

2015

Defect Characterization of 4H-SiC by Deep Level Transient Spectroscopy (DLTS) and Influence of Defects on Device Performance

Mohammad Abdul Mannan
University of South Carolina - Columbia

Follow this and additional works at: <http://scholarcommons.sc.edu/etd>

Recommended Citation

Mannan, M. A. (2015). *Defect Characterization of 4H-SiC by Deep Level Transient Spectroscopy (DLTS) and Influence of Defects on Device Performance*. (Doctoral dissertation). Retrieved from <http://scholarcommons.sc.edu/etd/3083>

This Open Access Dissertation is brought to you for free and open access by Scholar Commons. It has been accepted for inclusion in Theses and Dissertations by an authorized administrator of Scholar Commons. For more information, please contact SCHOLARC@mailbox.sc.edu.

DEFECT CHARACTERIZATION OF 4H-SIC BY DEEP LEVEL TRANSIENT
SPECTROSCOPY (DLTS) AND INFLUENCE OF DEFECTS ON DEVICE
PERFORMANCE

by

Mohammad Abdul Mannan

Bachelor of Science
Bangladesh University of Engineering and Technology, 1998

Master of Science
Concordia University, 2011

Submitted in Partial Fulfillment of the Requirements

For the Degree of Doctor of Philosophy in

Electrical Engineering

College of Engineering and Computing

University of South Carolina

2015

Accepted by:

Krishna C. Mandal, Major Professor

Yinchao Chen, Committee Member

Guoan Wang, Committee Member

Fanglin Chen, Committee Member

Lacy Ford, Vice Provost and Dean of Graduate Studies

© Copyright by Mohammad Abdul Mannan, 2015
All Rights Reserved.

DEDICATION

This dissertation is dedicated to my wife Farhana Anjum, my daughter Fabliha Maliyat and my son Fawaz Mustaneer, whose relentless encouragement and support during this extraordinary odyssey has helped me to put my best efforts toward this research work.

ACKNOWLEDGEMENTS

Firstly, I would like to thank my advisor, Dr. Krishna C. Mandal, for his continued support and guidance on this research. My development within his group has allowed me to undertake this work with the proper knowledge and skillset. I would also like to thank my committee members, Dr. Yinchao Chen, Dr. Guoan Wang, and Dr. Fanglin Chen, for taking the time to oversee my research and their support of my work.

I would also like to thank the following people for their contributions to the research performed in this work:

- Khai Nguyen, who assisted heavily to set up take Alpha Spectrometer and taking Spectroscopy measurement.
- Dr. Sandeep K. Chaudhuri (Electrical Engineering, University of South Carolina) for his assistance during the set-up of the DLTS equipment.
- The staff of Electron Microscopy Center (EMC) at the University of South Carolina for their assistance with Scanning Electron Microscopy (SEM) and Energy Dispersive X-ray Spectroscopy (EDX) studies.
- Dr. Shuguo Ma (College of Engineering and Computing, University of South Carolina) for performing the XPS characterization.

I would also like to thank my fellow lab members, Ramesh Krishna, Sandip Das, Kelvin Zavalla, Rahmi Pak, and Cihan Oner for their support and friendship throughout this process. Finally, I would like to thank all those faculty members and staff in the Electrical Engineering department at the University of South Carolina whose cumulative efforts have contributed to the successful completion of my doctoral research. Without their contributions, this work would have been impossible to perform.

ABSTRACT

Silicon carbide (SiC) is one of the key materials for high power opto-electronic devices due to its superior material properties over conventional semiconductors (e.g., Si, Ge, GaAs, etc). SiC is also very stable and a highly suitable material for radiation detection at room temperature and above. The availability of detector grade single crystalline bulk SiC is limited by the existing crystal growth techniques which introduce extended and microscopic crystallographic defects during the growth process. Recently, SiC based high-resolution semiconductor detectors for ionizing radiation have attracted world-wide attention due to the availability of high resistive, highly crystalline epitaxial layers with very low micropipe defect content ($< 1 \text{ cm}^{-2}$). SiC Schottky barrier radiation detectors on epitaxial layers can be operated with a high signal-to-noise ratio even above room temperature due to its wide band-gap. However, significant amount of intrinsic defects and impurities still exist in the grown SiC epilayer which may act as traps or recombination/generation centers and can lead to increased leakage current, poor carrier lifetime, and reduced carrier mobility. Unfortunately, the nature of these electrically active deep levels and their behavior are not well understood. Therefore, it is extremely important to identify these electrically active defects present in the grown epitaxial layers and to understand how they affect the detector performance in terms of leakage current and energy resolution.

In this work, Schottky barrier radiation detectors were fabricated on high quality n-type 4H-SiC epitaxial layers. The epitaxial layers were grown on nitrogen doped n-type 4H-SiC (0001) substrates by a hot wall chemical vapor deposition (CVD) process. The epitaxial growth was carried out with 8° off-cut towards the $[11\bar{2}0]$ direction. The Schottky barriers were formed on the epitaxial layers (Si-face) by depositing thin (~ 10 nm) circular Ni contact (area $\sim 10 \text{ mm}^2$) which acts as the detector window. The thickness of the detector window was decided such that there was minimal alpha energy attenuation while maintaining a reliable electrical contact. For the back contact, ~ 100 nm thick square ($\sim 40 \text{ mm}^2$) Ni contact was deposited on the C-face of the 4H-SiC substrate.

The junction properties of the fabricated Schottky barrier radiation detectors were characterized through current-voltage (I-V) and capacitance-voltage (C-V) measurements. From the fabricated devices, those with high barrier height (~ 1.6 eV) and extremely low leakage current (few pA at a reverse bias of ~ -100 V) were selected for alpha spectroscopic measurements. Alpha pulse-height spectra was obtained from the charge pulses produced by the detector irradiated with a standard $0.1 \mu\text{Ci } ^{241}\text{Am}$ source. The charge transport and collection efficiency results, obtained from the alpha particle pulse-height spectroscopy, were interpreted using a drift-diffusion charge transport model. The detector performances were evaluated in terms of the energy resolution. From alpha spectroscopy measurements the FWHM (full width at half maxima) of the fabricated Schottky barrier detectors were in the range of 0.29% - 1.8% for the main alpha peak of ^{241}Am (5.486 MeV).

Deep level transient spectroscopy (DLTS) studies were conducted in the temperature range of 80 K - 800 K to identify and characterize the electrically active defects present in the epitaxial layers. Deep level defect parameters (i.e. activation energy, capture cross-section, and density) were calculated from the Arrhenius plots which were obtained from the DLTS spectra at different rate windows. The observed defects in various epitaxial layers were identified and compared with the literature. In the 50 μm epitaxial layer, a new defect level located at $E_c - 2.4$ eV was observed for the first time. The differences in the performance of different detectors were correlated on the basis of the barrier properties and the deep level defect types, concentrations, and capture cross-sections. It was found that detectors, fabricated on similar wafers, can perform in a substantially different manner depending on the defect types. For 20 μm epitaxial layer Schottky barrier radiation detectors, deep levels $Z_{1/2}$ (located at $\sim E_c - 0.6$ eV) and $\text{EH}_{6/7}$ (located at $\sim E_c - 1.6$ eV) are related to carbon vacancies and their complexes which mostly affect the detector resolution. For 50 μm epitaxial layer Schottky barrier radiation detectors, $Z_{1/2}$, EH_5 , and the newly identified defect located at $E_c - 2.4$ eV mostly affect the detector resolution.

The annealing behavior of deep level defects was thoroughly investigated by systematic C-DLTS measurements before and after isochronal annealing in the temperature range of 100 $^{\circ}\text{C}$ - 800 $^{\circ}\text{C}$. Defect parameters were calculated after each isochronal annealing. Capture cross-sections and densities for all the defects were investigated to analyze the impact of annealing. The capture cross-sections of the defects Ti (c) (located at $E_c - 0.17$ eV) and EH_5 (located at $E_c - 1.03$ eV) were observed to

decrease with annealing temperature while the densities did not change significantly. Deep level defects $Z_{1/2}$ and $EH_{6/7}$ were found to be stable up to the annealing temperature of 800 °C.

TABLE OF CONTENTS

DEDICATION.....	iii
ACKNOWLEDGEMENTS	iv
ABSTRACT.....	vi
LIST OF TABLES	xii
LIST OF FIGURES	xiii
LIST OF ABBREVIATIONS	xviii
CHAPTER 1: GENERAL INTRODUCTION.....	1
1.1 DISSERTATION INTRODUCTION	1
1.2 DISSERTATION OVERVIEW.....	4
CHAPTER 2: SiC: PROPERTIES AND ELECTRONIC DEVICES.....	6
2.1 SiC MATERIAL PROPERTIES.....	6
2.2 SiC CRYSTAL GROWTH.....	8
2.3 THEORETICAL BACKGROUND METAL-SEMICONDUCTOR CONTACT.....	12
2.4 CONCLUSION.....	25
CHAPTER 3: DEFECTS IN SiC	26
3.1 OVERVIEW	26
3.2 POINT DEFECTS.....	26
3.3 MORPHOLOGICAL DEFECTS	27
3.4 MORPHOLOGICAL DEFECTS DELINEATION BY ETCHING	30
3.5 CONCLUSIONS.....	35
CHAPTER 4: DETECTOR FABRICATION AND CHARACTERIZATION.....	37
4.1 4H-SiC DETECTOR FABRICATION	37

4.2	ELECTRICAL CHARACTERISTICS OF FABRICATED DETECTOR.....	39
4.3	RADIATION INTERACTION WITH SEMICONDUCTOR MATERIALS.....	47
4.4	DRIFT-DIFFUSION MODEL.....	48
4.5	RADIATION DETECTION	49
4.6	ALPHA SPECTROSCOPY MEASUREMENT RESULTS	58
4.7	CONCLUSION.....	64
CHAPTER 5: DEFECT CHARACTERIZATION BY DLTS STUDIES		65
5.1	INTRODUCTION	65
5.2	DEFECT PARAMETERS.....	67
5.3	DEFECT CHARACTERIZATION BY THERMALLY STIMULATED CURRENT.....	68
5.4	THEORETICAL BACKGROUND OF DLTS MEASUREMENT	75
5.5	DLTS EXPERIMENTAL SETUP.....	83
5.6	DEFECTS' ROLE ON DETECTOR PERFORMANCE	97
5.7	CONCLUSION.....	101
CHAPTER 6: ANNEALING BEHAVIOR OF CRYSTALLINE DEFECTS		102
6.1	INTRODUCTION	102
6.2	DEEP LEVEL TRANSIENT SPECTRA BEFORE ANNEALING.....	102
6.3	EXPERIMENT FOR ISOCHRONAL ANNEALING STUDIES	105
6.4	ANNEALING STUDIES RESULTS	107
6.5	CONCLUSION.....	125
CHAPTER 7: CONCLUSION AND SUGGESTIONS FOR FUTURE WORK		127
7.1	CONCLUSION.....	127
7.2	FUTURE WORK	129
REFERENCES.....		132

LIST OF TABLES

Table 2.1. Comparisons of properties of selected important materials at 300 K [35]	9
Table 4.1. I-V characteristics parameters of the Schottky detector	41
Table 5.1. Trap parameters deduced from TSC measurements [86]	72
Table 5.2. Trap parameters by TSC measurements for the 4H-SiC n-type epilayer [92].	74
Table 5.3. Defect parameters of the deep levels for the detector AD06.....	91
Table 5.4. Defect parameters of the detector AS1 obtained from the DLTS scans	93
Table 5.5. Defect parameters of the detector AS2 obtained from the DLTS scans	93
Table 5.6. Defect parameters of the detector AS3 obtained from the DLTS scans	93
Table 5.7. Detector properties and defect parameters for the detector AS1	99
Table 5.8. Detector properties and defect parameters for the detector AS2	99
Table 5.9. Detector properties and defect parameters for the detector AS3	99
Table 5.10. Detector properties and defect parameters for the detector AD06	100
Table 6.1. Defect Parameters Obtained from the DLTS Measurements.	104
Table 6.2. Defect parameters obtained after annealing at 100 °C.....	115
Table 6.3. Defect parameters after annealing at 200 °C	116
Table 6.4. Defect parameters after annealing at 400 °C	117
Table 6.5. Defect parameters after annealing at 600 °C	118
Table 6.6. Defect parameters after obtained annealing 800 °C.....	119

LIST OF FIGURES

Figure 2.1. Energy band diagram of metal-semiconductor Ohmic contact: (a) Metal and n-type semiconductor; (b) Metal and p-type semiconductor.	14
Figure 2.2. Energy band diagram of metal-semiconductor Schottky contact; (a) Metal and n-type semiconductor; (b) Metal and p-type semiconductor.	16
Figure 2.3. Transport process in a forward biased Schottky barrier	19
Figure 2.4. Linear fit of current-voltage (I-V) acquired data plotted in logarithmic scale	22
Figure 2.5. Capacitance-voltage data acquired using a Schottky diode.	23
Figure 2.6. $1/C^2$ vs. reverse bias plot with linear fitting. Variation of $1/C^2$ as a function of reverse bias corresponding to the C-V plot shown in above . The straight line shows the linear fit of the experimental data.	25
Figure 3.1. SEM image of the molten KOH etched bulk SiC: (a) Region with TSDs and TEDs; (b) Regions with BPDs and TEDs.....	33
Figure 3.2. SEM images of the molten KOH etched bulk SiC: (a) Region with TSDs and TEDs; (b) Enlarge images of micropipes; (C)) Enlarge images of closed core and threading edge dislocations.....	34
Figure 3.3. (a) SEM images of the molten KOH etched SiC epitaxial layers; (b) Enlarged images of closed core and threading edge dislocations.	35
Figure 4.1. Photograph of an n-type 4H-SiC epitaxial layer wafer.	37
Figure 4.2. Schematic diagram of the cross-sectional view of 50 μ m thick n-type 4H-SiC Schottky barrier device.	38
Figure 4.3. Schematic of the I-V and C-V experimental setup.....	39
Figure 4.4. Photograph of the experimental setup for the I-V and C-V measurements. The detector is mounted inside the aluminum box.	40
Figure 4.5. Variation of junction current as a function of applied bias for a 50 μ m n-type Ni/4H-SiC epitaxial Schottky barrier radiation detector.	42
Figure 4.6. Forward I-V characteristics on 4H-SiC epitaxial Schottky barrier detectors AS1, AS2, and AS3.	43

Figure 4.7. Reverse I-V characteristics obtained for 4H-SiC epitaxial Schottky barrier detectors AS1, AS2, and AS3.	44
Figure 4.8. $1/C^2$ vs V plot for a 50 μm n-type Ni/4H-SiC epitaxial Schottky barrier detector. The open circles are the experimental data points and the solid line is a straight line fit to the experimental data. Inset shows the original C-V plot.	45
Figure 4.9. $1/C^2$ vs V plots for 4H-SiC epitaxial Schottky barrier radiation detectors AS1, AS2, and AS3.....	47
Figure 4.10. Energy loss of 5.48 MeV alpha particle as a function of penetration depth.	48
Figure 4.11. Schematic diagram of an analog radiation detection measurement system.	50
Figure 4.12. (a) Simplified circuit diagram for a charge sensitive preamplifier used in a detection system. (b) Input and output pulse shapes seen by a preamplifier [7] ..	51
Figure 4.13. (a) Typical input and output pulse shapes seen by a shaping amplifier. (b) Simplified circuit diagram for the various stages of differentiation (CR) and integration (RC) used by an analog shaping amplifier [81].....	52
Figure 4.14. Photograph of the 4H-SiC epitaxial Schottky barrier radiation detector inside RFI/EMI shielded test box.	53
Figure 4.15. Connection schematic for analog data acquisition set-up.	54
Figure 4.16. Schematic of the electrical connections for energy calibration.....	56
Figure 4.17. (a) Pulse-height spectrum obtained for six different pulse sizes, and (b) Corresponding calibration curve.....	57
Figure 4.18. Picture of the radiation detection system at USC.....	58
Figure 4.19. Variation of experimentally obtained (\square) and theoretically calculated (\circ) CCE. CCE from drifts (Δ) and diffusion (∇) are also shown. The solid line shows the variation in depletion width.	59
Figure 4.20. Variation of detector energy resolution as a function of reverse bias voltage. The variation of the peak width (FWHM) of the pulser recorded simultaneously has also been plotted.	61
Figure 4.21. An ^{241}Am pulse-height spectrum obtained using the 50 μm n-type Ni/4H-SiC epitaxial Schottky barrier detector reverse biased at 130 V.	62
Figure 4.22. Alpha pulse-height spectra obtained for detectors (a) AS1, (b) AS2, and (c) AS3 using an ^{241}Am source.....	63
Figure 5.1. Illustration of electron and hole trapping and de-trapping phenomena in a semiconductor material.....	66

Figure 5.2. TSC spectrum showing trap centers at temperatures T_{m1} and T_{m2} . [85].	69
Figure 5.3. Schematic of the TSC experimental setup.	71
Figure 5.4. TSC spectra for the heat rates of 5 K/min (----), 10 K/min (—), and 15 K/min (.....) at 10 V bias voltage. (b): Arrhenius plot of $\ln(T_m^4/\beta)$ versus $1000/T$ for five traps corresponding to peak numbers 1 – 5 in Figure (a).	72
Figure 5.5. TSC spectrum of n-type 4H-SiC epitaxial layer obtained at 10 V reverse bias and 15 K/min heat rate [92].	74
Figure 5.6. A schematic of the DLTS transient signal generation. (A): Steady state reverse bias, (B): Applying pulse; (C) Just after removing pulse; (D) Capacitance transient due to thermal emission of carriers.	77
Figure 5.7. The applied bias and the capacitance change of the Schottky device as a function of time.	78
Figure 5.8. (a) Capacitance transient at various temperature (b) DLTS signal obtained by using double boxcar is plotted as a function of sample temperature [14].	81
Figure 5.9. An illustration of how a rate window produces a peak in its response when the emission rate of the input signal matches the rate selected by the window [14].	82
Figure 5.10. (a) The DLTS spectra corresponding to a trap center at various rate windows and (b) the Arrhenius plots obtained from the spectra.	82
Figure 5.11. Block-Diagram of the SULA DDS-12 DLTS setup.	84
Figure 5.12. Photograph of the SULA DDS-12 DLTS measurement system.	84
Figure 5.13. Photograph of the sample holder used in DLTS measurements.	85
Figure 5.14. DLTS spectra obtained using the 50 μm n-type Ni/4H-SiC epitaxial Schottky barrier radiation detector (AD06) in a temperature range (a) 80 K - 140 K with the smallest initial delay (b) 80 K - 800 K with the largest initial delay.	88
Figure 5.15. DLTS scan for detectors AS2, AS1, and AS3 showing negative peaks related to electron traps present in the 4H-SiC epilayer detectors.	90
Figure 5.16. Arrhenius plots obtained for the Peaks #1 - #6 corresponding to the DLTS spectra shown in Figure 5.14.	91
Figure 5.17. Arrhenius plots for determining the activation energy obtained from the DLTS scans shown in Figure 5.15 for detectors (a) AS2, (b) AS1, and (c) AS3. The solid lines show the linear fits.	92
Figure 6.1. DLTS spectra obtained using the 50 μm thick n-type Ni/4H-SiC unannealed epitaxial Schottky barrier in the temperature range: (a) 85 K - 130 K with a	

smaller set of initial delays, and (b) 200 K - 800 K with a larger set of initial delays.	103
Figure 6.2. Arrhenius plots obtained for the peaks #1 - #4 corresponding to the DLTS spectra shown.....	104
Figure 6.3. Block diagram of annealing set up at USC.	105
Figure 6.4. Picture of the annealing set up at USC.	106
Figure 6.5. Forward current voltage (I-V) characteristics of the as-fabricated 50 μm thick n-type 4H-SiC Schottky barrier and after isochronal annealing at different temperatures:.....	108
Figure 6.6. Reverse current voltage (I-V) characteristics of the as-fabricated 50 μm thick n-type 4H-SiC Schottky barrier and after isochronal annealing at different temperatures:.....	108
Figure 6.7. Variation of ideality factors with isochronal annealing of 50 μm thick n-type 4H-SiC Schottky barrier device.	110
Figure 6.8. Capacitance vs voltage of the as-fabricated 50 μm thick n-type 4H-SiC Schottky barrier and after isochronal annealing at different temperatures.	111
Figure 6.9. DLTS spectra obtained using the 50 μm thick n-type Ni/4H-SiC epitaxial Schottky barrier in a temperature range 80 K - 140 K: (a) as-fabricated, annealed at 100 $^{\circ}\text{C}$ and 200 $^{\circ}\text{C}$; and (b) annealed at 400 $^{\circ}\text{C}$, 600 $^{\circ}\text{C}$, and 800 $^{\circ}\text{C}$ respectively.	112
Figure 6.10. DLTS spectra obtained in a temperature range 250 K - 750 K: (a) as-fabricated and annealed at 100 $^{\circ}\text{C}$ and 200 $^{\circ}\text{C}$; and (b) annealed at 400 $^{\circ}\text{C}$, 600 $^{\circ}\text{C}$, and 800 $^{\circ}\text{C}$	114
Figure 6.11. Arrhenius plot corresponding to the DLTS spectra obtained after annealing at 100 $^{\circ}\text{C}$	115
Figure 6.12. Arrhenius plots corresponding to the DLTS spectra obtained after annealing at 200 $^{\circ}\text{C}$	116
Figure 6.13. Arrhenius plots corresponding to the DLTS spectra obtained after annealing at 400 $^{\circ}\text{C}$	117
Figure 6.14. Arrhenius plots corresponding to the DLTS spectra obtained after annealing at 600 $^{\circ}\text{C}$	118
Figure 6.15. Arrhenius plot corresponding to the DLTS spectra obtained after annealing at 800 $^{\circ}\text{C}$	119

Figure 6.16. Defect ($E_c - 0.17$ eV corresponding to peak #1) parameters variation with annealing temperature: (a) capture cross-section, and (b) defect density. 121

Figure 6.17. Defect $Z_{1/2}$ (corresponding to peak #2, $E_c - 0.67$ eV) parameters variation with annealing temperature: (a) capture cross-section, and (b) defect density... 122

Figure 6.18. Defect EH_5 (corresponding to peak #3, $E_c - 1.03$ eV) parameters variation with annealing temperature: (a) capture cross-section, and (b) defect density... 124

Figure 6.19. Defect $EH_{6/7}$ (corresponding to peak #4, $E_c - 1.6$ eV) parameters variation with annealing temperature: (a) capture cross-section, and (b) defect density... 125

LIST OF ABBREVIATIONS

BPDs	Basal Plane Dislocations
CVD	Chemical Vapor Deposition
DLTS	Deep Level Transient Spectroscopy
EBIC	Electron Beam Induced Current
FWHM	Full Width at Half Maxima
HEMT	High Electron Mobility Transistor
keV	Kilo Electron Volt
LPE	Liquid Phase Epitaxy
MeV	Mega Electron Volt
MCA	Multi-Channel Analyzer
MBE	Molecular Beam Epitaxy
PICTS	Photo Induced Current Transient Spectroscopy
SEM	Scanning Electron Microscopy
TSC	Thermally Stimulated Current
TED	Threading Edge Dislocation

CHAPTER 1: GENERAL INTRODUCTION

1.1 DISSERTATION INTRODUCTION

The perfect crystal, described in any introductory solid state book, is rare to find in nature. Many things, such as impurities, vacancies, broken bonds, lattice strain and stress, are responsible for imperfections in the crystal. Imperfect crystals are due to the introduction of impurities which are desirable in a vast area of solid state application. Hence, adding impurities in a controlled way (doping) is very important for successful device fabrication. However, in many cases the presence of impurities and other imperfections affect the semiconductor properties in an undesired way which is detrimental for the device performance. Therefore, the nature of the defects and their impact on carrier transport are crucial for device fabrication.

Imperfection in crystal structure arises mainly due to the structural defects, impurities, and vacancies. Structural defects are created due to lattice strain during material growth and processing which gives rise to stacking faults and dislocations. Impurities, either intentionally or inadvertently introduced, disturb the lattice periodicity by substituting native crystal atoms or forming complexes [1]. Vacancies, i.e. missing atoms from their regular atomic site, are formed during solidification of the crystal which disturbs the periodic structure of the crystal. The impurity and vacancy induced defects

are known as point defects which create localized energy levels in the energy band-gap. Semiconductor electrical and optical properties strongly depend upon these defects' energy levels, their concentration, and nature.

On the basis of energy level location in the band-gap, the defects are classified as shallow and deep levels. Shallow levels are located near the band edges of the conduction band or valence band of the semiconductor. Substitutional impurities mainly introduce shallow levels and are used for doping to control the electrical conductivity, mobility, and resistivity of the semiconductor. Deep levels located further away from the band edges may originate from impurities, vacancies or structural defects. Their contribution to conduction is negligibly small compared to shallow levels. However deep levels may act as generation or recombination centers and can control the lifetime of the charge carriers. Consequently, optical and electrical characteristics of semiconductor devices are greatly influenced by electrically active deep level defects. It is proven that deep level defects affect the detector performance [2], degrade solar cell performance and reduce hetero-junction laser efficiency [3].

Both theoretical and experimental attempts have been made to characterize the deep level defects of semiconductors. Many techniques have been employed to develop a suitable theory for deep levels. In perturbative method the Hamiltonian and corresponding Eigen value problem is solved by assuming a perturbative potential introduced by the defect. By using this method, Jaros *et al.* calculated substitutional oxygen impurity in GaP [4], and Baraff *et al.* depicted vacancy related defects in Si [5,

6]. This approach suffers from convergence problems. In non-perturbative method, the eigenvalue problem is solved by assigning a single potential function to a cluster of atoms. Sulfur related defects in Si are calculated by this method which is in good agreement with experimental results [7]. Calculation based on this method is flawed by surface states and impurities in the crystal. Density Functional Theory (DFT) based *ab initio* calculations are used in several approaches to calculate vacancies and antisite related defects for wide band-gap materials [8]. Each theoretical method for deep level defect calculation is based on its own specific assumption which usually makes the method only suitable for a particular type of impurity and semiconductor.

Experimental characterization of deep level defects, such as temperature dependence of Hall effect, photoconductivity, electroluminescence etc, involve thermal or optical excitation to fill the defect center and subsequent de-excitation. In 1966 Williams first conducted a junction based experiment to investigate the deep level impurities located in the space charge region [9]. In junction based method, the experimental measurement is done either by static or dynamic technique. In static measurement, the current or capacitance is recorded as a function temperature such as thermally stimulated current [10] and thermally stimulated capacitance [11]. On the other hand, in dynamic technique, the capacitance or current transient is measured at different temperatures during the defect relaxation to equilibrium after a perturbation. In Deep Level Transient Spectroscopy (DLTS) [12, 13, 14] the excitation is done by electrical pulse, and in Photo Induced Current Transient Spectroscopy (PICTS) [15, 16], the excitation is done by optical signal.

DLTS is considered one of the most powerful equipment used for semiconductor defect characterization. DLTS is widely used to investigate deep level defects of different material such as Si [17], GaAs [18], GaN [19, 20], NiSi₂ precipitates in silicon [21], CZTS [22] etc. Besides Schottky diodes DLTS measurements also have been done on solar cells [23], high electron mobility transistors (HEMTs) [24], quantum wells [25, 26] etc. Presently, DLTS equipment is considered an essential tool in semiconductor fabrication and processing technology due to its wide application, sensitivity to lower defect concentration, and capability of determining most defect parameters.

1.2 DISSERTATION OVERVIEW

This work focuses on DLTS investigation of deep levels in the epitaxial layers of 4H-SiC wide band-gap materials and the correlation of defects with detectors fabricated on 4H-SiC epitaxial layers.

Chapter 1 is an introductory chapter to describe the background, importance, and organization of this work. The whole study related to this work is described in seven chapters.

Chapter 2 is an introduction to SiC material properties, growth, and a brief description of SiC based devices. Junction theory of metal-semiconductor Schottky contact and Ohmic contact is also explained in this chapter.

Chapter 3 is a description of SiC extended and point defects. This chapter also discusses the etching studies to delineate different extended defects.

Chapter 4 is dedicated to detector fabrication based on the epitaxial layer of 4H-SiC and in detailed characterization of the fabricated detectors. Current-Voltage (I-V) and Capacitance-Voltage (C-V) measurement technique, Alpha spectroscopy measurement technique, and the results obtained are discussed here.

Chapter 5 is an introduction to defect characterization by different techniques. Basic principles of thermally stimulated current (TSC) and results obtained by TSC measurements are described. The detailed background description of DLTS technique, the experimental setup and results obtained in this work are explained in this chapter. The experimental results are analyzed by comparing with previously reported data. The correlation between deep level defects and detector performance are discussed in this chapter.

Chapter 6 is dedicated to describing the annealing behavior of the deep levels in 4H-SiC epitaxial layers. Isochronal annealing impact on the defect parameters of each individual defect is described in this chapter.

Finally, Chapter 7 concludes the research presented in this dissertation and provides suggestions for future work.

CHAPTER 2: SiC: PROPERTIES AND ELECTRONIC DEVICES

2.1 SiC MATERIAL PROPERTIES

Silicon carbide is an indirect wide band-gap semiconductor. SiC is thermally stable up to about 2000 °C, even in oxidizing and aggressive environments. SiC is one of the most intensively studied materials among all the other wide band-gap semiconductors. The Swedish scientist Jons Jakob Berzelius first discovered silicon carbide in 1824 [27]. Since then silicon carbide has been commercialized as an abrasive due its extreme hardness (~ 9.5 in Mohs scale). Silicon carbide is also used for fireproofing, high-temperature ceramics, and resistive heating elements. After discover of its rectifying properties, silicon carbide crystal detectors were used in the early days of radio communications. Around the 1940s, silicon carbide was abandoned as a semiconductor material with the emergence of silicon based semiconductor technology. In the late 1970s, silicon carbide was in focus as a suitable semiconductor material for blue light emitting diode, but soon it was replaced by group III-nitride wide band-gap direct semiconductor. The main bottle neck of spreading silicon carbide technology is difficulty in producing good quality crystals. However, the availability of high quality silicon carbide crystal with the advanced semiconductor technology and the necessity of suitable high power electronic device materials prompted the commercialization of silicon carbide devices in the beginning of the 21st century.

Silicon carbide crystal lattice is structured from closely packed silicon-carbon bilayers (also called Si-C double layers). Si-C bilayer can be viewed as a planar sheet of silicon atoms coupled with a planar sheet of carbon atoms. Due to the sequential variation of these stacked bilayers silicon carbide has many crystal structures. This property is known as polytypism. Polytypes represent different staking sequences of atomic planes in one certain direction. The staking sequence causes hexagonal and cubic lattice sites in the crystal structure. The different layers are usually designated by the letter A, B, and C. To specify the cubic, hexagonal and rhombohedral symmetry of the crystal lattice the letters C, H and R are used, respectively [28]. The repetition number of bilayers in the stacking sequence is expressed by an integer number. From the side view, the staking sequence of SiC crystal shows a zig-zag pattern which terminates with a silicon face on a surface and with carbon atoms on the opposing surface.

Different polytypes vary from each other only in the stacking sequence of double layers of Si and C atoms. However, due to this difference in staking sequence, the optical and electrical properties such as band-gap, saturated drift velocity, breakdown electric field strength, and the impurity ionization energies vary significantly from polytype to polytype [29, 30, 31]. Even for a given polytype, some electrical properties are shown non-isotropic behavior and have strong dependency on the crystallographic direction. Among all of the existing polytypes, the following are the most common:

- 2H This is a wurtzite structure with the stacking sequence AB and has hexagonal symmetry. Growth of this polytype is difficult and did not receive any attention.
- 3C Here the stacking repeats itself every three bilayers. This polytype is cubic zinc blende structure with the stacking sequence ABC.
- 4H This polytype has wurtzite structure with the stacking sequence ABAC and has hexagonal symmetry. It has 50% cubic and 50% hexagonal lattice sites and most intensively studied poly-type for power electronic devices.
- 6H It has the stacking sequence ABCACB and contains $2/3$ cubic and $1/3$ hexagonal lattice sites. 6H polytype has more pronounced anisotropy compared to 4H silicon carbide.

Among different polytypes, 4H-SiC is usually preferred for electronic devices due to its better charge transport properties [32, 33, 34]. However, any promising semiconductor properties are usually evaluated against silicon due to its wide market share in the solid state technology. The comparison of the properties of 4H-SiC with other commonly used semiconductor is shown in Table 2.1 [35]. From the table, it is apparent that 4H-SiC is superior to silicon for the device material where wide bandgap energy, high breakdown electric field, high carrier saturation drift velocity, and high atom displacement energy are expected.

2.2 SiC CRYSTAL GROWTH

The SiC based electronic and optoelectronic device performances highly depend upon the improvement of bulk crystal and epitaxial growth technology. SiC does not show a liquid

phase and the only way to grow, synthesize, and purify silicon carbide is by means of gaseous phases. For the growth of electronic-grade silicon carbide the most common techniques are:

Table 2.1. Comparisons of properties of selected important materials at 300 K [35]

Properties/Material	D*	Si	Ge	GaAs	CdTe	4H-SiC
Bandgap (eV)	5.5	1.12	0.67	1.42	1.49	3.27
Relative dielectric constant	5.7	11.9	16	13.1	10	9.7
Breakdown field (MV cm ⁻¹)	10	0.3	0.1	0.4	0.5	3.0
Density (g cm ⁻³)	3.5	2.3	5.33	5.3	5.9	3.2
Atomic number Z	6	14	32	31-33	48-52	14-6
e-h creation energy (eV)	13	3.6	2.95	4.3	4.42	7.78
Saturation electron velocity (×10 ⁷ cm ² s ⁻¹)	2.2	1.0	0.6	1.2	1.0	2
Electron mobility (cm ² V ⁻¹ S ⁻¹)	1800	1300	3900	8500	1100	800
Hole mobility (cm ² V ⁻¹ S ⁻¹)	1200	460	1900	400	100	115
Threshold displacement energy (eV)	40-50	13-20	16-20	8-20	6-8	22-35
Minimum ionizing energy loss (MeV cm ⁻¹)	4.7	2.7	6	5.6		4.4

D* -Diamond

Physical Vapor Transport (PVT): A solid source of silicon carbide is evaporated at high temperatures and the vapors crystallize at a colder part of the reactor.

Chemical Vapor Deposition (CVD): Gas-phase silicon and carbon containing precursors react in a reactor and silicon carbide is solidified on target.

2.2.1 Bulk Growth

Bulk growth of SiC is the first step for any SiC application. During bulk growth the target is to grow large single crystals in high quantities, and the emphasis placed on achieving a high growth rate. Silicon carbide cannot be grown by seeded solidification from melts because SiC sublimates before it melts. Therefore, the bulk growth is usually done by a method based on physical vapor transport which is known as modified-Lely method [36]. In the modified Lely method, either powder or polycrystalline source materials are sublimed at $\sim 2300\text{ }^{\circ}\text{C} - 2500\text{ }^{\circ}\text{C}$ in a closed crucible under low-pressure inert gas ambient. The vapor from the sublimation mainly consists of Si, Si_2C , and SiC_2 from sublimation which migrates and deposits on a monocrystalline SiC seed kept at a lower temperature. The crystal growth parameters such as growth rate uniformity, grown stress in the material, crystalline quality, are dependent on the reactor design. Different approaches have been offered to optimize the reactor design in order to have better control of thermal gradients inside the growth chamber [37]. In every approach, the main focus is always on increasing the diameter of the wafers while at the same time reducing the density of extended material defects such as micropipes and dislocations. At present, 3-inch diameter substrates are commercially available from multiple vendors [38]. Recently CREE Inc. has presented zero micropipe wafers [39]. In this method of crystal growth, precise doping and uniformity cannot be controlled easily because the evaporation and growth takes place in a closed environment. This fact discourages device fabrication directly on the sublimation grown SiC wafers.

2.2.2 Epitaxial Growth

SiC devices are hardly fabricated directly in sublimation-grown bulk wafers because of low crystal quality. Higher crystalline quality SiC epitaxial layers are needed for SiC electronic applications. The epilayers are more controllable and reproducible than bulk SiC wafer. There are several growth techniques for SiC epitaxial layers including liquid phase epitaxy (LPE), sublimation epitaxy, molecular beam epitaxy (MBE), and chemical vapor deposition (CVD).

Liquid phase epitaxy (LPE) is a technique where the growth of SiC takes place from a supersaturated solution of Si and C at slightly above 1415° C which is the melting temperature of silicon. In LPE, it is difficult to control the surface morphology, doping level, and conductivity type. This method suffers from low carbon solubility in a silicon melt and is used for the healing of micropipe defects and to grow a buffer layer on substrates [35, 40].

Sublimation epitaxy growth mechanism is similar to those for bulk sublimation growth. However compared to bulk, the sublimation epitaxy is grown at lower temperature (1800 °C – 2200 °C) with higher growth pressure (~ 1 atm) [41]. This technique is suitable for thick epitaxial layers with high growth rate.

In molecular beam epitaxy (MBE), the growth rate is very low (order of nanometers per hour) and the growth temperature is also quite low. This technique is usually applied to grow a very thin epitaxial layer for surface science studies [35].

Chemical Vapor Deposition (CVD) is the most promising technique for growing thick epitaxial layers of low and uniform doping concentration with good morphology. In this process, silicon and carbon containing gases are transported to a chamber where chemical reaction occurs and material is deposited on the SiC substrate surface. In a typical SiC-CVD epitaxial process, growth rates up to $50 \mu\text{m h}^{-1}$ can be achieved at substrate temperatures of around $\sim 1500 \text{ }^\circ\text{C}$. In SiC-CVD process, horizontal hot-wall reactor is used to reach higher growth temperature (up to $2000 \text{ }^\circ\text{C}$) with more efficient heating of the substrate [42]. In this technique, the precursor gases are utilize more efficiently, and consequently, a growth rate up to $100 \mu\text{m h}^{-1}$ can be achieved.

2.3 THEORETICAL BACKGROUND METAL-SEMICONDUCTOR CONTACT

2.3.1 Overview

Semiconductor junctions are the most important device in solid state technology. Due to the interesting electrical or opto-electrical properties of the junction, numerous opto-electronic devices can be made based on the semiconductor junction. The semiconductor junction can be formed in the following ways:

- a. Junction formed from the joining of p-type and n-type of the same semiconductor called as *p-n* homojunction.
- b. Junctions made of two different semiconductors with different band-gap, such as GaAs and AlGaAs. These can be *p-n* junctions or isotype heterojunctions (*n-n* or *p-p*).
- c. Junctions created between metals of suitable work function and semiconductors of suitable electron affinity are known as Schottky barriers.
- d. Junctions made of metals and semiconductors that form Ohmic contacts.

All *p-n* junction and Schottky barriers have rectifying characteristics. P-n junctions are widely used in power electronic devices. Schottky diode is preferable for fast response diode and photodetectors. For the defect characterization by DLTS technique, both p-n junction and Schottky diode are suitable. In this study, Schottky diode is used to investigate the defects in 4H-SiC epitaxial layer. The Schottky diodes are fabricated on 4H-SiC epitaxial layer, and Ohmic contact is formed on the bulk side of 4H-SiC. Therefore, it is very important to understand the theoretical concepts behind the formation of Schottky and Ohmic contact. For Schottky contacts, the thermionic emission model was used in order to study the contact properties in SiC diodes in terms of the barrier height and the ideality factor using current-voltage (I-V) measurements. For further characterization of the Schottky contact, the calculation procedure of doping concentration and built-in voltage using capacitance-voltage (C-V) measurements are described.

2.3.2 Ohmic Contact

A metal-semiconductor junction is formed Ohmic contact when it does not show any rectifying characteristics during I-V measurements. The contact simply behaves as a resistor and the current-voltage across the resistance follow a linear relationship. A good Ohmic contact would have negligible contact resistance, small voltage drop even at a large current, and same voltage drop for both forward and reverse current.

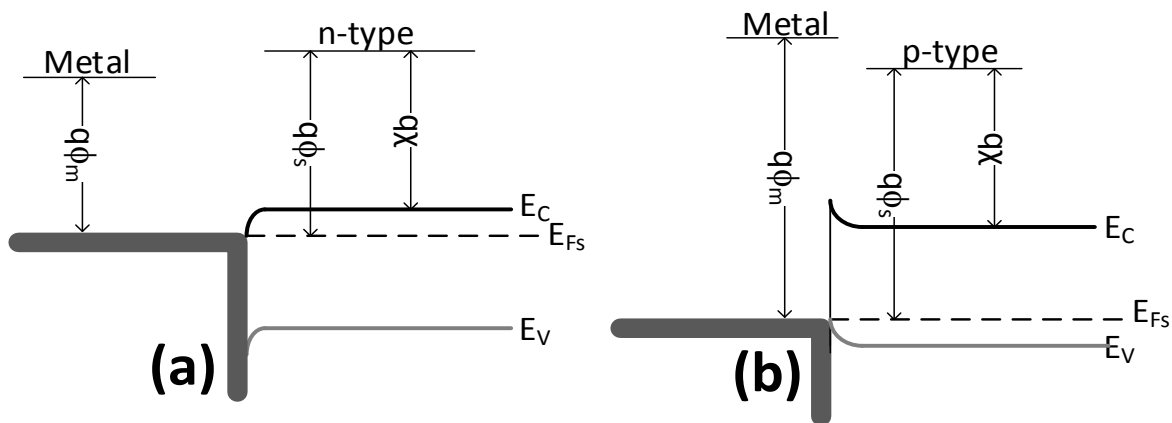


Figure 2.1. Energy band diagram of metal-semiconductor Ohmic contact: (a) Metal and n-type semiconductor; (b) Metal and p-type semiconductor.

The metal is characterized by the work function of the metal Φ_m (energy required to remove an electron from the Fermi level to the vacuum level), and the semiconductor is characterized by the work function of the semiconductor Φ_s (energy required to remove an electron from the Fermi level to the vacuum level). The work function of metal and semiconductor are measured with respect to the vacuum level (the energy of an electron at rest outside the material). Figure 2.1 shows the thermal equilibrium energy band

diagram of a metal-semiconductor Ohmic contact for n-type and p-type semiconductor. For Ohmic contact formation the metal work function should be less than the n-type semiconductor work function and greater than the p-type semiconductor work function. In both cases the Fermi levels are aligned between the metal and the semiconductor. The difference between metal Fermi levels and semiconductor Fermi level diminishes at the moment of forming the junction by exchanging charges at the edges of the bands. The energy band diagrams shows that there is no barrier blocks to halt the flow of electrons in the case of metal n-type contact and holes in the case of metal p-type contact. Hence the current can flow through the junction regardless of the polarity of the applied voltage.

The 4H-SiC material used for Schottky diode fabrication can be considered as intrinsic with the energy band-gap of ~3.26 eV at 300K [43] and the work function was calculated to be 4.73 eV using Equation 2.1

$$\phi_s = \chi + \frac{E_g}{2} \quad 2.1$$

where χ is the electron affinity (energy required to remove an electron from the conduction band to the vacuum level), and E_g is the band-gap. In order to form Ohmic contact, deposited metal work function should be less than 4.73 eV.

2.3.3 Schottky Contact Formation and Energy Band Diagram

A metal-semiconductor contact is called Schottky contact when it has a rectifying effect providing current conduction at forward bias (metal to semiconductor) and presenting a low saturation current at reverse bias (semiconductor to metal). Figure 2.2 shows the Schottky metal-semiconductor contact after thermal equilibrium. In the Schottky model, the vacuum level is assumed to be continuous across the interface and the metal work function and semiconductor electron affinity are assumed to be constant throughout the material right to the interface. In both cases it can be observed that the Fermi levels are aligned between the metal and the semiconductor.

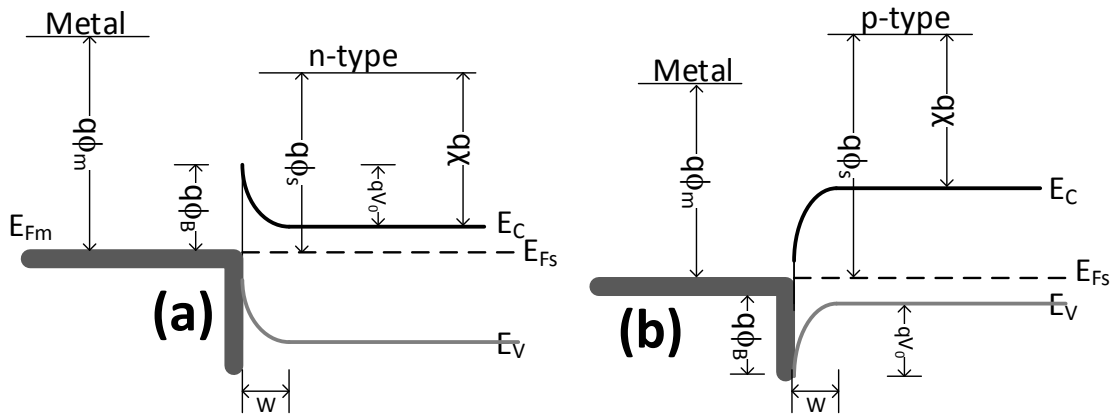


Figure 2.2. Energy band diagram of metal-semiconductor Schottky contact; (a) Metal and n-type semiconductor; (b) Metal and p-type semiconductor.

At the interface itself the vacuum level is same for the two sides such that there is a barrier due to the difference between ϕ_m and χ . This difference, the ideal barrier of the junction, ϕ_B , is given by the following equation 2.2

$$q\phi_B = q(\phi_m - \chi) \quad 2.2$$

The rectifying effect of the Schottky contact is due to the formation of this barrier height ($q\phi_B$) at the junction. So it is important to note that the condition to form a Schottky barrier for a n -type semiconductor is $\phi_m > \phi_s$ and for p -type semiconductor is $\phi_m < \phi_s$. For n -type semiconductor as the distance from the interface increases, the conduction band bends to match with the bulk region value. This band bending builds an electric field which sweeps free electrons from the vicinity of the contact interface and creates fixed positive charge distribution due to ionized donors and thus forms a depletion region (also known as space charge region). The bands become flat at the edge of depletion region and the electric field falls to zero at the edge which persists throughout the semiconductor. In the metal side a neutralizing negative charge is accumulated at the contact. A Schottky junction consists of a space charge region (entirely depleted of mobile charge) and an electrically neutral bulk region where they are separated by a sharp interface [44].

Electrons coming from the n -type semiconductor into the metal face a barrier known as built-in voltage (V_{bi}) are obtained from $\phi_m - \phi_s$. The barrier faced by holes moving from p -type semiconductor to metal is $\phi_s - \phi_m$. The depletion width for a Schottky barrier on an n -type semiconductor can be obtained following expression [45],

$$W = \sqrt{\frac{2 \times V_{bi} \times \epsilon \times \epsilon_0}{q \times N_D}} \quad 2.3$$

where ϵ is the dielectric constant of the semiconductor material, ϵ_0 is the permittivity of vacuum, q is the electronic charge (1.6×10^{-19} C) and N_D is the effective doping concentration and V_{bi} is the built-in potential. For n-type semiconductor the built-in voltage V_{bi} is given by

$$V_{bi} = \phi_B - \frac{kT}{q} \ln\left(\frac{N_C}{N_D}\right) \quad 2.4$$

A forward bias opposes the built-in voltage and reduces the overall band bending while a reverse bias does the opposite.

2.3.4 Carrier Transport Mechanism

The current transport in metal-semiconductor contacts is mainly due to majority carriers. The various electrons transport mechanisms across a metal – semiconductor junction under a forward bias are as follows [46]:

- a. Electron thermionic emission over the top of the barrier (holes for p -type material) in which electrons with energies greater than the barrier height can pass across the junction
- b. Quantum mechanical tunneling which is important for heavily doped semiconductors where the depletion width is small.
- c. Depletion width is small. Recombination in the space charge region

d. Recombination in the neutral region.

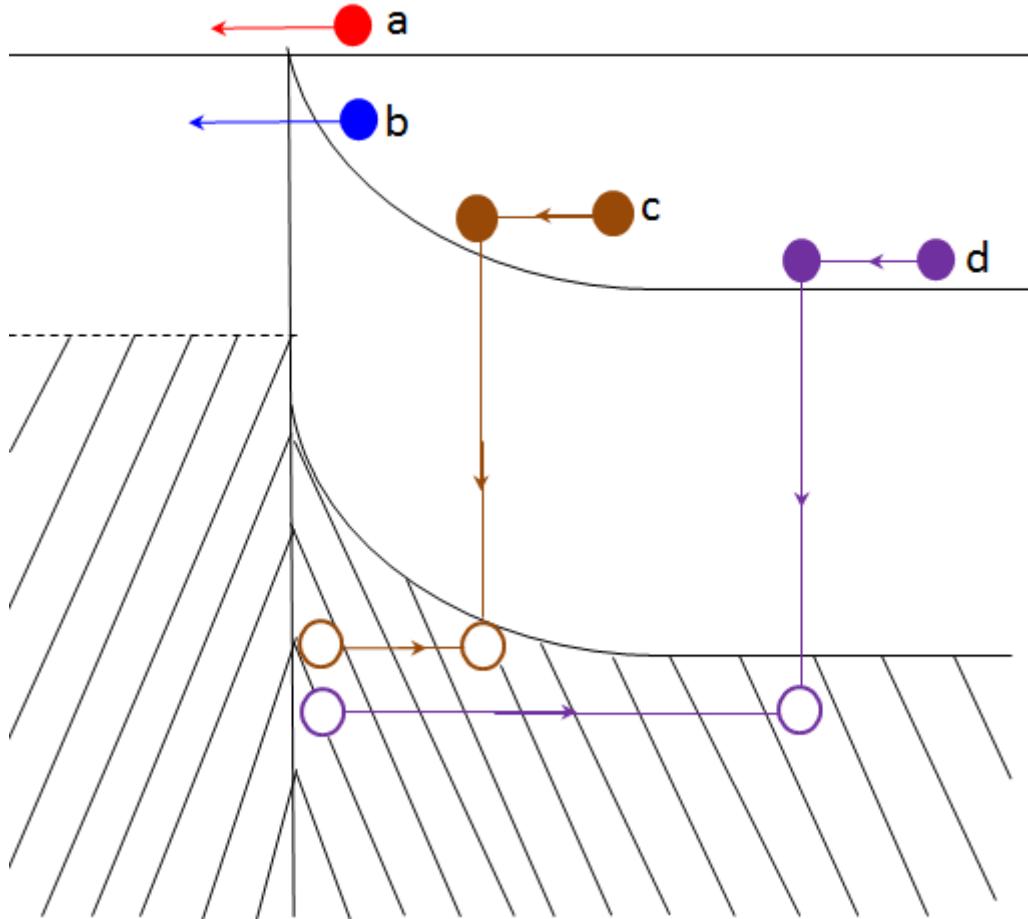


Figure 2.3. Transport process in a forward biased Schottky barrier

The four different electron transport mechanisms are shown in Figure 2.3. Besides this, edge leakage current may flow at the contact periphery due to high electric field. There may also be current flow due to traps at the metal-semiconductor interface. The inverse process happens under the reverse bias. In ideal cases, the current flows mainly by the process (a). The other processes (b), (c), and (d) are responsible for the departures from ideality. The electron emission over the barrier from semiconductor to metal is

governed by two basic processes: (i) electrons transport from the bulk semiconductor and across the depletion region by diffusion and drift in the barrier electric field and (ii) the electron emission at metal-semiconductor interface which is determined by the rate of transfer of electrons across the boundary. According to the diffusion theory of Schottky [47], the first process is dominant one. According to Bethe thermionic–emission theory [48], the second process, the actual transfer of electrons across the metal-semiconductor interface, is a current limiting factor.

2.3.5 Current-Voltage (I-V) Analysis

Many semiconductor devices; such as *p-n* and Schottky junctions, solar cells, photodiodes, MOSFET etc., electrical performances are evaluated through current-voltage (I-V) characteristics. The performance level and degradation are highly dependent upon the material, the operating current flowing through the device and series resistances. The voltage dependent junction current in a Schottky contact can be expressed as [46]:

$$I = I_s(e^{\frac{\beta V}{n}} - 1) \quad 2.5$$

where I_s is the saturation current, V is the applied voltage, n is the diode ideality factor, $\beta = q/k_B T$, q being the electronic charge (1.6×10^{-19} C), k_B the Boltzmann constant (8.62×10^{-5} eV/K), and T is the absolute temperature (°K). The saturation current is given by Equation 2.6

$$I_S = A^* A T^2 (e^{-\beta \phi_B}) \quad 2.6$$

where A is the area of the diode, ϕ_B is the Schottky barrier height, and A^* is the effective Richardson constant which can be expressed as [49]

$$A^* = 4\pi^2 m^* / h^3 = 120 (m^* / m) A cm^{-2} K^{-2} \quad 2.7$$

where h is Planck constant, and m^* is the electron effective mass .

Plot of $\log(I)$ vs. V will be a straight line if I_0 and n are constant. The voltage across the diode becomes $V_d = V - IR_s$, where R_s is the series resistance of the diode and V is the measured voltage across the entire diode including contact resistance as well as other resistance components.

$$I = I_S (e^{\frac{\beta(V-IR_s)}{n}} - 1) \quad 2.8$$

By taking the logarithm the equation 2.6 can be written as

$$\log(I) = \frac{\beta V}{n} + \log(I_S) \quad 2.9$$

which is an equation of straight line where $\frac{\beta}{n}$ is the slope and $\log(I_S)$ is the intercept as shown in Figure 2.4. The plot gives a straight line over the range where the condition $IR_s \ll V$ and $k_B T/q \ll 1$ are satisfied. The plot deviates from straight line for lower current due to the term -1 in the parenthesis of the equation and deviates from

straight line for higher current due to series resistance. The slope and the intercept can be easily calculated using a linear regression of $\log(I)$ vs V plot obtained from I-V measurements. As the sample temperature is known, the ideality factor is obtained from the measured slope according to the equation 2.10.

$$n = \frac{1}{\text{slope} \times 1/\beta} \quad 2.10$$

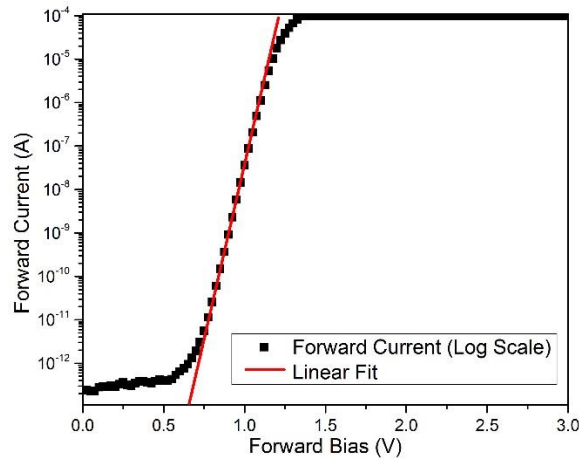


Figure 2.4. Linear fit of current-voltage (I-V) acquired data plotted in logarithmic scale

The reverse saturation current I_s is obtained by extrapolation of the straight line portion of the curve, and surface barrier height is calculated from the equation. The diode ideality factor gives the uniformity of surface barrier height across the detector surface [50]. An ideality factor greater than unity, indicates the presence of patches (i.e. presence of generation-recombination centers) on the detector surface where the surface barrier height is considerably lower than the rest of the surface [51].

2.3.6 Capacitance-Voltage (C-V) Analysis

The voltage dependence of the capacitance (C-V) measurement relies on the fact that the depletion region width of a semiconductor junction depends upon the applied voltage. The effective doping concentration (N_D) in the active region of a Schottky diode or p-n junction can be obtained from the C-V measurement. The knowledge of effective doping concentration allows the calculation of the depletion width under certain applied bias (According to Equation 2.11) and also the determination of full depletion bias. In order to calculate the doping concentration and the built-in voltage, analysis of the data acquired from capacitance-voltage (C-V) measurements is needed.

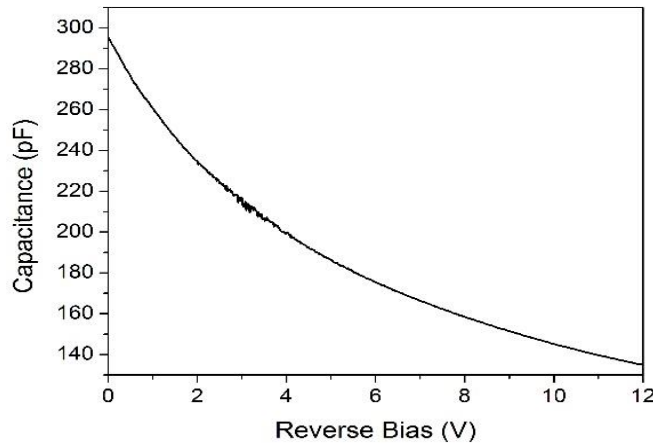


Figure 2.5. Capacitance-voltage data acquired using a Schottky diode.

Figure 2.5 shows a C-V measurement conducted on a Schottky device. The capacitance can be seen decreasing with the increase in reverse bias because the capacitance is inversely proportional to the depletion width as is shown in Equation 2.11 and the depletion width in a *p-n* junction or Schottky diode increases as reverse bias increases. Mathematically, the capacitance of a Schottky diode can be expressed as [52],

$$C = \frac{\epsilon \times \epsilon_0 \times A}{W} = A \left[\frac{\epsilon \epsilon_0 N_D}{2(V_{bi} + V)} \right]^{1/2} \quad 2.11$$

where the symbols have their usual meaning.

The variation in capacitance as a function of reverse bias is given by

$$\frac{1}{C^2} = \frac{2V_{bi}}{A^2 q \epsilon \epsilon_0 N_D} + \frac{2V}{A^2 q \epsilon \epsilon_0 N_D} \quad 2.12$$

which is a straight line equation in a $1/C^2$ vs. V plot. The doping concentration N_D is calculated by the following equation:

$$N_D = \frac{2}{A^2 q \epsilon \epsilon_0 \times slope} \quad 2.13$$

The first term of Equation 2.12 allows calculation of the built-in voltage (V_{bi}) using the intercept obtained from the linear fit. Figure 2.6 shows one such linear $1/C^2$ vs. V plot obtained for a Schottky diode.

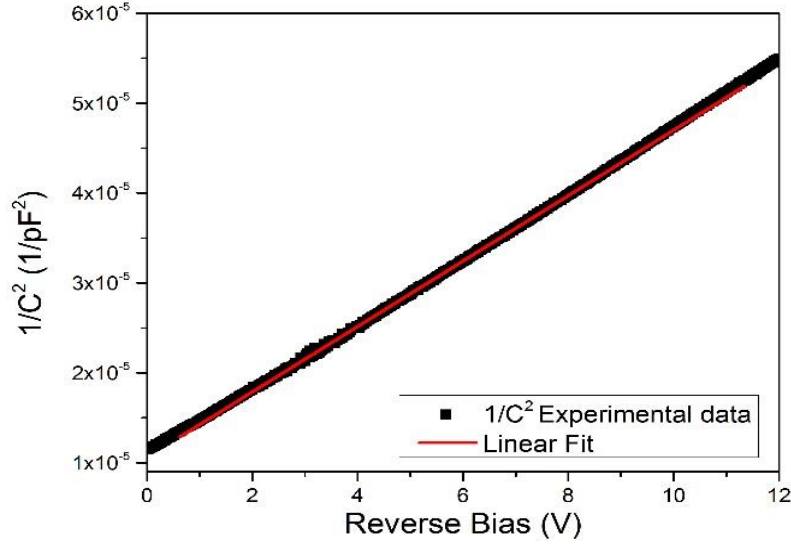


Figure 2.6. $1/C^2$ vs. reverse bias plot with linear fitting. Variation of $1/C^2$ as a function of reverse bias corresponding to the C-V plot shown in above . The straight line shows the linear fit of the experimental data.

2.4 CONCLUSION

In this chapter material properties and the crystal structure of SiC are discussed. The crystal growth process for both bulk and epitaxial layer are also described briefly. The theoretical concepts of the device's structure used in the experiments of this thesis are explained here. For the detector fabrication, it is important to understand how to obtain the desired type of metal-semiconductor contact, e.g. Ohmic or Schottky. For Schottky contacts, the thermionic emission model is described in order to study the contacts' properties in SiC diodes in terms of the barrier height and the ideality factor using current-voltage (I-V) measurements. For further characterization of the Schottky contact, the calculation procedures for doping concentration and built-in voltage using capacitance-voltage (C-V) measurements are described.

CHAPTER 3: DEFECTS IN SIC

3.1 OVERVIEW

Defects in semiconductors can be classified as: point defects and extended defects. Point defects are localized in a lattice site, involving only a few nearest neighbors and not extended to any spatial dimensions. Extended defects, such as, grain boundaries, dislocations and/or stacking faults, are extended in all dimensions and will be discussed in the next section. This chapter will discuss on the defects and their detrimental properties.

3.2 POINT DEFECTS

Point defects exist in small concentrations in all semiconductor materials and formed mainly due to vacancies, interstitials, and substitutions. Aggregation of few point defects which generate a perturbation in a lattice site and its immediate vicinity, such as, divacancies, vacancy–donor complexes, are also considered as point defects. Point defects introduce electronic energy states within the semiconductor band-gap which can act as, ‘traps’, ‘recombination centers’, or ‘generation centers’ and may modify the semiconductor properties and device performances significantly. The point defects are

desirable for some devices and introduced intentionally. As for example, in switching devices, energy levels introduced by point defects can be used as recombination centers which help to remove minority carriers quickly during turning off and enhance the device's switching speed thereby increasing efficiency [53, 54]. However for many cases point defects are detrimental to the device performances. Energy states created by point defects may act as a recombination centers for the generated electron-hole pairs and degrade the performance of radiation detectors and photovoltaic solar cells. Point defects and their characterization will be discussed in detail in chapter five of this dissertation.

3.3 MORPHOLOGICAL DEFECTS

Most SiC devices are fabricated in such a way that their electrically active regions reside entirely within the epilayer grown on bulk crystal substrate. The electrical characteristics of these devices critically depend on the quality and smoothness of the semiconductor surface. So the defects contained in the epilayer are of great interest to any opto-electrical devices. The defects in SiC epilayer that impact electrical device performances are threading screw dislocation (TSD), threading edge dislocation (TED), basal plane dislocation (BPD), small growth pits, triangular inclusions, carrots, and comet tail defects [55, 56, 57]. Lot of defects originated in bulk cannot propagate to the epilayer, so the epitaxial layer contains significantly fewer defects than bulk wafers.

3.3.1 Threading Screw Dislocation (TSD) and Micropipes

Threading screw dislocation (TSD) can penetrate along the crystallographic c -axis through the entire length of the crystal. Screw dislocations terminate only in the crystal surface and are present in all wafers cut from the grown crystal. This screw dislocation can propagate throughout the whole thickness of epitaxial layer grown by CVD technique. Additional screw dislocation may also form during the epitaxial growth [58, 59]. Extended screw dislocation is usually measured by the length of the Burgers vector (b). For pure screw dislocation the Burgers vector is parallel to the crystallographic c -axis and the Burger vector length is related to the step height of the screw dislocation.

Screw dislocation with large Burger vector forms hollow cores and is widely known as micropipes. Micropipes are hollow tubular defects penetrating the SiC single crystals and their radius ranges from a few tens of nanometers to several tens of micrometers. The performance of SiC based power devices and radiation detectors is severely degraded by these micropipes [56, 60, 61]. Substrate micropipe defects with an area of 1 mm^2 or larger may cause pre-avalanche reverse-bias point failure in epitaxially grown p - n junction devices. With the steady development of the material growth process, the micropipe densities have been reduced drastically (from 10^4 cm^{-2} to less than 1 cm^{-2}) and recently vendors have grown micropipe-free epitaxial layers [57].

The SiC screw dislocation with small Burgers vector forms close core and sometimes termed as elementary screw dislocations which exist at densities on the order

of thousands per cm^2 in 4H- and 6H-SiC wafers and epilayers [62]. Close core dislocation is not as detrimental as micropipes, however, experimentally it is proven that these defects have negative impact on device performances [63]. It is found that soft breakdown (at voltage <250 V) in 4H-SiC p - n junction diodes may happen due to these close core dislocation [64]. Wahab *et al.* showed that increasing density of close core dislocations in the active region can cause the degradation of the breakdown voltages [65].

3.3.2 Basal Plane Dislocation (BPD)

Basal plane dislocations (BPDs) probably have the highest density of all the dislocations. BPDs form to relaxation of the thermal stress which mainly occurred during cooling down from high growth temperature to room temperature. BPDs in p - n diodes may dissociate into two Shockley partials and cause an increase of forward voltage drop [66]. Basal plane tilt low angle grain boundaries due to the pile-up of BPDs [67].

3.3.3 Threading Edge Dislocation (TED)

Threading edge dislocation (TED) is an edge type dislocation which has Burgers vectors perpendicular to along the c -axis of the crystal. TEDs are mostly inherited from the substrate. Basal plane dislocations (BPDs) propagate from the off-axis 4H-SiC substrate into the homoepitaxial layer and convert into threading edge dislocations in the epitaxial layer. The conversion from BPDs to TEDs happens due to the image force in the

epilayers. The converted dislocations are inclined from the c-axis toward the down-step direction by about 15° [68]. Ha *et al.* [69] suggest that TEDs may also form due to prismatic plane slip.

3.3.4 Staking Faults

Staking faults (SFs) are kind of planar defects and exist mostly in the primary slip plane $\{0001\}$ of SiC. SFs occur due to the deviation of Si–C bilayers from the perfect stacking sequence along the c-axis of the crystal. SFs reduce the barrier height and the breakdown voltage of a Schottky diode. An electrostatic potential may appear in SiC *p-i-n* diodes due to the charge accumulation in the stacking faults and can increase the forward voltage drop in the diode [68].

3.4 MORPHOLOGICAL DEFECTS DELINEATION BY ETCHING

Chemical etching of silicon carbide is the most versatile way to characterize silicon carbide crystals and has been used effectively to evaluate the crystal qualities. Most of the chemicals used in chemical etching process are used in molten state. Since the sublimation temperature of SiC is 2830°C , it is possible to etch SiC at temperature as high as 1200°C . Due to high amount of hazards involved in etching SiC at such high temperature, a new method of etching SiC at low temperature is absolutely necessary. Molten KOH etching is the widely used method of etching to investigate the growth defects in SiC wafers. SiC etching by molten KOH is an isotropic etching which is a non-

directional etching with uniform etch rate in all directions of the wafers. So molten KOH remove the SiC surface layers at the same etch rate in all directions irrespective of the crystal orientation.

3.4.1 Experimental Procedure for SiC Etching

In our studies, etching studies have been conducted for bulk 4H-SiC crystals and 4H-SiC epitaxial layers. The epilayers were grown by chemical vapor deposition on ~ 350 μm 4H-SiC thick substrate. Both the bulk and the epitaxial layers were diced into 10 \times 10 mm² size. Before etching, the samples have been cleaned thoroughly by an established procedure. This involved cleaning tri-chloro-ethylene (TCE) for 5 minutes and cleaning in HF and acetone for 5 min successively. A nickel crucible, inert to molten KOH, was used for holding the dry KOH pellets. A hot plate was used for heating the nickel crucible containing the KOH pellets. The temperature of the crucible is monitored by a thermocouple and the temperature was controlled with the help of a knob of the hot plate. The temperature is gradually increased to 500 °C to melt the KOH pellets. The SiC samples were immersed into the molten KOH with the help of a specially designed sample holder. The sample holder is also made from a thick nickel sheet. Throughout the etching period, KOH solution temperature is kept constant (~ 500 °C) by adjusting the power knob of the hot plate. After 20 minutes of etching, the samples were taken out from the solution and quickly washed by acidified water to neutralize the KOH. After repeated cleaning by DI water, the samples were finally cleaned with acetone. The whole etching experiment was carried out inside the chemical hood in the advanced

microelectronic materials laboratory at USC. A very thin layer (~ 5 nm) of gold was deposited on the etched surface of SiC samples for SEM studies.

3.4.2 Result of SEM Studies

Figure 3.1 shows the SEM image of a Si-face etched bulk SiC crystal. In the SEM images observed pits with hexagonal shapes are correlated to three types of dislocations. Hexagonal pits with a small black spot in the center are the closed-core screw dislocations [70, 71, 72]. The larger hexagonal pits with a hollow core in the center are considered as the open-core screw dislocations (micropipes) [73, 74]. Hexagonal pits without any center spot are the threading edge dislocations [72, 73]. The hexagonal pits images corresponding to the threading edge dislocations are less bright than those of open core or close core dislocations. In the SEM image shown in Figure 3.1 (b), the basal plane dislocations are appeared as sharp elongated lines which are formed by the interconnection of a series of asymmetrical pits. Figure 3.2 shows the magnified images of the following observed dislocations.

Figure 3.3 (a) shows the SEM images of etched SiC epitaxial layers. The experimental set up and etching process was kept exactly the same for both bulk and epitaxial layers. Figure 3.3 (b) shows the enlarged SEM images of closed core dislocations and threading edge dislocations of the epitaxial layers. The densities of the identified dislocations are much lower in the epitaxial layer compared to the bulk

crystals. Micropipes and BPDs are not observed in the SEM images of the etched epitaxial layers.

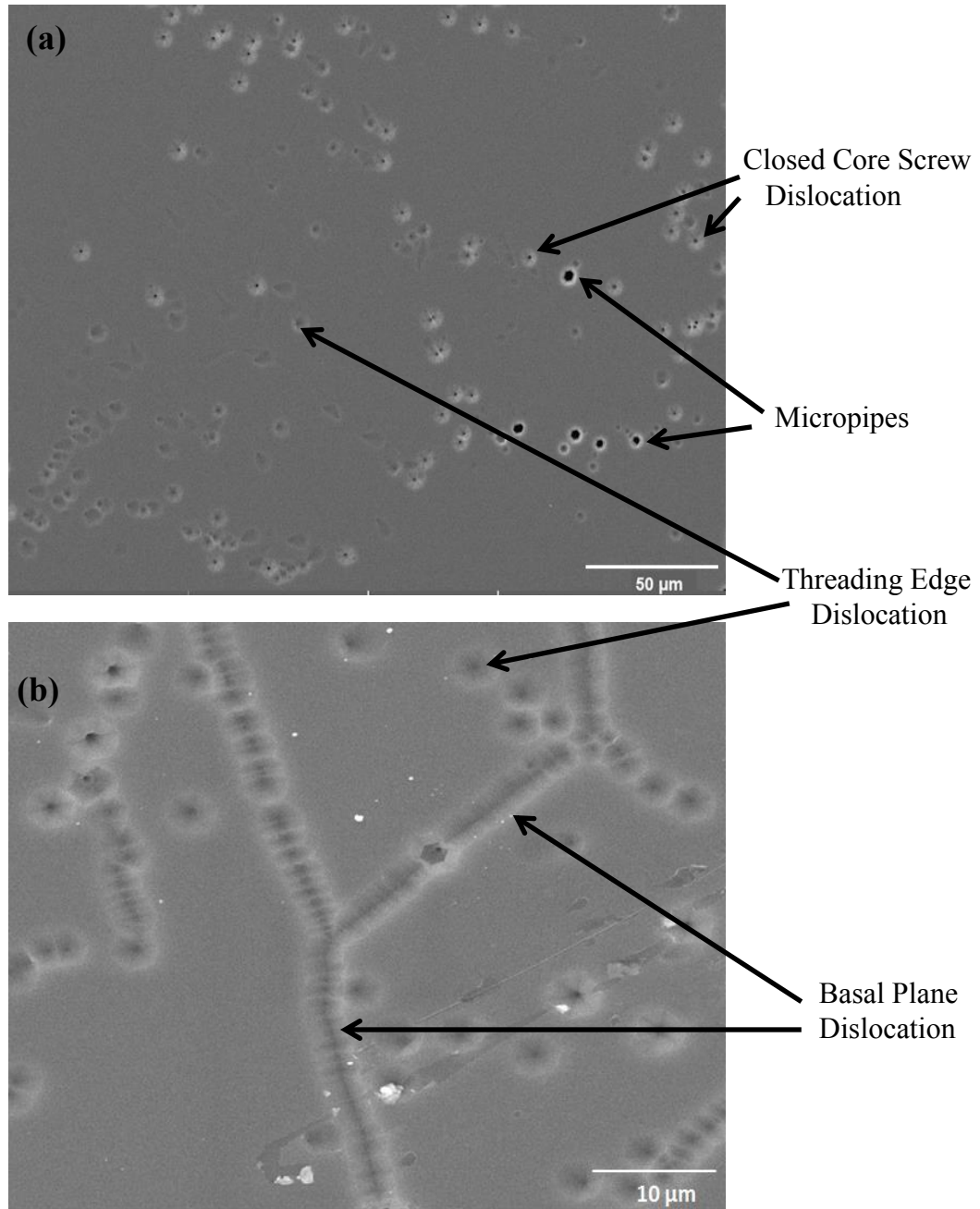


Figure 3.1. SEM image of the molten KOH etched bulk SiC: (a) Region with TSDs and TEDs; (b) Regions with BPDs and TEDs.

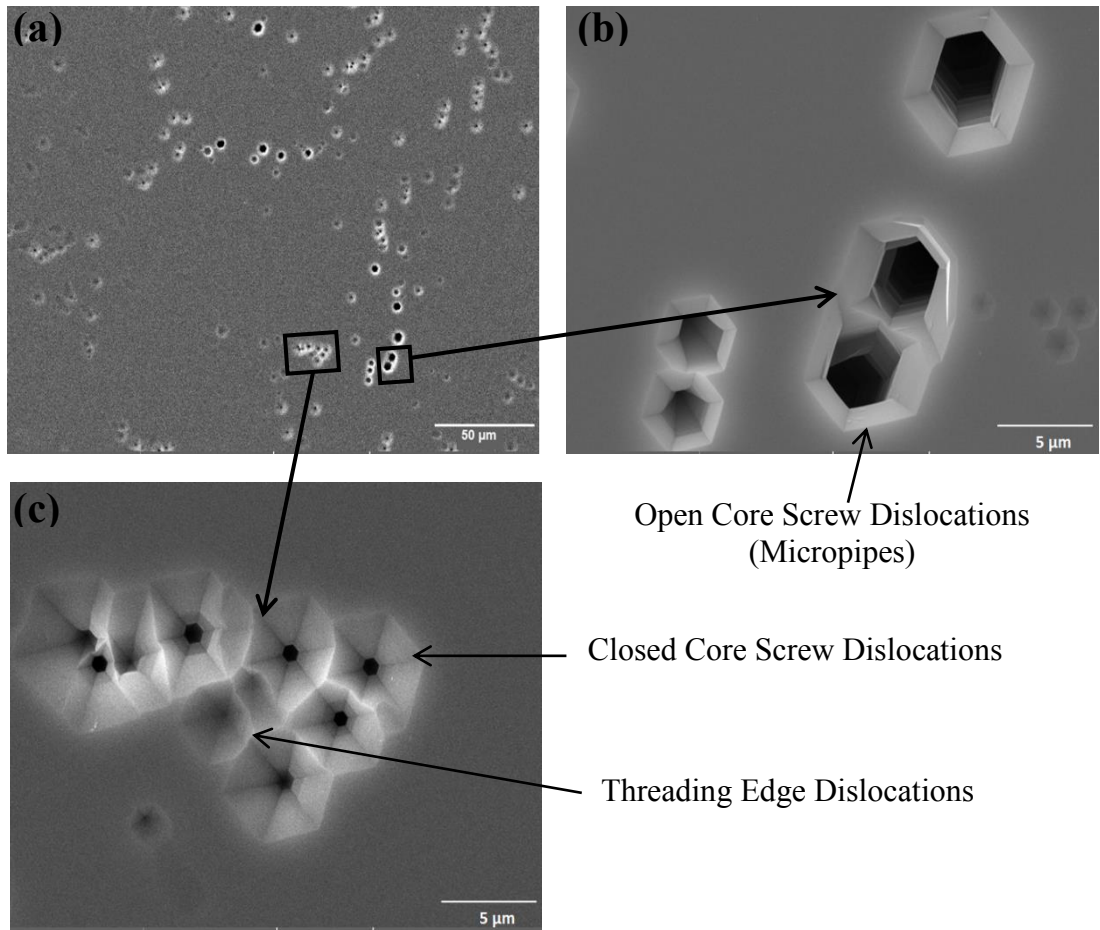


Figure 3.2. SEM images of the molten KOH etched bulk SiC: (a) Region with TSDs and TEDs; (b) Enlarge images of micropipes; (C)) Enlarge images of closed core and threading edge dislocations.

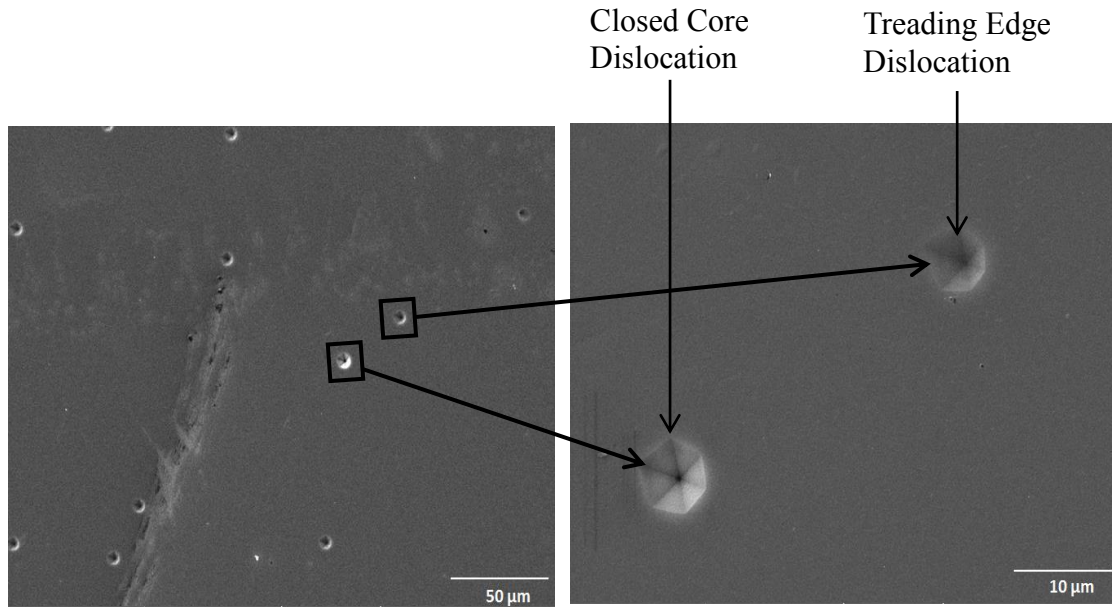


Figure 3.3. (a) SEM images of the molten KOH etched SiC epitaxial layers; (b) Enlarged images of closed core and treading edge dislocations.

3.5 CONCLUSIONS

Various defects of SiC bulk crystals and epitaxial layers are evaluated and analyzed in this chapter. Different kinds of extended defects are also discussed in this chapter. Etching studies have been performed to delineate the extended defects in bulk crystals and epilayers of SiC. The samples were etched for 20 minutes in molten KOH at 500 °C. SEM images of etched samples were taken to depict the types of defects. In the bulk crystal, threading screw dislocations (open core and closed core), threading edge dislocations, and basal plan dislocations are observed. In the epitaxial layers, only the closed core screw dislocations and treading edge dislocations are observed. From the SEM studies it is found that open core screw dislocations (micropipes) and basal plan dislocations, which are detrimental for device performance, are not found in the epitaxial

layers. Moreover the densities of the delineated defects in the 4H-SiC epitaxial layers are much less compared to the bulk crystals. So it is clear that substantial amount of bulk crystal defects are not being propagated to the epitaxial layers during the epitaxial growth.

CHAPTER 4: DETECTOR FABRICATION AND CHARACTERIZATION

4.1 4H-SiC DETECTOR FABRICATION

50 μm thick n-type epilayers were grown by chemical vapor deposition (CVD) on 4H-SiC (0001) n-type substrate. The substrate is highly doped with nitrogen and was off-cut 8° towards $[11\bar{2}0]$ direction. Nomarski optical microscopy and scanning electron microscopy (SEM) revealed a micropipe defect density of less than 1 cm^{-2} . The 76 mm diameter wafer was diced into $10 \times 10 \text{ mm}^2$ size pieces as is shown in Figure 4.1.

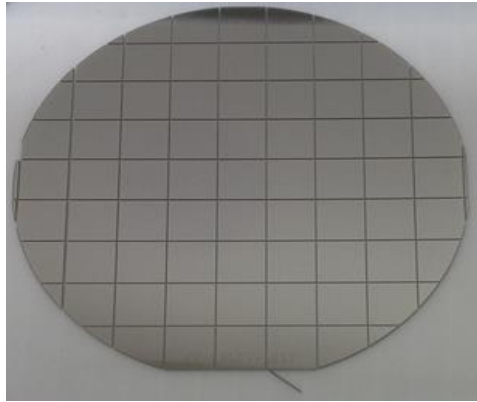


Figure 4.1. Photograph of an n-type 4H-SiC epitaxial layer wafer.

Before contact deposition, a RCA (Radio Corporation of America) standard wafer cleaning procedure was applied. This process starts with the removal of organic contaminants (dust particles, grease, etc.) from the wafer surface using organic solvents

(trichloroethylene, acetone, and methanol) at their respective boiling temperatures. Any organic residue left by the first step is then processed using sulfuric acid (H_2SO_4) and ammonium hydroxide (NH_4OH) solutions (with hydrogen peroxide). These solutions are designed to attack the organic impurities by dehydration and oxidation of the carbon present forming oxide at the surface of the wafer. Finally, these oxide layers were etched with hydrofluoric acid (HF).

The Schottky barriers were formed on the epitaxial layers (Si face) by depositing thin (10 nm) circular Ni contacts (area $\sim 11.95 \text{ mm}^2$). 100 nm thick square ($\sim 64 \text{ mm}^2$) Ni back contacts were deposited on the C face of the 4H-SiC substrates. A Quorum model Q 150T DC sputtering unit was used to deposit the metal contacts. The cross-sectional schematic of the fabricated Schottky barrier radiation detector is shown in Figure 4.2.

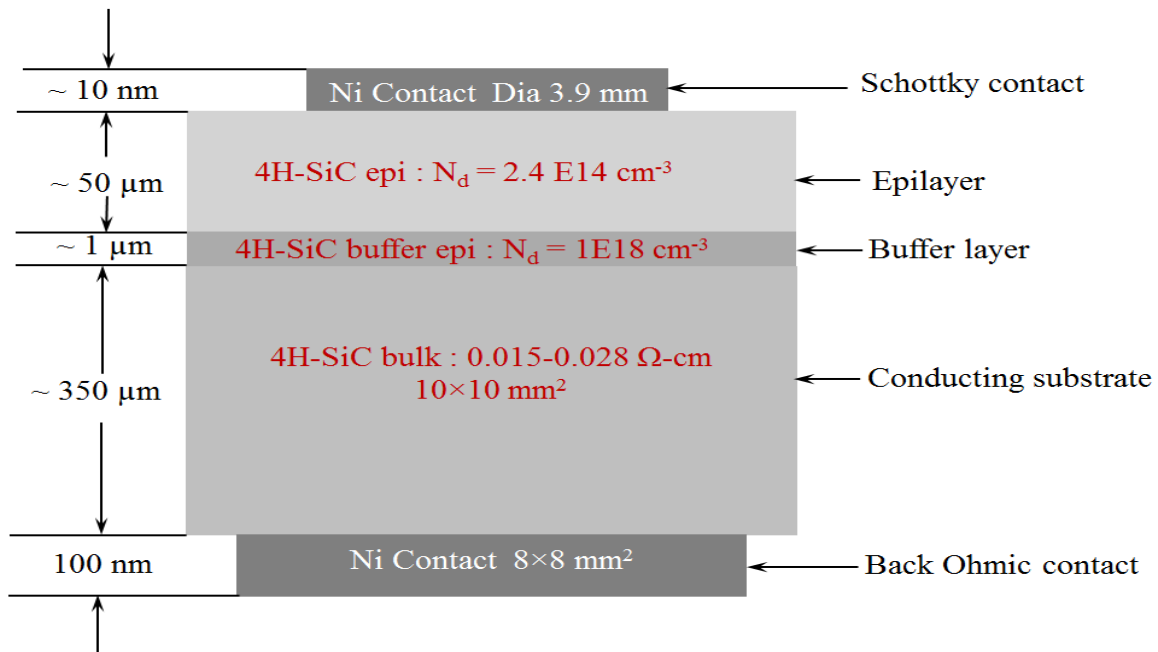


Figure 4.2. Schematic diagram of the cross-sectional view of 50µm thick n-type 4H-SiC Schottky barrier device.

4.2 ELECTRICAL CHARACTERISTICS OF FABRICATED DETECTOR

Current-voltage (I-V) and capacitance-voltage (C-V) measurements were conducted in order to investigate the electrical properties of the metal-semiconductor contact. The I-V measurements were carried out using a Keithley 237 high voltage source-measure unit. Forward and reverse I-V characteristics were acquired to study the behavior of the Schottky contact. C-V measurements were carried out at 100 kHz using a Keithley 590 C-V meter. Figure 4.3 shows the schematic and the arrangement of the equipment setup used to perform the I-V and C-V measurements.

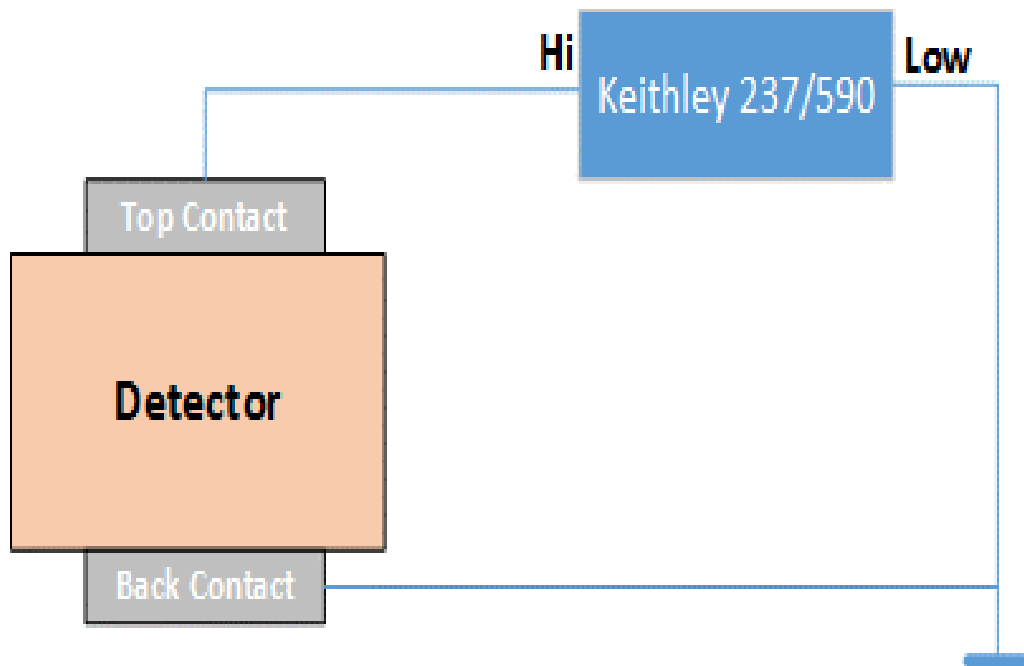


Figure 4.3. Schematic of the I-V and C-V experimental setup.

The picture of the I-V and C-V measurement system at USC is shown in Figure 4.4. To minimize the influence of external electrical and optical signal, the detector is mounted in an EMI shielded aluminum box during the measurement.

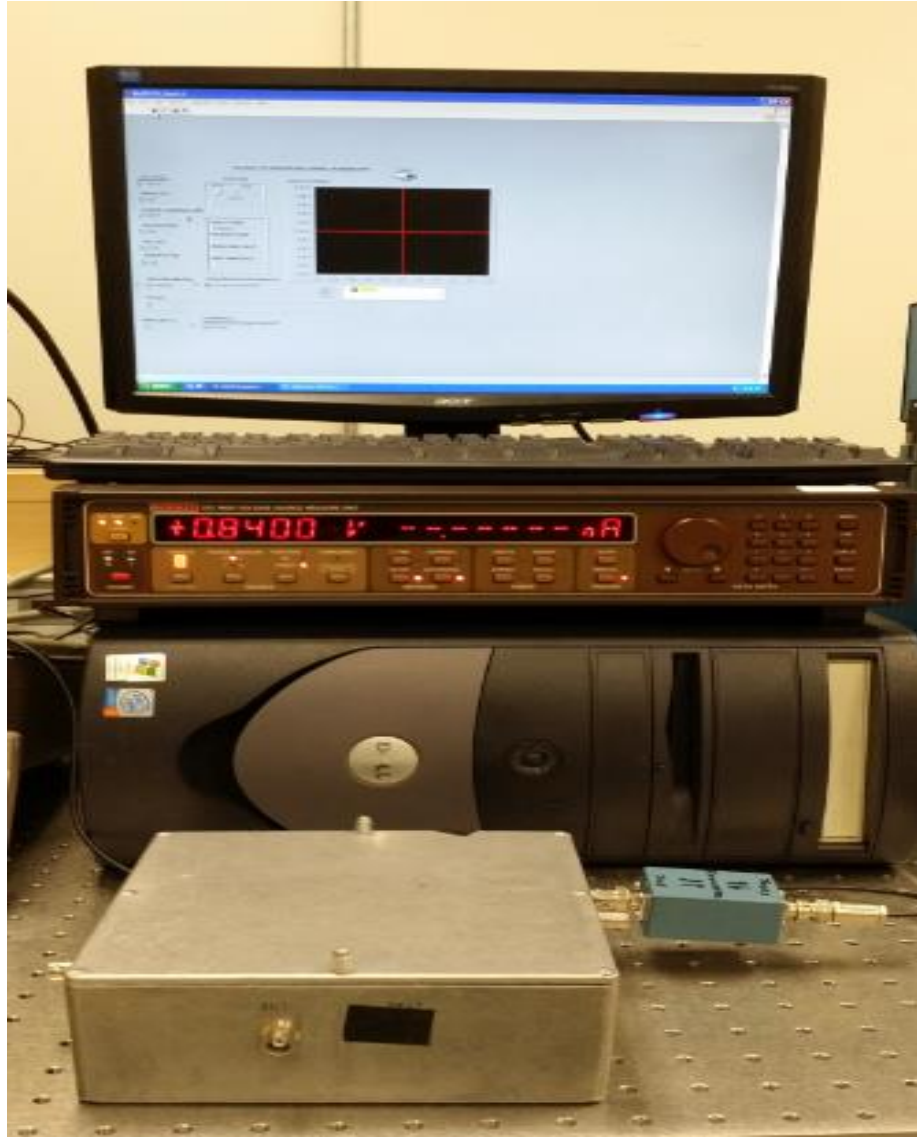


Figure 4.4. Photograph of the experimental setup for the I-V and C-V measurements. The detector is mounted inside the aluminum box.

4.2.1 Current-Voltage (I-V) Characteristics

In order to identify the electrical properties of the detectors, I-V characteristics of the detectors at forward and reverse bias were measured at room temperature. The forward response is used to study the behavior of the Schottky contacts using the thermionic emission model mentioned in Section 2.4 in terms of barrier height and the diode ideality factor. The reverse I-V characteristics give the magnitude of the leakage current under operating conditions.

The I-V characteristics of the Schottky barrier radiation detector (AD06) fabricated on 50 μm 4H-SiC epitaxial layer is shown in Figure 4.5. From the forward I-V characteristic, the diode ideality factor was calculated to be 1.2 which suggests the presence of spatial non-uniformities in barrier height distribution along the metal contact area. The barrier height for the Ni/4H-SiC Schottky contact was calculated to be 0.95 eV. The reverse bias characteristic of the detector is also shown in Figure 4.5. The leakage current was found to be ~ 9 nA at a reverse bias voltage of - 150 V [75]. Table 4.1 shows the calculated parameters from the forward and reverse bias response of the detector AD06. From the calculated parameters of the Schottky barrier fabricated device, AD06 was determined to be suitable for radiation detection.

Table 4.1. I-V characteristics parameters of the Schottky detector

Diode Name	Current at - 150V	Barrier Height (eV)	Ideality Factor
AD 06	9 nA	0.95 eV	1.2

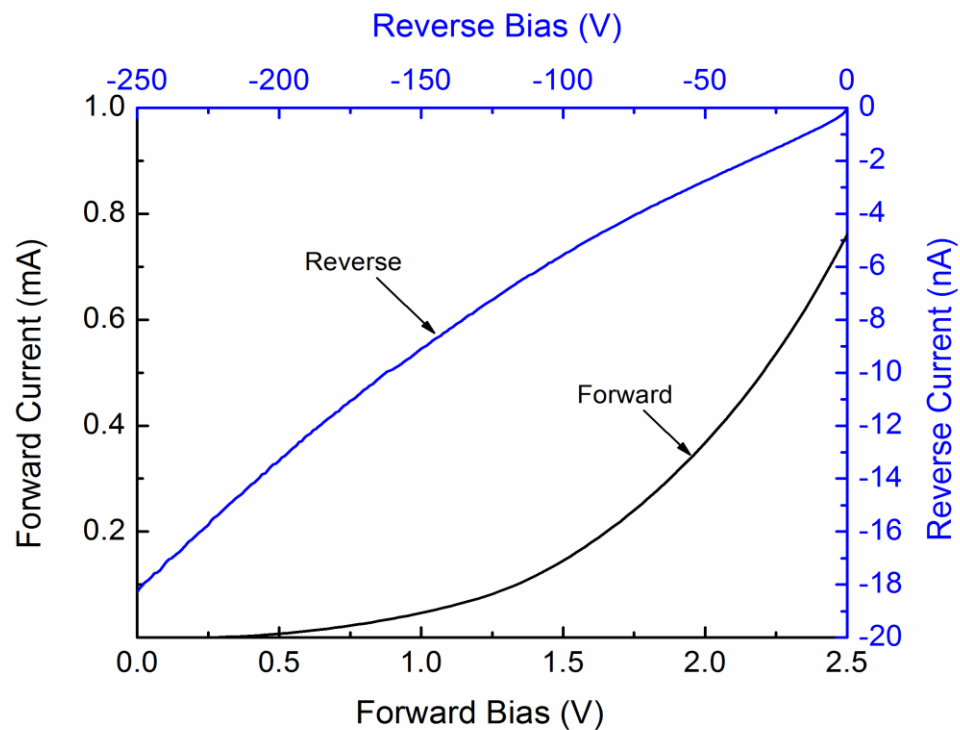


Figure 4.5. Variation of junction current as a function of applied bias for a 50 μm n-type Ni/4H-SiC epitaxial Schottky barrier radiation detector.

In another study, several Schottky barrier radiation detectors were fabricated on 20 μm 4H-SiC epitaxial layer. The Schottky devices were fabricated on 20 μm epitaxial layers that were from the similar type of parent wafer. Three detectors AS1, AS2, and AS3 of high resolution were chosen for analysis. Figure 4.6 shows the forward I-V characteristics of the detectors. The barrier heights of the detectors AS1, AS2, and AS3 were calculated to be 1.6 eV, 1.67 eV, and 1.15 eV, respectively. The ideality factors of the detectors AS1, AS2, and AS3 are found as 1.2, 1.09, and 1.24, respectively.

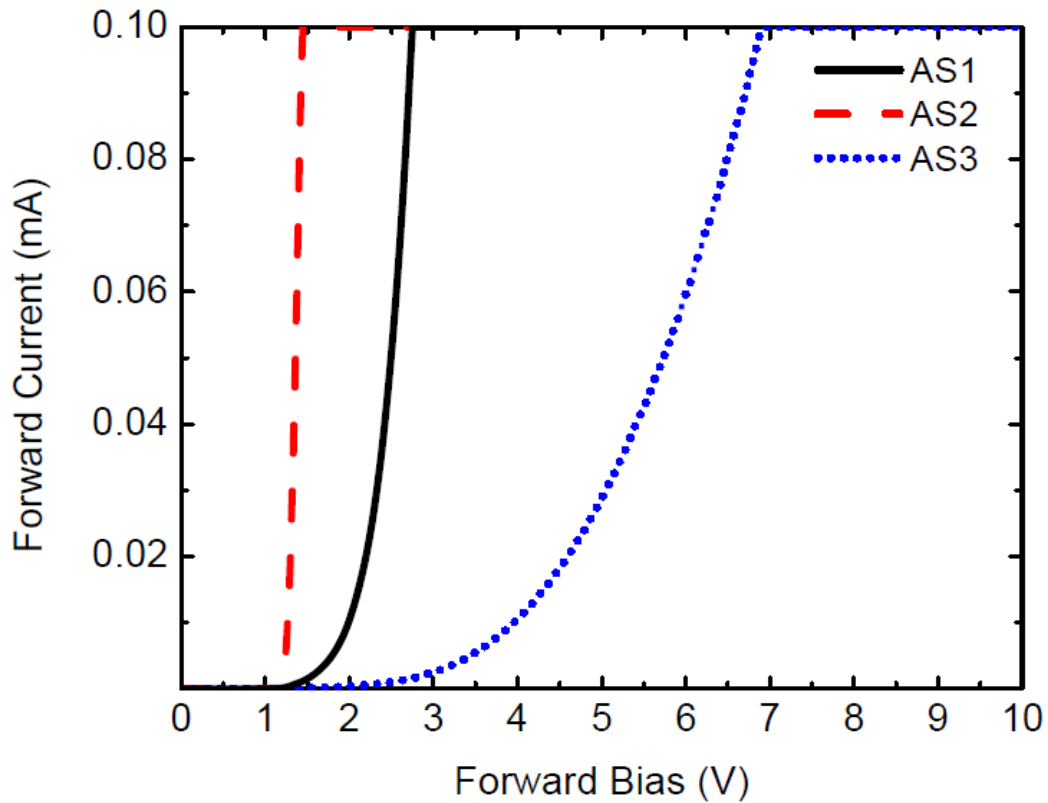


Figure 4.6. Forward I-V characteristics on 4H-SiC epitaxial Schottky barrier detectors AS1, AS2, and AS3.

Figure 4.7 shows the reverse I-V characteristics of the three detectors. The leakage currents at -110 V for AS1, AS2, and AS3 were 4.3 pA, 6.2 pA, and 10.0 pA, respectively. Detector AS1 exhibited the lowest leakage current among these three detectors at the operating voltage (~110 V) of the detectors.

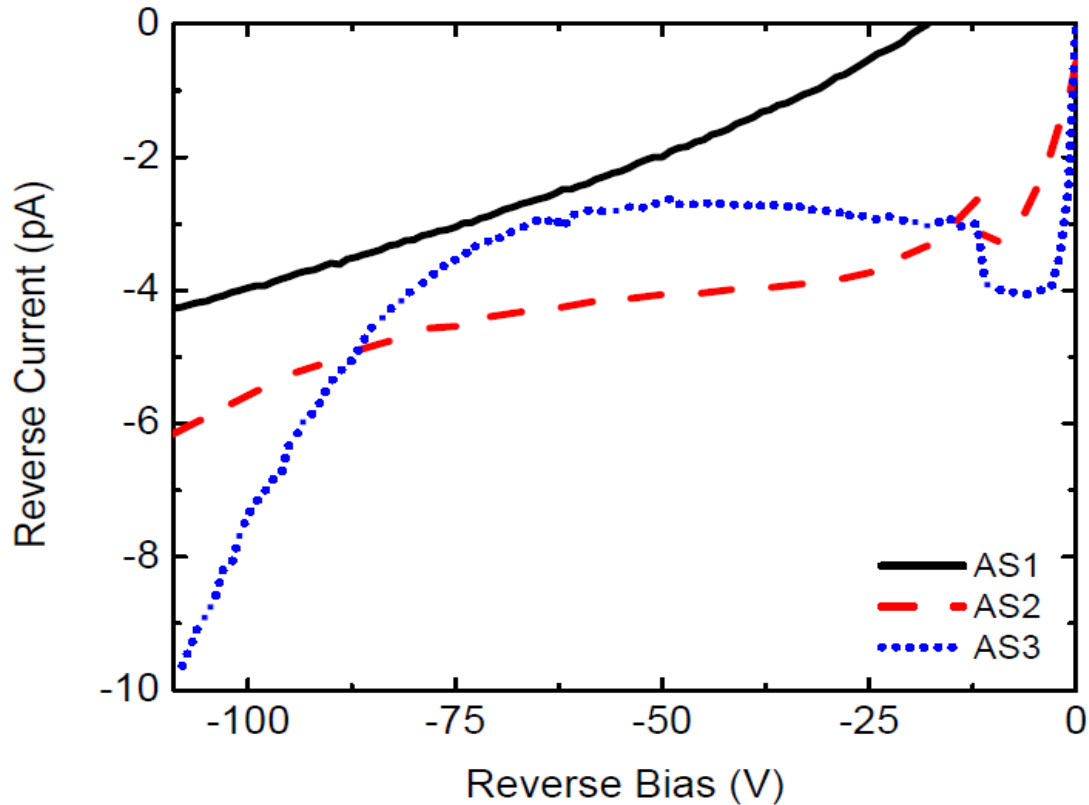


Figure 4.7. Reverse I-V characteristics obtained for 4H-SiC epitaxial Schottky barrier detectors AS1, AS2, and AS3.

4.2.2 Capacitance-Voltage (C-V) Characteristics

Figure 4.8 shows a $1/C^2$ vs V plot, and the inset shows the original C-V plot. In a Schottky metal-semiconductor junction, the depletion region extends to the side of the semiconductor and increases its width with the increase in reverse bias; this property allows control of the depletion width in the epitaxial layer which defines the active region. The active region is where the charge signal due to particle interaction takes place (creation of electron-hole pairs) in the detector. As the capacitance value depends on the contact area and width of the depletion region, as shown in Section 2.4, capacitance is

expected to decrease as reverse bias increases. Further analysis of the acquired data was performed in order to calculate the doping concentration of the epilayer and the built-in voltage of the Schottky contact. As expected, the capacitance values showed a decreasing trend with the increasing reverse bias because of the increase in depletion width. The effective doping concentration (N_{eff}) was calculated to be $1.98 \times 10^{15} \text{ cm}^{-3}$ and the built-in potential (V_{bi}) of the contact was found to be 1.5 V from $1/C^2$ vs V plots.

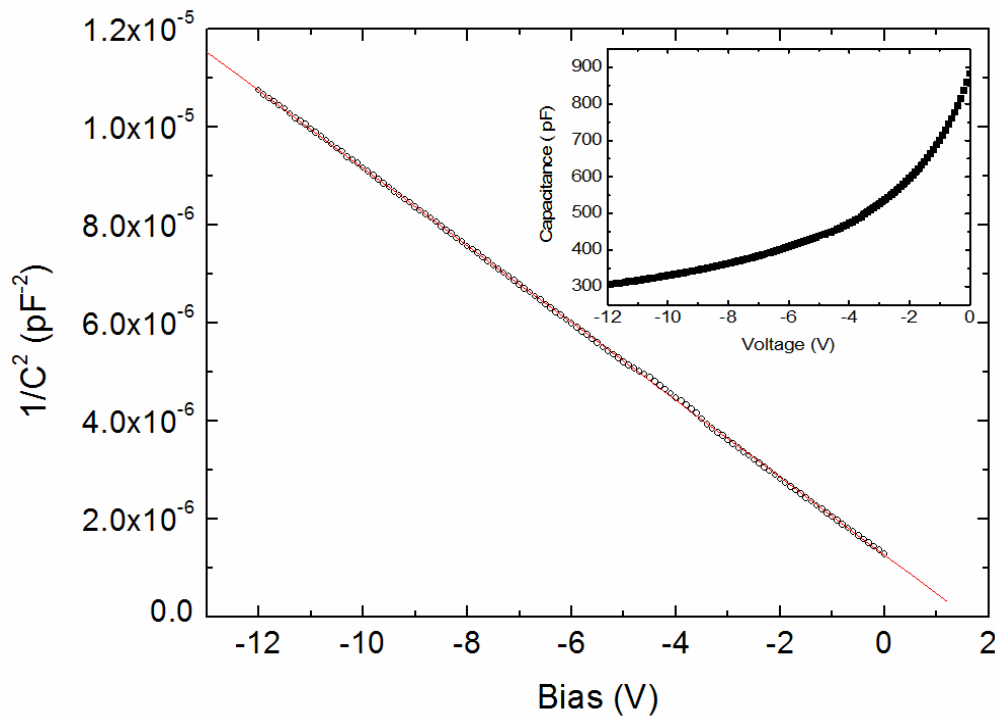


Figure 4.8. $1/C^2$ vs V plot for a 50 μm n-type Ni/4H-SiC epitaxial Schottky barrier detector. The open circles are the experimental data points and the solid line is a straight line fit to the experimental data. Inset shows the original C-V plot.

The Schottky barrier height was also calculated from the C-V characteristics. Considering the standard band diagram for an abrupt p-n junction, the barrier height can be expressed as

$$\Phi_{B(C-V)} = V_{bi} + V_n \quad 4.1$$

where, V_n is the energy difference between the Fermi level and the conduction band minimum and can be expressed as

$$V_n = kT \ln \frac{N_C}{N_{eff}} \quad 4.2$$

where N_C is the effective density of states in the conduction band of 4H-SiC and is taken equal to $1.7 \times 10^{19} \text{ cm}^{-3}$ [76]. The barrier height thus calculated from C-V measurements was 1.7 eV which is higher than that obtained from the forward I-V characteristics. The difference between the two barrier height values can be explained as follows. Barrier height obtained from the forward I-V characteristics is generally dominated by current flow through the low Schottky barrier height locations over the entire metal contact area in an inhomogeneous Schottky diode which results in lower surface barrier height. C-V characteristics, on the other hand, give an average value of the barrier height for the whole diode area [50, 77]. The larger value of barrier height calculated from the C-V measurements reconfirms the spatial inhomogeneity of the surface barrier height as was also inferred from the ideality factor value.

Figure 4.9 shows the $1/C^2$ vs V plots for the three detectors (AS1, AS2, and AS3). The calculated effective doping concentrations for the detectors are the following: AS1 is $2.6 \times 10^{14} \text{ cm}^{-3}$, AS2 is $3.2 \times 10^{14} \text{ cm}^{-3}$, and AS3 is $2.6 \times 10^{14} \text{ cm}^{-3}$. The effective doping concentration was found to be the least for the detector AS1 among all the three detectors.

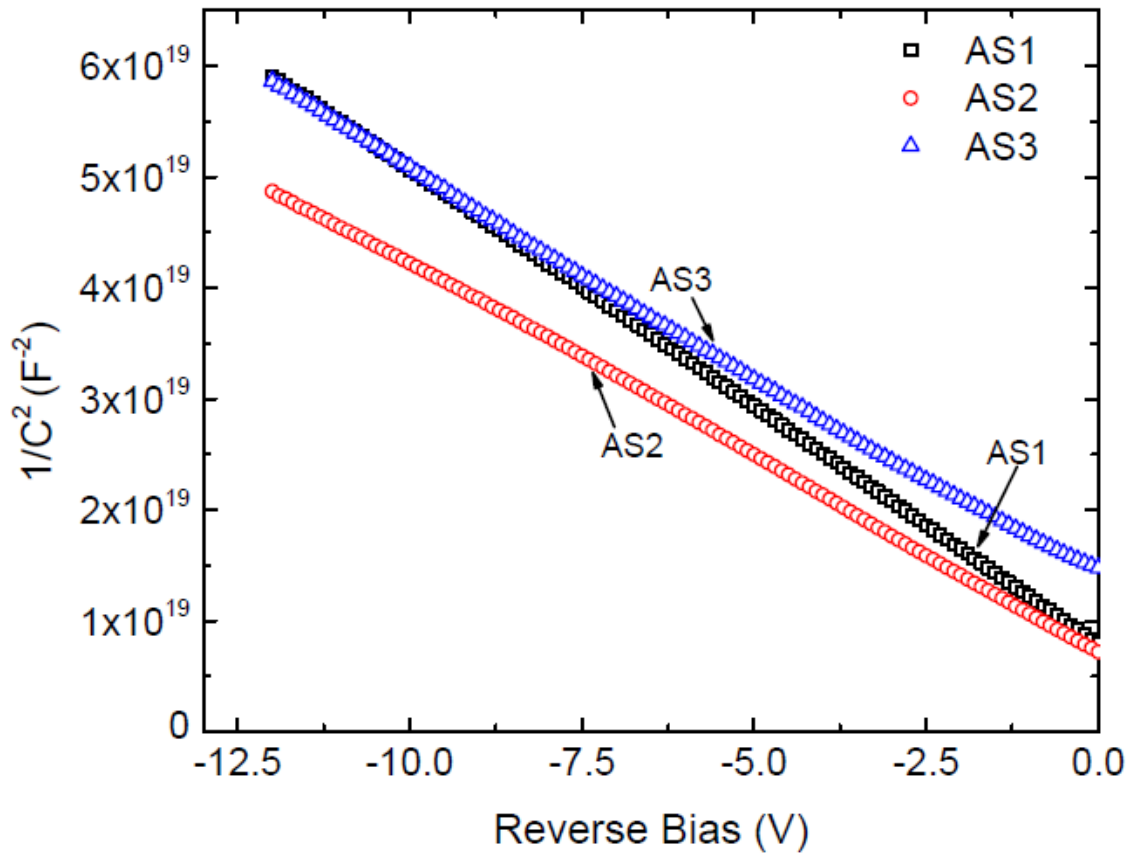


Figure 4.9. $1/C^2$ vs V plots for 4H-SiC epitaxial Schottky barrier radiation detectors AS1, AS2, and AS3.

4.3 RADIATION INTERACTION WITH SEMICONDUCTOR MATERIALS

Alpha particles continuously interact with the semiconductor material as they pass through by the Coulomb force with electrons in the material. If the transferred kinetic energy exceeds the electron's binding energy, ionization occurs which gives rise to the creation of an electron-hole pair. If a charged particle of mass m with kinetic energy E interacts with an electron of mass m_0 , the maximum transferable energy is $4Em_0/m$ in a single collision. Continuous interactions with various electrons in the absorber material

decrease the velocity of the charge particle until it captures electrons and becomes electrically neutral. Range in an absorber material is defined as the distance traversed by the charged particle in that particular material before it loses all its kinetic energy.

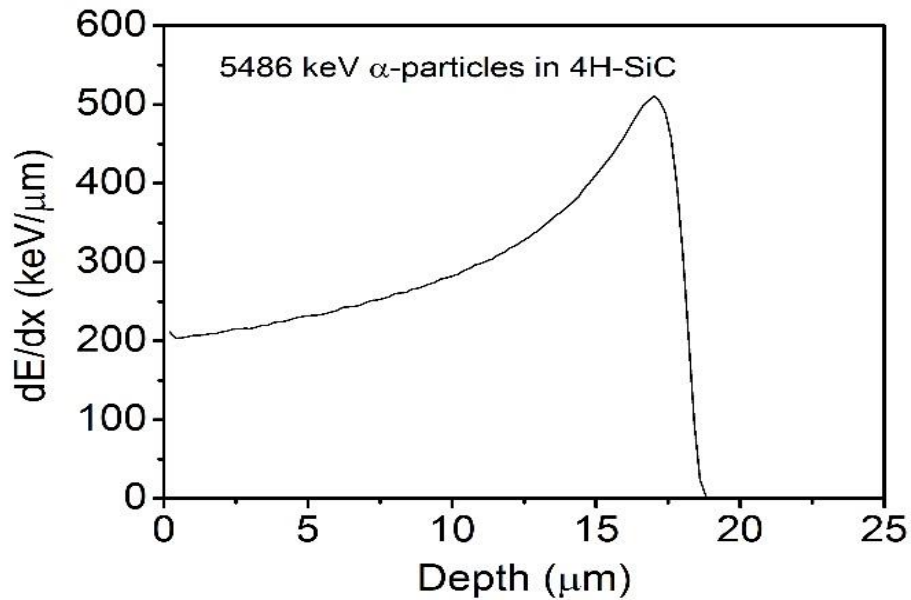


Figure 4.10. Energy loss of 5.48 MeV alpha particle as a function of penetration depth.

Figure 4.10 shows a Bragg curve which shows the energy loss of 5.48 MeV alpha particles as a function of depth of penetration. It can be seen from a Bragg curve that the maximum loss of energy for the alpha particles occurs at the end of the range which is typical of charged particle interaction with matter [78].

4.4 DRIFT-DIFFUSION MODEL

The drift-diffusion model proposed by Breese [79] allows the calculation of the minority carrier diffusion length for ion beam induced charge collection measurements.

For radiation detection applications, this model is used to calculate the separate contribution of charge carriers produced in the depletion region and that of the diffusion of holes created in the neutral region to the experimentally determined overall charge collection efficiency (CCE_{obs}). Equation 4.3 describes the concept applied to the model.

$$CCE_{theory} = \frac{1}{E_p} \int_0^d \left(\frac{dE}{dx}\right) dx + \frac{1}{E_p} \int_d^{x_r} \left[\left(\frac{dE}{dx}\right) \times \exp\left\{-\frac{x-d}{L_d}\right\}\right] dx \quad 4.3$$

$$= CCE_{drift} + CCE_{diffusion}$$

where E_p is the energy of the alpha particles, d is the depletion width at the particular bias, $\frac{dE}{dx}$ is the electronic stopping power of the alpha particles calculated using SRIM 2012 [80], x_r is the projected range of the alpha particles with energy E_p , and L_d is the diffusion length of the minority carriers. The first term of the Equation 4.10, CCE_{drift} , gives the contribution of charge generated within the depletion region to the charge collection efficiency and the second term, $CCE_{diffusion}$, is that from the charge carriers created in the region behind the depletion region and diffused to the depletion region.

4.5 RADIATION DETECTION

4.5.1 Pulse-height Spectrum

Once an alpha particle has deposited its energy into a detector which generates electron-hole pairs, the signal is extracted by the front-end electronics. Figure 4.11 shows

a typical radiation detection measurement setup which will process the signals produced by the detector into a useable form. The charge signal seen by the detector requires immediate amplification to prevent signal loss, due to the small amounts of charge involved. A preamplifier performs this initial amplification, which will allow the charge signal to be converted to a voltage signal, which can be sent over standard BNC cables to a shaping amplifier.

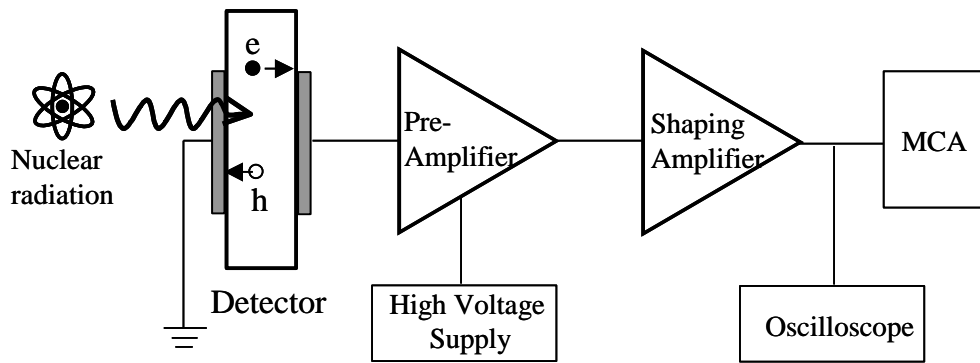


Figure 4.11. Schematic diagram of an analog radiation detection measurement system.

Preamplification is a critical step for signal processing in the detection system because noise introduced in this stage of the detection setup can have a significant effect on the resulting pulse-height spectrum. Figure 4.12 shows a basic charge-sensitive preamplifier circuit, and the effect the preamplifier has on the signal coming from the detector. A charge-sensitive preamplifier at its basic level consists of a high gain amplifier with a feedback capacitor and feedback resistor. The feedback capacitor makes the preamplifier insensitive to changes in the capacitance of the detector, while adding some noise to the circuit. Furthermore, a FET is usually used at the input of the high-gain amplifier, which must be carefully selected for noise consideration purposes.

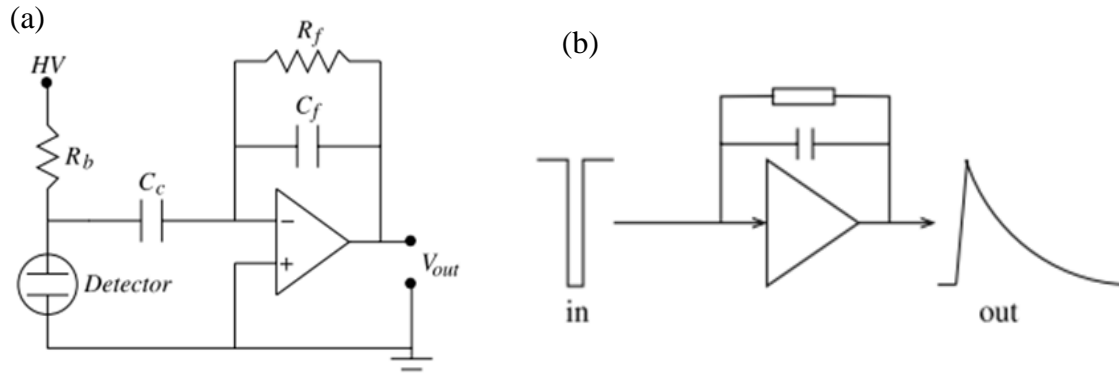


Figure 4.12. (a) Simplified circuit diagram for a charge sensitive preamplifier used in a detection system. (b) Input and output pulse shapes seen by a preamplifier [7]

After preamplification, the signal is sent to a shaping amplifier. The preamplifier pulse output contains background noise generated by both the preamplifier circuit and the detector itself. For this reason, these pulses are shaped by a shaping amplifier, which will filter as much noise as possible while preserving information about the energy of the radiation seen by the detector. This is done by passing the preamplifier signal through one stage of differentiation (using a CR, or high pass circuit) and several stages of integration (using an RC, or low pass circuit). Figure 4.13 shows the effect of a shaping amplifier on a preamplifier output signal as well as the analog circuitry and stages of CR and RC shaping used in a shaping amplifier. The shaping amplifier will spend a certain amount of time, τ_m , measuring the signal, which is also known as the shaping time.

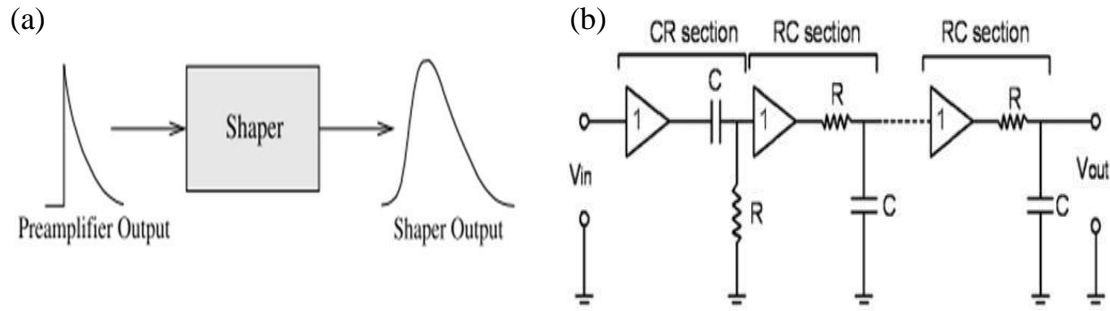


Figure 4.13. (a) Typical input and output pulse shapes seen by a shaping amplifier. (b) Simplified circuit diagram for the various stages of differentiation (CR) and integration (RC) used by an analog shaping amplifier [81].

After shaping, the amplified pulses are sent to a multi-channel analyzer (MCA). The MCA converts the analog signals into digital information containing the height of the shaped pulse (the “pulse-height”), and record the number of pulse-heights acquired within a given range. The resulting histogram, produced by the MCA is called the “Pulse-height Spectrum”, which depicts how many counts of particle interactions occur in the detector in a given energy window.

4.5.2 Experimental Setup for Spectroscopy Measurement

Pulse height spectra of alpha particles were collected using an analog spectrometer comprised of an Amptek CoolFet (A250CF) preamplifier, an Ortec 671 spectroscopy amplifier, and a Canberra Multiport II ADC-MCA unit controlled by Genie 2000 interface software. The radiation source used was a 0.1 μCi ^{241}Am alpha source (5.48 MeV is the main alpha peak energy) with an active diameter of 7 mm. To minimize

electromagnetic interference with the detector, the source and the detector under test were mounted inside an RFI/EMI shielded aluminum box.

During the measurements, the box was constantly evacuated ($\sim 10^{-3}$ mbar) using a rotary pump in order to minimize the scattering of alpha particles with air molecules. The radiation source was mounted inside the box just above the detector (facing the Schottky contact) at a vertical distance of 12 mm which ensures a full window illumination. Figure 4.14 shows a photograph of the 4H-SiC epitaxial Schottky barrier radiation detector inside the RFI/EMI shielded test box.

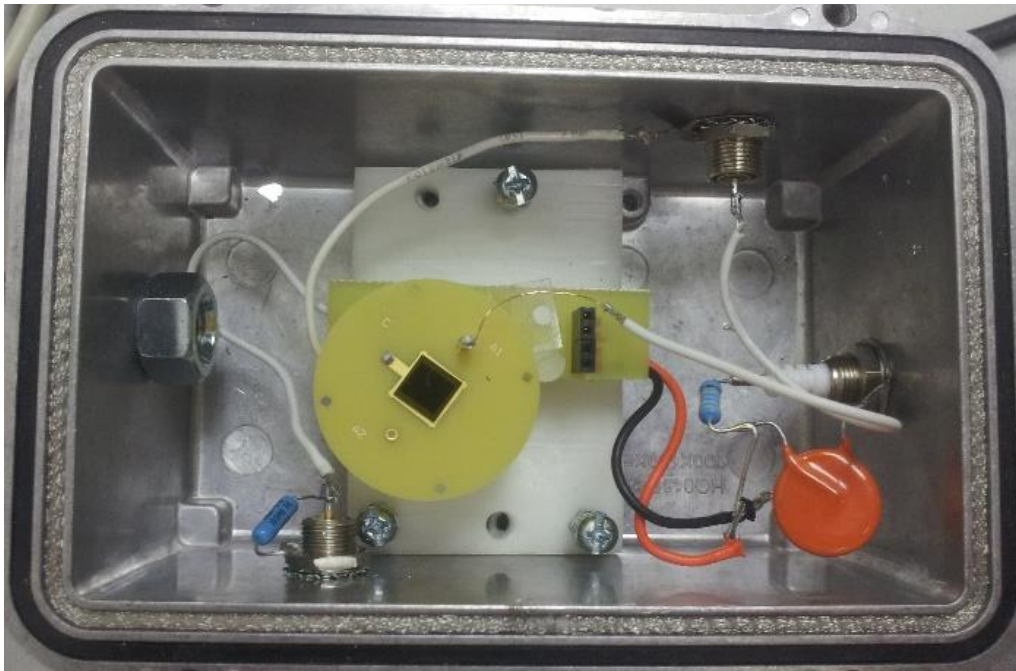


Figure 4.14. Photograph of the 4H-SiC epitaxial Schottky barrier radiation detector inside RFI/EMI shielded test box.

After placing the detectors and the sources in a proper configuration in the test box, the connections between the detector box, the pre-amplifier (A250CF), the NIM bin, the oscilloscope, and the computer were made as shown in Figure 4.15.

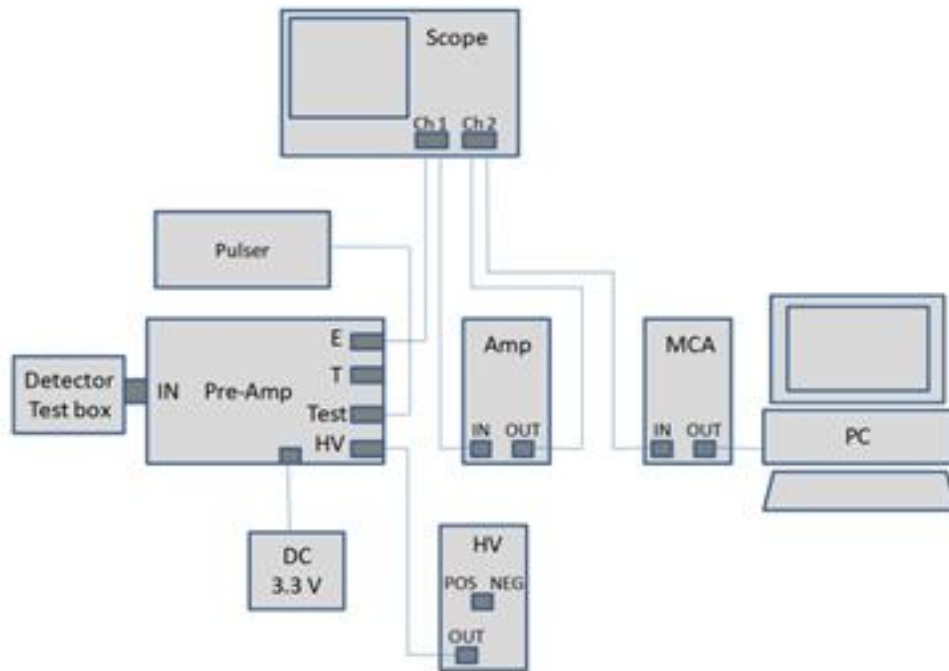


Figure 4.15. Connection schematic for analog data acquisition set-up.

The charges generated in the detector due to the incident radiation energy are collected by the A250CF, which is a charge sensitive low noise pre-amplifier and is best suited for room-temperature detector operation. It hosts a Peltier cooled FET which helps with noise reduction to a great extent. The voltage output of the pre-amp is then fed to the shaping amplifier (Ortec 671) which produces a shaped (semi-Gaussian) amplified output with enhanced signal-to-noise ratio. This is achieved by using a band pass filter consisting of differentiator and integrator circuits. The amplifier allows the user to select the shaping time constant for optimized (trade-off between minimum noise and complete

charge collection time) detector performance. This amplified voltage output is directly proportional to the incident energy of the radiation.

The amplified output pulse is then fed to a multichannel analyzer (MCA), which basically digitizes the amplifier output pulse signal, and bins the pulses of similar heights in similar bins or channels to obtain a histogram of the distribution of pulse-height. A higher channel number corresponds to a higher energy level. The resulting distribution is called a pulse-height spectrum or simply energy spectrum. Once a pulse-height spectrum is generated, the full width at half maxima (FWHM) of the alpha energy peak is calculated through the Gaussian peak fitting function using the Origin plotting software. The energy resolution of the detector is calculated by the following Equation 4.4:

$$\% \text{ Energy Resolution} = \frac{FWHM (keV)}{Centroid (keV)} * 100\% \quad 4.4$$

where the centroid is the “center of mass” of the energy peak observed in the pulse-height spectrum. Lower values of energy resolution and FWHM indicate better detector performance. The software Genie 2000 was used to acquire and save pulse-height spectra and also to analyze the acquired data.

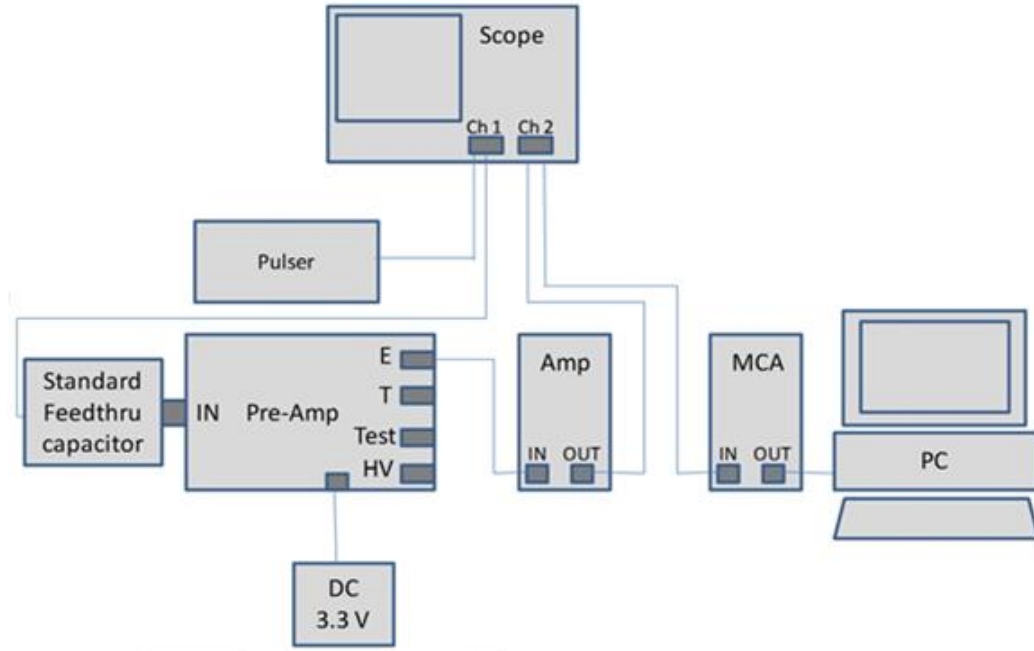


Figure 4.16. Schematic of the electrical connections for energy calibration.

Once the data is acquired, a calibration process is performed in order to find a correlation between the channels of the MCA with their corresponding energy. It is important to note that the calibration process should be done under the same settings and similar configuration as the setup used to test a radiation detector. In order to calibrate the system, a pulser, which generates waveforms and simulates the output of a radiation detector, is connected to the detection system through a capacitor. Figure 4.16 shows the connection schematic for energy calibration. The energy of the charge pulses from the capacitor, E_{pulser} (in keV) can be determined using the Equation 4.5.

$$E_{pulser} = \frac{V_{pulser} \times \varepsilon \times C}{1.6 \times 10^{-19}} \quad 4.5$$

where ϵ is the electron-hole pair creation energy (7.7 eV for 4H-SiC) [82]. This calibration was accomplished by the injecting pulses of various known amplitudes, V_{pulsar} (mV), from a precision pulser (Ortec 419) through a calibrated feed-through capacitor, to the preamplifier input and simultaneously noting down the peak positions of the shaped pulses in the MCA.

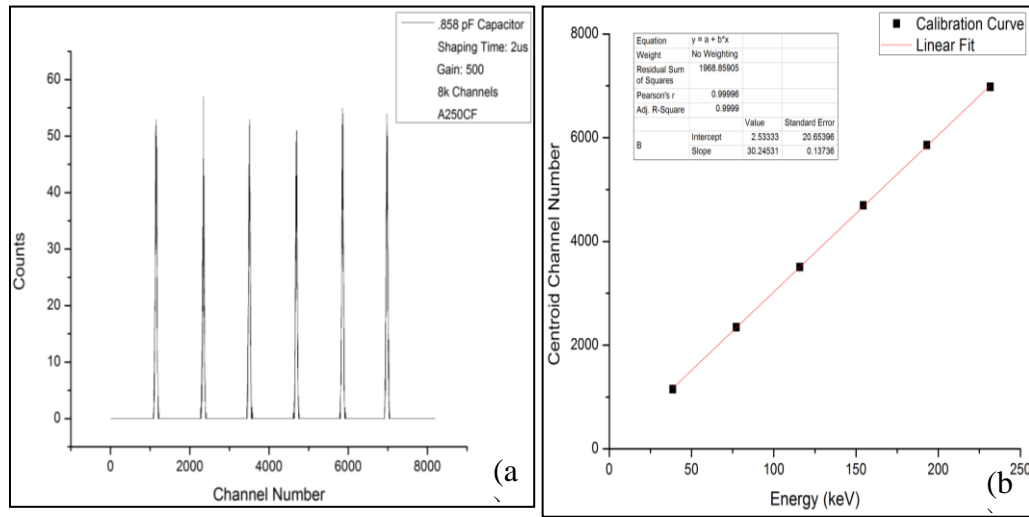


Figure 4.17. (a) Pulse-height spectrum obtained for six different pulse sizes, and (b) Corresponding calibration curve.

The pulse-height is systematically changed via the pulser to generate several peak positions relative to the pulser energies. A graphical plot between E_{pulsar} and corresponding MCA peak positions for different pulse-heights, gives the calibration graph. Figure 4.17 shows one MCA spectrum with various pulser peak-positions taken during calibration. The linear plot of the peak centroid channel number against the keV equivalent pulser energy as shown in Figure 4.0 b gives the required calibration parameters [83]. Using the Equation 4.5, values obtained in terms of MCA channel

numbers are converted to energy units in keV. The entire radiation detection setup in our laboratory at USC is shown in the Figure 4.18.

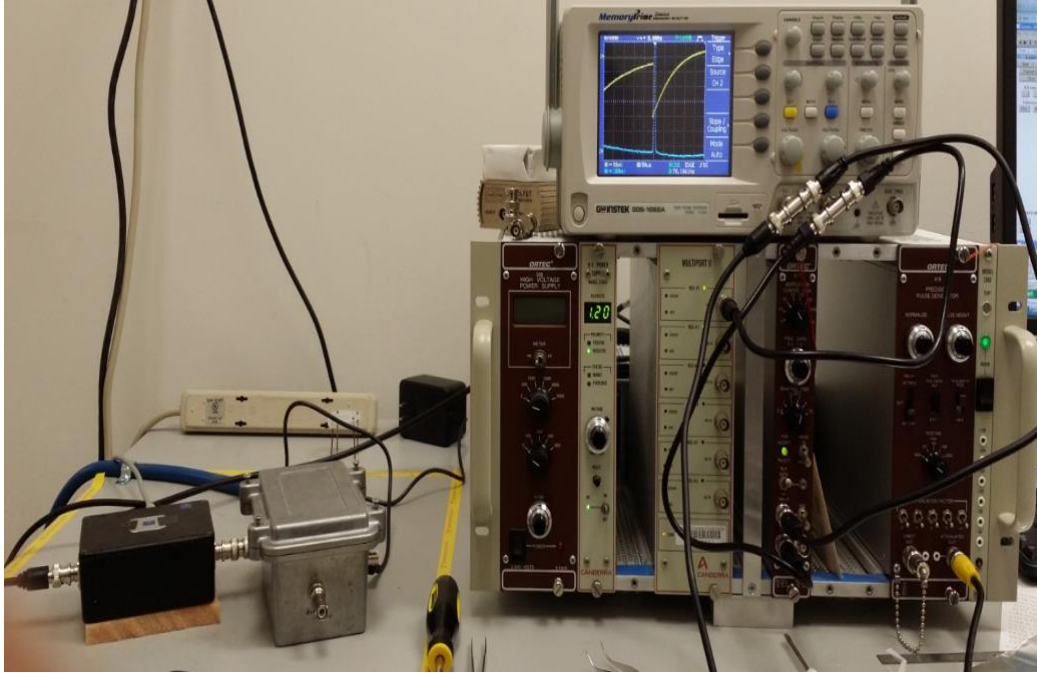


Figure 4.18. Picture of the radiation detection system at USC.

4.6 ALPHA SPECTROSCOPY MEASUREMENT RESULTS

The information obtained by the electrical characterization of the fabricated detectors is useful deciding which detectors are suitable for spectroscopic characterization. Spectroscopic characterization was performed using the detector AD06 and a 0.1 μCi ^{241}Am alpha source. The spectrometer was set up following the description in Section 4.5.

Figure 4.19 shows the variation of charge collection efficiency (CCE_{obs}) for alpha particles calculated from detector AD06 as a function of reverse bias [75]. The CCE_{obs} was calculated as the ratio of the output energy observed by the detector to the actual incident energy of the alpha particles (5.48 MeV). The contribution of the drift ($CCE_{depletion}$) and diffusion ($CCE_{diffusion}$) related charge collection to the observed total charge collection efficiency was calculated using the drift-diffusion model described in section 4.3.

The detector readily showed an alpha peak with charge collection efficiency (CCE) of ~17% at 0 V applied bias when exposed to a ^{241}Am source, suggesting a substantial diffusion of minority carriers. As can be seen from Figure 4.19, the charge collection efficiency was observed to improve with increase in reverse bias.

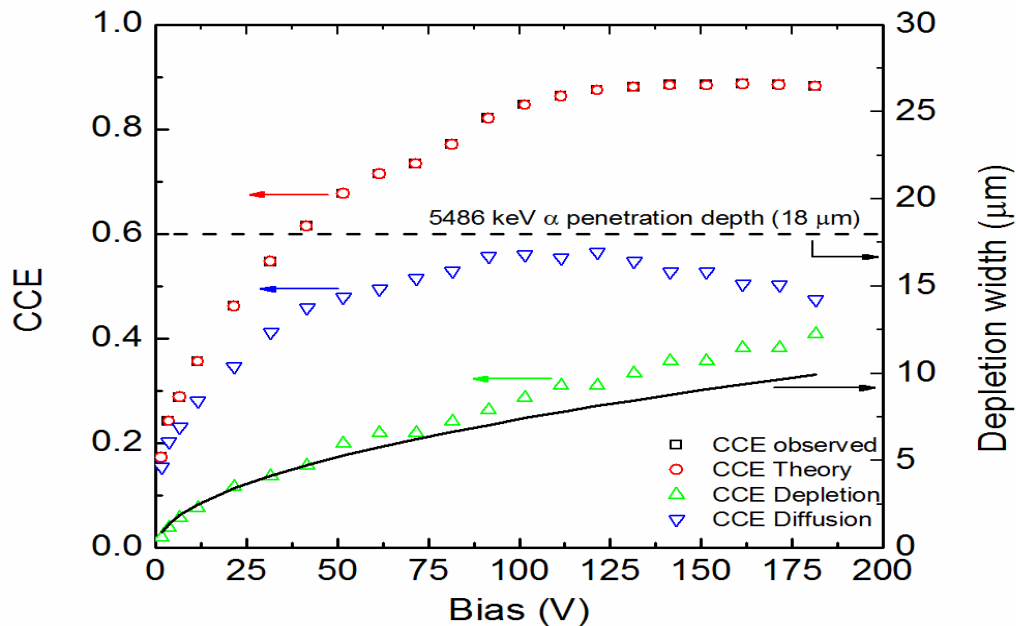


Figure 4.19. Variation of experimentally obtained (□) and theoretically calculated (○) CCE. CCE from drifts (Δ) and diffusion (▽) are also shown. The solid line shows the variation in depletion width.

From Figure 4.19 it could be seen that the experimentally observed CCE values reached a maximum value of ~ 0.87 at an applied bias of 130 V and started to decrease slowly thereafter. A CCE value less than 1 suggests that a fraction of the generated charge carriers are getting trapped and eventually lost (recombine) in the defect centers. It can also be noticed from Figure 4.19 that the major contribution towards the observed CCE was from the diffusion of the charge carriers (more than 50%). The contribution of the drifting of charge carriers ($CCE_{depletion}$) towards $CCE_{observed}$ was seen to increase steadily with the reverse bias and became almost equal to $CCE_{diffusion}$ at higher reverse bias voltages. The reason behind the dominating contribution of charge carrier diffusion towards $CCE_{observed}$ is because of the fact that the depletion width ($\sim 10 \mu\text{m}$) at the highest applied bias of -180 V was still much less compared to the penetration depth of the 5486 keV alpha particles ($\sim 18 \mu\text{m}$) in 4H-SiC. Hence, a substantial part of the charge carrier generation takes place in the neutral region of the detector. However, for superior detector performance, the generation of charge carriers is preferred to occur in the depletion region in order to obtain optimized charge transport properties. The reverse bias was further increased to widen the depletion width so that the contribution of charge carrier drifting in the detector could increase CCE. However, further increase in bias voltage led to increased leakage currents which deteriorated the detector performance.

The depletion width (d) of a Schottky junction of a given material and bias depends on the effective doping concentration of the semiconductor material as shown in Equation. 4.6. Electrically active defects can behave as acceptor or donor levels thus controlling the effective doping concentration and hence the depletion width.

$$d = \sqrt{\frac{2\varepsilon\varepsilon_r(\Phi_B - V)}{qN_{eff}}} \quad 4.6$$

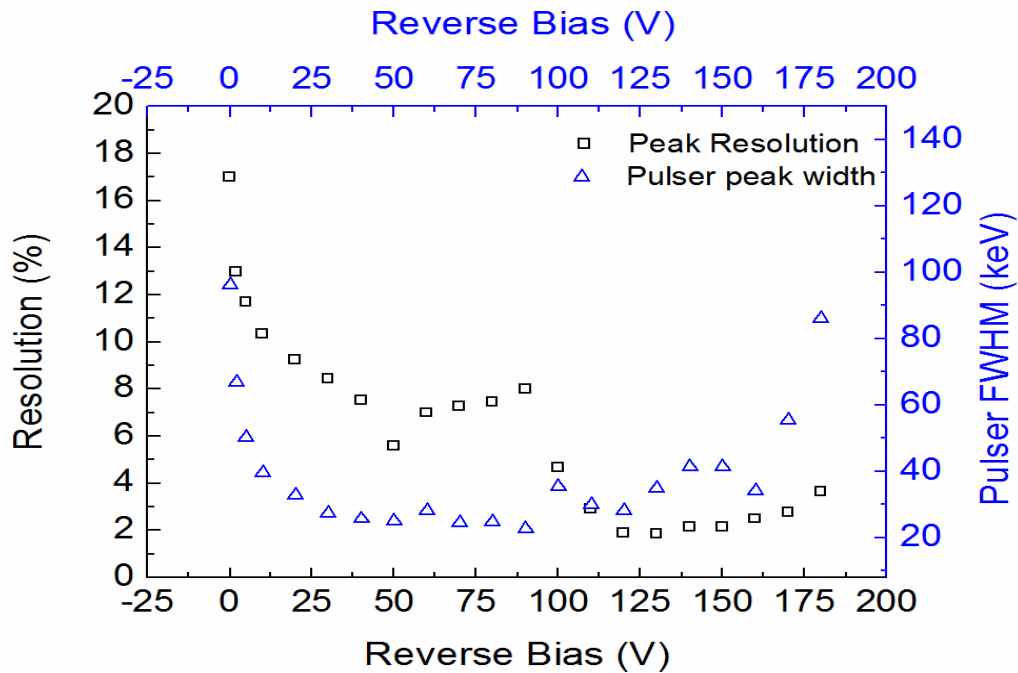


Figure 4.20. Variation of detector energy resolution as a function of reverse bias voltage. The variation of the peak width (FWHM) of the pulser recorded simultaneously has also been plotted.

The dependence of detector energy resolution with the reverse bias is shown in Figure 4.20 [75]. The percentage energy resolution improved with the reverse bias because of improved charge collection and lowering of detector capacitance (reduction of series noise). However, the resolution was seen to deteriorate with further increase in reverse bias due to increase in leakage current as was evident from the increase in the corresponding pulser peak width (FWHM) shown along-with in Figure 4.20. Also, increase in the depletion width leads to inclusion of more number of defects within the

detector active volume leading to poor performance of the detectors. Figure 4.21 shows the best pulse-height spectrum obtained with the optimized bias settings. The energy resolution of 1.8% is observed for the 5486 keV alpha peak [75].

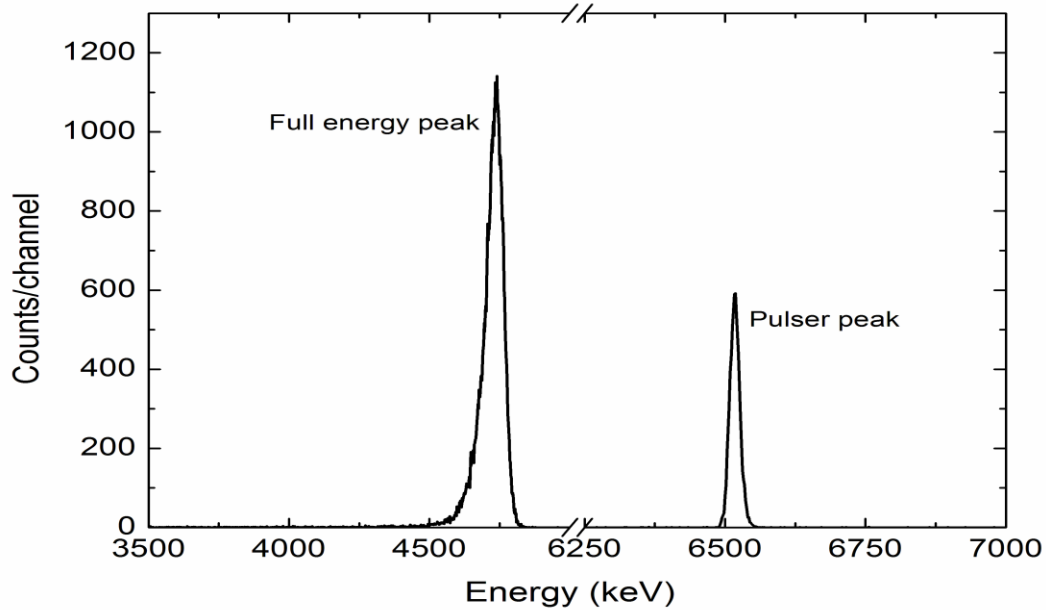


Figure 4.21. An ^{241}Am pulse-height spectrum obtained using the $50\ \mu\text{m}$ n-type Ni/4H-SiC epitaxial Schottky barrier detector reverse biased at 130 V.

The pulse-height spectra for ^{241}Am obtained from detectors AS1, AS2, and AS3 are shown in Figure 4.22 (a), (b), and (c), respectively [2]. The percentage energy resolutions of the detectors AS1, AS2, and AS3 were calculated as 0.29% , 0.38% and 0.96%, respectively. Detector AS1 exhibited the highest energy resolution (0.29%) among the three detectors, and it could be seen from Figure (a) that the three major alpha particle energies, viz. 5388 keV, 5443 keV, and 5486 keV emitted from an ^{241}Am source were clearly resolved. Detector AS2 showed a moderately high energy resolution of 0.38%, and AS3 showed a comparatively lower resolution but still less than 1% for 5486 keV alpha particles.

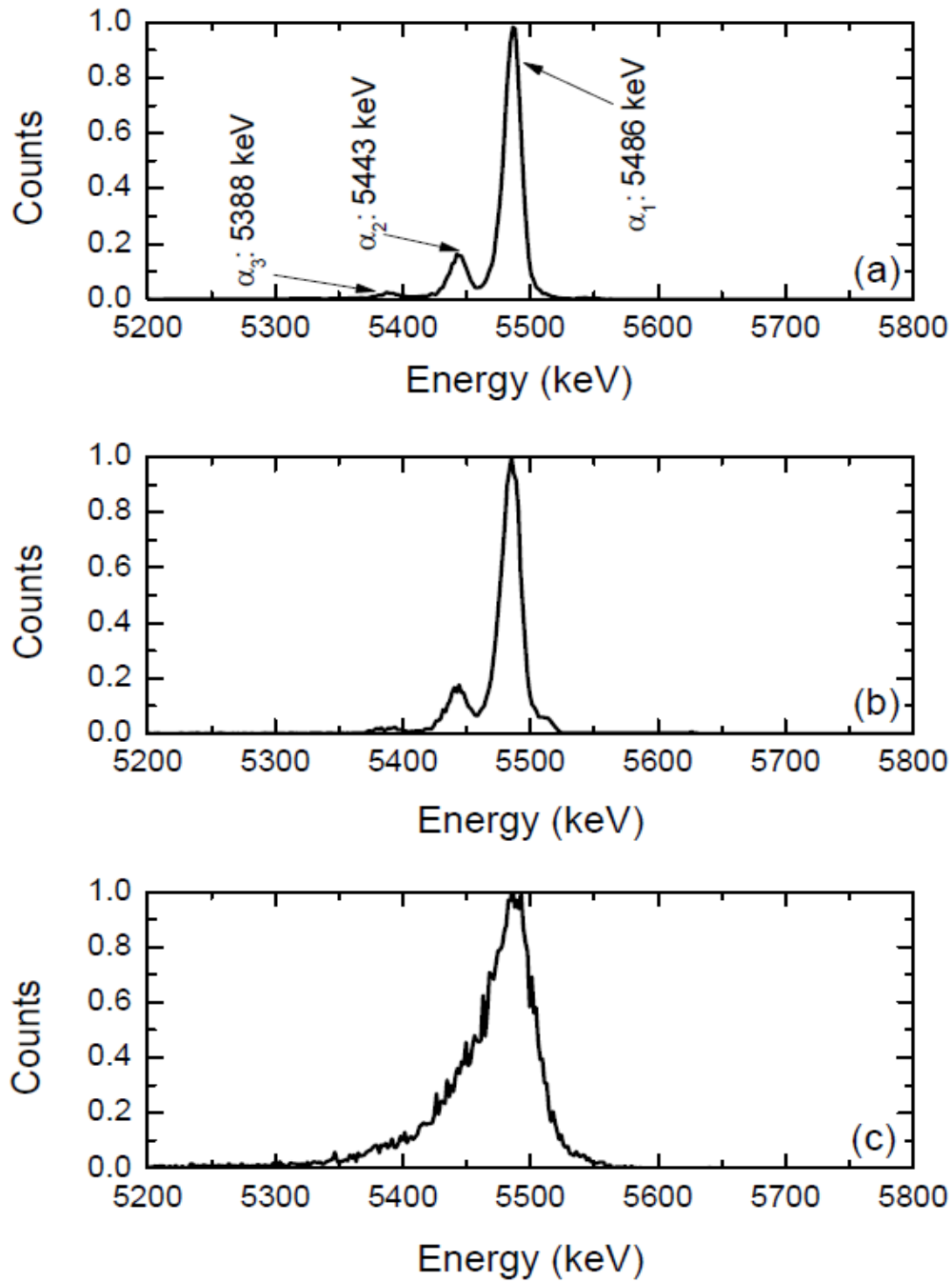


Figure 4.22. Alpha pulse-height spectra obtained for detectors (a) AS1, (b) AS2, and (c) AS3 using an ^{241}Am source.

4.7 CONCLUSION

Electrical and spectroscopic characterizations were performed on 4H-SiC detectors fabricated on 20 μm and 50 μm n-type 4H-SiC epilayers. I-V characteristics revealed the Schottky behavior of the detectors. Using a thermionic emission model, the barrier height and diode ideality factor were calculated for all fabricated detectors. The doping concentration (N_{eff}) was calculated from the C-V measurements. Due to good Schottky behavior and low leakage current at high reverse bias voltage (>100 V) the fabricated detectors were found to be suitable for radiation detection. Spectroscopic characterization was performed on the detectors with ^{241}Am alpha source. The percentage energy resolution of the detectors was found in the range 0.29% - 1.8% for 5486 keV alpha particle peak.

CHAPTER 5: DEFECT CHARACTERIZATION BY DLTS STUDIES

5.1 INTRODUCTION

In a semiconductor material, defect centers could either act as an electron trap or a hole trap. These trap levels are associated with four fundamental phenomena that may occur as illustrated in Figure 5.1. Electrons could be trapped by a defect level acting as an electron trap. This process is known as electron capture. Consequently, a trapped electron may get de-trapped if sufficient thermal energy is available. This process is known as electron emission. Similarly, a hole capture process is characterized by trapping of a hole by a defect level and the hole emission process by de-trapping of a previously captured hole.

The semiconductors properties may be greatly influenced due to this charge carrier capture/emission phenomena by the defects and hence affect the efficiency of the electronic devices. Therefore, it is very important to identify and characterize the defects to understand their role in electronic and opto-electronic device performance. The characterization would provide a deep understanding of defects in the semiconductor which will be very helpful to enhance the efficiency of devices.

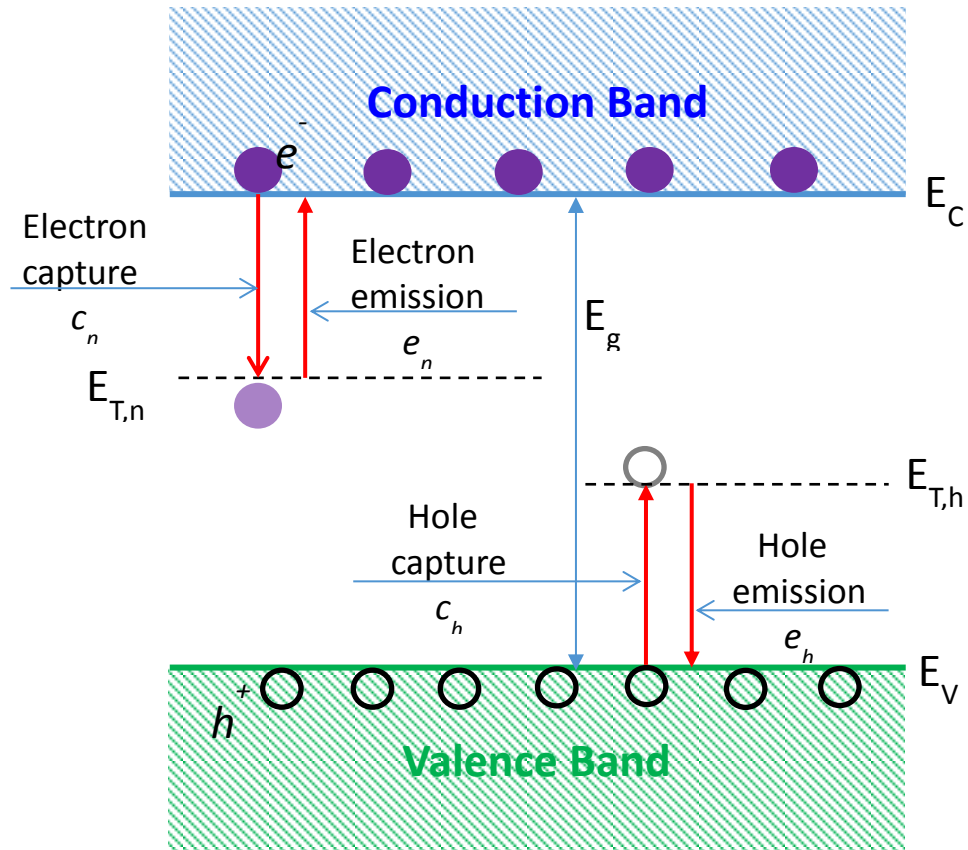


Figure 5.1. Illustration of electron and hole trapping and de-trapping phenomena in a semiconductor material.

Different techniques have been used to characterize the defects in semiconductor, some of which include: admittance spectroscopy (AS), positron annihilation spectroscopy (PAS), thermally stimulated current (TSC), Rutherford backscattering spectroscopy (RBS), optically stimulated conductivity (OSC), thermally stimulated capacitance (TSCAP), and deep level transient spectroscopy (DLTS). In this chapter, the theoretical background and experimental methods of defect characterization by TSC and DLTS are discussed in detail.

5.2 DEFECT PARAMETERS

During defect characterization, by any method, it is essential to measure some of the important parameters of the defects. The main parameters required for characterization of deep levels are: (a) Activation energy, (b) Capture cross-sections, (c) Concentration of deep levels.

5.2.1 Energy Level

The activation energy ΔE gives the exact position of a deep level in the band-gap. The activation energy of defects is defined as the required energy needed to move an electron from the trap center into the appropriate energy band. The activation energy of a defect depends upon the location of the trap center in the band-gap and varies from defect to defect. The energy of the conduction band E_c or energy of the valence band E_v is usually taken as reference during the measurement of the activation energy. A trap with the energy E_T in the band-gap requires the activation energy $(E_c - E_T)$ for electron emission and $(E_v + E_T)$ for hole emission.

5.2.2 Trap Concentration

Trap concentration is one of the most important parameters for defect characterization. Defect properties and their influence on semiconductor behavior greatly depend on their concentration. This parameter helps to determine the extent of the role

defects have on device performance. The trap concentration is defined as the amount of a particular deep level in the band-gap of the semiconductor material. The number of deep level traps in the band-gap of the semiconductor material is denoted as the concentration of deep levels.

5.2.3 Capture Cross-section

Deep levels may act as a trapping, recombination, or generation centers in the semiconductors. Each of these behaviors highly depend upon the electron and hole capture rates of the trap. The capture rate of a trap is determined by the characteristics of the capture cross-section for that particular trap.

5.3 DEFECT CHARACTERIZATION BY THERMALLY STIMULATED CURRENT

5.3.1 Background and Experiment

Thermally stimulated current (TSC) is widely used to study deep energy levels in semiconductor materials [49]. In TSC measurement, the semiconductor is cooled to a low temperature, and the trap centers are filled using light of a wavelength greater than or equal to the band-gap of the material. The electrons/holes are emitted from the filled traps by slowly heating the sample at a constant rate. Under an applied bias, the emitted electrons and holes will produce current which is measured by an ammeter and a PC. The emission is thermally activated and has an emission rate e_n [84] given by

$$e_n = \sigma N_c V_{th} * \exp(-E_T/kT) \quad 5.1$$

where σ is the capture cross-section for the trap, N_c is the effective density of states, V_{th} is the thermal velocity, and E_T is the trap energy with respect to the conduction band. According to the equation, a given trap will begin emission at a characteristic temperature. As temperature increases, emission rate will rapidly increase. The emission probability will drop when the trap is depleted, and the emitted current will reach a peak. TSC spectrum signal is obtained by plotting the emitted current against temperature which is used to determine the deep level signature.

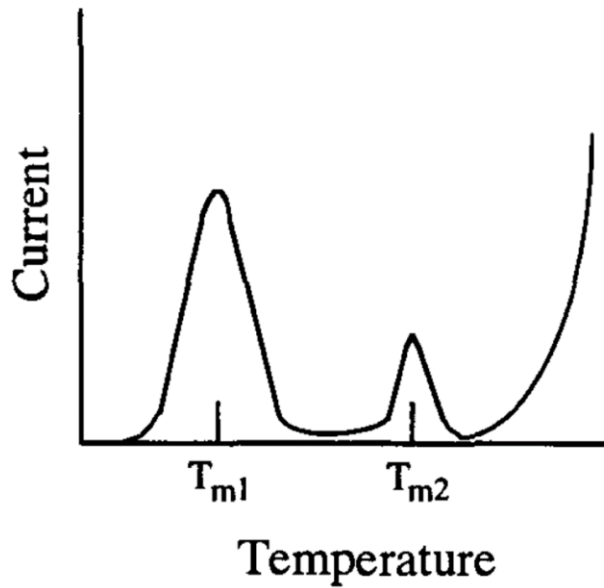


Figure 5.2. TSC spectrum showing trap centers at temperatures T_{m1} and T_{m2} . [85].

Figure 5.2 shows a TSC spectrum with two peaks at temperature T_{m1} and T_{m2} . The peaks appeared in the spectrum of thermally stimulated current due to the release of

charge carriers from two different trap centers in the band-gap [49]. The thermally stimulated current can be described by the following equation [84, 85]

$$I_{TSC} = CV_b q \mu \tau N_T e_n * \exp\left(-\int \frac{e}{\beta dT}\right) \quad 5.2$$

where q is electronic charge, μ is the carrier mobility, τ is the carrier lifetime, N_T is the trap density, V_b is the bias voltage, e_n is the emission rate of trapped carriers, β is the heat rate, and C is the constant related to the sample geometry.

The magnitude of a peak corresponding to a trap center in a given spectrum will vary with the heating rate. An Arrhenius plot can be drawn from the peaks of different heating rate spectrum, and all of these peaks are associated with a particular trap. The trap center activation energy associated with peaks at T_m can be calculated from the slope of an Arrhenius plot using equation [84, 85, 86],

$$\frac{E_T}{kT} = \ln\left(\frac{T_m^4}{\beta}\right) + \ln\left(\frac{10^{17} * \sigma}{E_T}\right) \quad 5.3$$

where E_T is the activation energy of the trap level, β is the heating rate, σ is the capture cross-section, and k is the Boltzmann's constant.

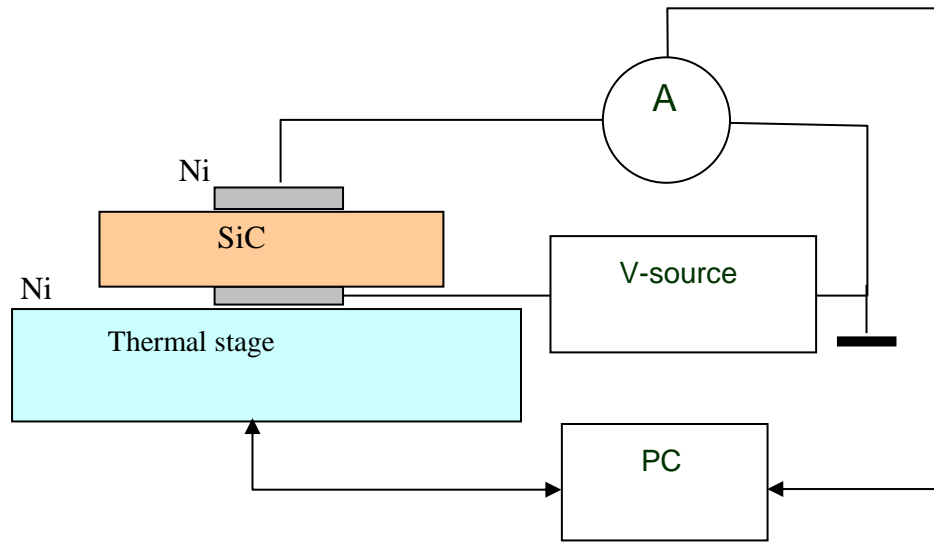


Figure 5.3. Schematic of the TSC experimental setup

The TSC measurements on the epitaxial layers were conducted in the temperature range 94 K - 620 K in vacuum of about 2×10^{-5} Torr. Figure 5.3 shows the schematic of the experiment setup for TSC measurement. The setup is equipped with a Keithley 6517A Electrometer/High resistance meter, thermal stage with programmable temperature controller (MMR Technologies), and low temperature microprobe (LTMP) chamber. At 94 K, the traps are filled by illumination using an UV lamp (320 nm , 1.5 mW/cm^2) [86].

5.3.2 TSC Spectroscopy and Defect Identity

For TSC measurement the $8 \text{ mm} \times 8 \text{ mm}$ samples were taken from a $\sim 390 \text{ }\mu\text{m}$ thick 4H-SiC (0001) semi-insulating wafer with a resistivity $\geq 1012 \text{ }\Omega\text{-cm}$. After standard RCA cleaning, Ni contacts on both Si and C side were deposited by electron beam deposition. The contacts were annealed at 1273 K for 1 minute in nitrogen ambient using

a Jipelec JetFirst Rapid Thermal Processor [86]. Figure 5.4a shows the TSC spectra for three different heat rates at 5, 10, and 15 K/min and Figure 5.4 b shows the corresponding Arrhenius plot to calculate activation energy [86, 87]. Five distinct peaks are identified in this spectrum. The capture cross-section of the TSC peaks 1, 2, and 5 are estimated by fitting the spectrum with the equation (ITSC) [88]. The observed maximum temperature T_m and the calculated parameters of the traps are summarized in Table 5.1.

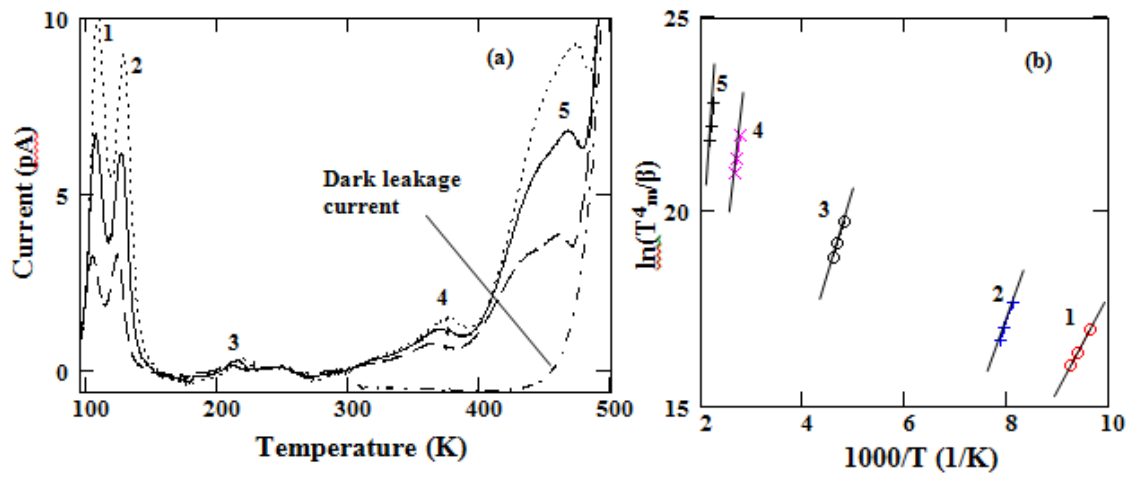


Figure 5.4. TSC spectra for the heat rates of 5 K/min (----), 10 K/min (—), and 15 K/min (····) at 10 V bias voltage. (b): Arrhenius plot of $\ln(T_m^4/\beta)$ versus $1000/T$ for five traps corresponding to peak numbers 1 – 5 in Figure (a)

Table 5.1. Trap parameters deduced from TSC measurements [86]

TSC peak #	T_m @ 10 K/min (K)	Trap activation energy (eV)	Capture cross-section (cm^2)	Possible Defect or Impurity
1	106.5	0.23	$\sim 10^{-17}$	Al
2	126	0.32	$\sim 10^{-15}$	B, Ga
3	215	0.42		EH1
4	370	0.95		V
5	456	1.1-1.2	$\sim 10^{-16}$	Unnamed

The intrinsic defects of 4H-SiC, which are responsible for the TSC peaks, are identified by using literature data. Maximum temperature and activation energy of the peaks in the TSC spectrum are compared with those of published literature to identify the impurity causing the defects. The peak 1 maximum temperature and activation energy is similar to that found by Fang et al. [84], and they assigned the peak to aluminum related shallow hole trap. Lebedev et al. [89] showed that boron or gallium related shallow hole trap and EH1 electron trap are responsible for the peaks 2 and 3 of the spectrum. The peak 4 is identified as electron trap related to vanadium acceptor level [84]. The activation energy of peak 5 of the spectrum is found in the range of 1.1 eV - 1.2 eV. Deep levels with this activation energy were found for bulk semi-insulating SiC [90, 91]. However, the origin of the defect is unknown, and no name is assigned to it.

In another experiment, TSC measurement was carried out on n-type 4H-SiC epitaxial layers grown by chemical vapor deposition (CVD). Figure 5.5 shows the TSC spectrum of the samples obtained with 15 K/min heat rate at 10 V reverse bias [92]. All the parameters extracted from the TSC measurement are provided in Table 5.2.

The peak #1 of the spectrum is due to B/Al complexes which form shallow acceptor-like levels near the valence band edge [93]. The peak #2 appeared at $T_m \sim 175$ K in the spectrum. This peak is due to hole traps in the lower half of the band-gap and identified as HS1 [94] and HH1 [95]. Peak #3 observed at ~ 225 K in the spectrum and is associated with boron related D-center [84, 89, 96]. Peak #4 ($T_m \sim 280$ K) is attributed to $Z_{1/2}$ which is an electron trap associated with a vacancy related defect [89, 94]. Broad

peak #5 (350 – 400 K) can be associated with IL2 [97], SI-6 [98], and SI-8 [98] intrinsic defects. However, a V-related trap center was also identified as the origin of peak #5 [84, 86].

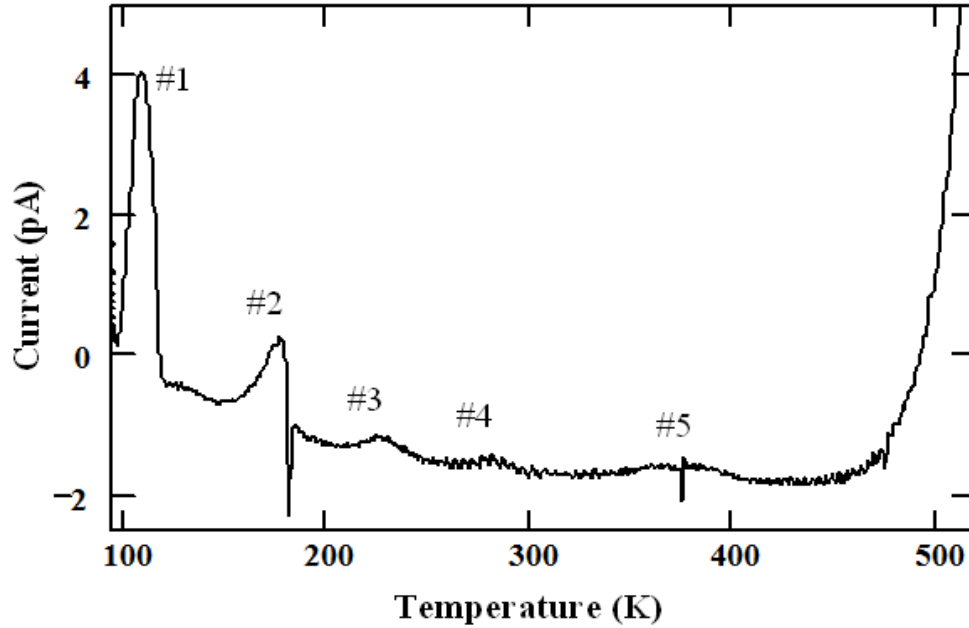


Figure 5.5. TSC spectrum of n-type 4H-SiC epitaxial layer obtained at 10 V reverse bias and 15 K/min heat rate [92].

Table 5.2. Trap parameters by TSC measurements for the 4H-SiC n-type epilayer [92]

Sample	TSC Peak #	Trap activation energy (eV)	Capture cross-section (cm ²)	Possible Defects or Impurities
4H-SiC n-type epilayer	1	0.22	~10 ⁻¹⁶	Al/B complexes, shallow
	2	0.25	~10 ⁻¹⁵	HS1-HH1 Hole traps
	3	0.31	~10 ⁻¹⁶	Boron D center
	4	0.95		Z _{1/2} electron center
	5	-		IL2, SI-6, SI-8 and/or to V

5.4 THEORETICAL BACKGROUND OF DLTS MEASUREMENT

5.4.1 Introduction

Deep levels influence both the electrical and the optical properties of material which can severely affect the device performance. It is very essential to develop sensitive equipment for deep level characterization semiconductor material. The equipment should be able to determine all important parameters (energy level, concentration, and capture cross-section) of the defects. It is also preferable that the equipment can distinguish between majority and minority carrier traps. Deep level spectroscopy (DLTS) is one of the most versatile techniques to determine the abovementioned electrical properties of electrically active defects over a wide range of depths in semiconductor material.

DLTS investigates electrically active defects in a depletion region of Schottky diodes or p-n junctions. In the DLTS measurement process, the depletion region is kept in reverse bias condition with a steady-state voltage. The depletion region reduction by a voltage pulse allows the flow of charge carriers (electron/holes) from the bulk region to the depletion region which fills the defect centers. When the pulse is removed, the defects start to emit trapped carriers due to thermal emission which causes transients in the depletion region capacitance. Important defect parameters can be determined by analyzing these capacitance transients. The DLTS, which is the most sensitive defect characterization technique, was first introduced by D. V. Lang (David Vern Lang of Bell Laboratories) in 1974 [14].

5.4.2 DLTS Technique

The DLTS measures the change of junction capacitance of the sample due to the emission of charge carriers from the defects existing in the space charge region. To better understand the DLTS theory, let us consider a reverse biased *n*-type semiconductor Schottky device as shown in Figure 5.6 A. The depletion region capacitance of a Schottky device having a homogeneous doping concentration can be expressed as

$$C_0 = A \sqrt{\frac{\epsilon\epsilon_0 eN_D}{2(V_r + V_d)}} \quad 5.4$$

where *A* is the sample area, N_D is the charge density in the space charge region, V_r is the reverse bias, V_d is the built-in voltage, ϵ is the permittivity of the semiconductor material, and *e* is the electron charge.

The semiconductor has a deep level trap with energy E_T , and all the traps in the space charge region are empty whereas all the traps in the bulk semiconductor are filled. An applied pulse (Figure 5.6 B) reduces the space charge width and increases the capacitance drastically. Now the traps are filled with the injected carriers from the bulk region. With return of the reverse bias to its quiescent level, the width of the space charge region increases again (Figure 5.6 C). However, charge density in the space charge region is slightly less than it was before applying the pulse. Therefore, the width of the space charge region, in the case of Figure 5.6 C, is slightly higher than that of Figure 5.6 A. Obviously; the capacitance is slightly lower for the case C.

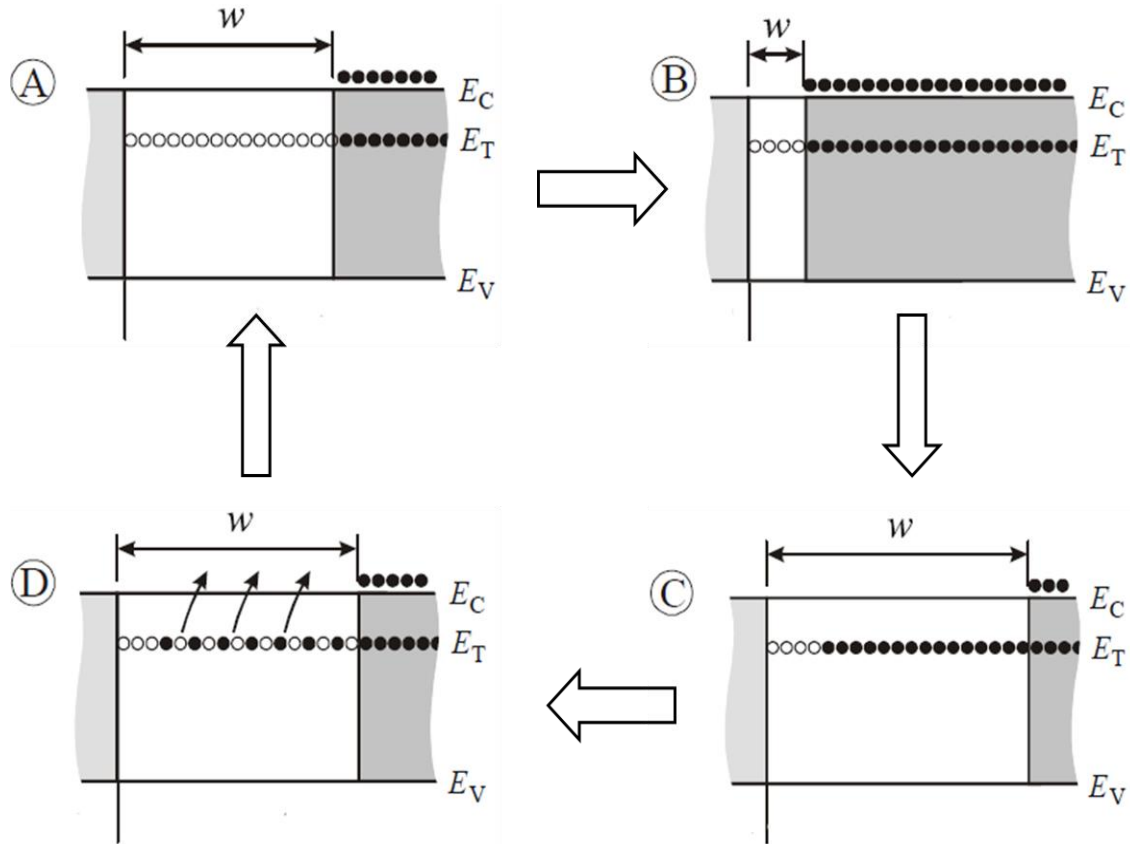


Figure 5.6. A schematic of the DLTS transient signal generation. (A): Steady state reverse bias, (B): Applying pulse; (C) Just after removing pulse; (D) Capacitance transient due to thermal emission of carriers.

As the filled traps are above the Fermi level, the system will relax into thermal equilibrium by emitting trapped charge carriers (Figure 5.6 D), and the capacitance will gradually increase until the steady-state value of Figure 5.6 A. The thermally activated emission rate e_n can be expressed as

$$e_n = (\sigma_n \langle V_{th} \rangle N_C / g) \exp(-\Delta E / kT) \quad 5.5$$

where σ_n is the carrier capture cross-section, $\langle V_{th} \rangle$ is the mean thermal velocity, N_C is the effective density of states, g is the degeneracy of the trap level and was considered to be equal to 1 in the present calculations, and ΔE is the energy separation between the trap level and the carrier band.

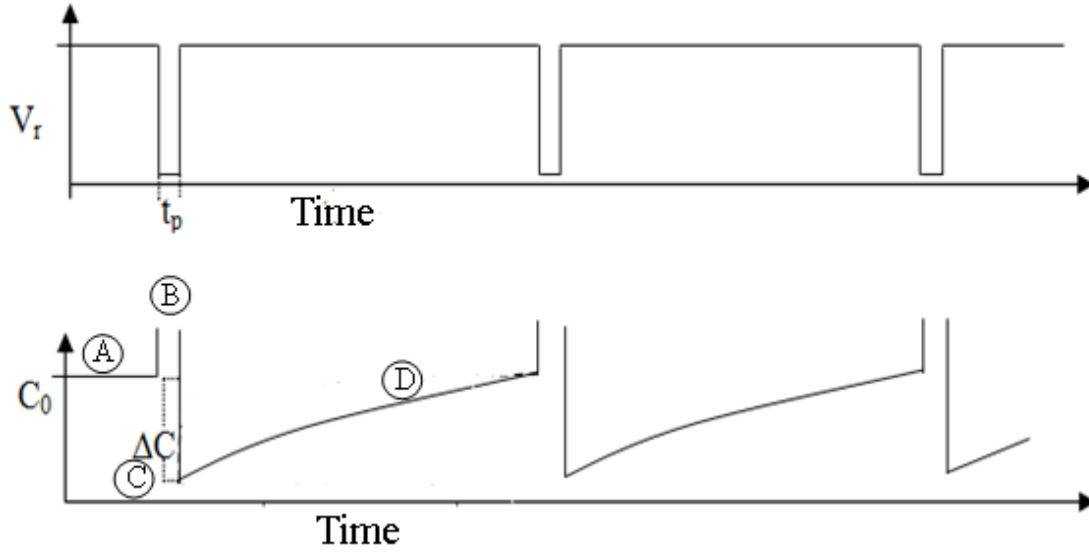


Figure 5.7. The applied bias and the capacitance change of the Schottky device as a function of time.

The periodic applied pulse and the corresponding periodic capacitance transient are shown in Figure 5.7. The capacitance transient is related to the emission rate by the following relationship:

$$C(t) = C_o + \Delta C \exp(-te_n) \quad 5.6$$

where C_0 is the junction capacitance at steady-state reverse bias voltage and ΔC is the difference in capacitance between case A and case C (difference in capacitance change between the two edges of the filling pulse) and can be expressed as

$$\Delta C = A \sqrt{\frac{\epsilon \epsilon_0 e N_D}{2(V_r + V_d)}} - A \sqrt{\frac{\epsilon \epsilon_0 e (N_D + N_t)}{2(V_r + V_d)}} \cong C_0 \frac{N_t}{2N_D} \quad 5.7$$

where N_t is the trapping density. The trap concentration N_t is expressed as,

$$N_t = 2 \left(\frac{\Delta C}{C_0} \right) N_D \quad 5.8$$

5.4.3 DLTS Signal Analysis

The DLTS spectrum is generated from the capacitance transient of Figure 5.7 by applying correlation techniques. The simplest kind of correlation is a dual gate (double boxcar) with gates set at t_1 and t_2 proposed by Lang [14] where the capacitance is measured at two times t_1 and t_2 after the end of each filling pulse. The DLTS signal is expressed as

$$S = C(t_1) - C(t_2) \quad 5.9$$

The DLTS starts at low temperature and is recorded by slowly ramping up the temperature. At low temperature, the capacitance transient is slow due to low thermal emission, and the DLTS signal is very small as shown in Figure 5.8 (i). With the increase

of temperature, the decay rate of the capacitance transient increases. Therefore, the difference between the capacitance at times t_1 and t_2 become greater which result in a larger value of the DLTS signal. This increase of DLTS signal continues with temperature until most of the transient decay takes place which is before time t_1 as shown in Figure 5.8 (ii - vi). After that temperature, the DLTS signal starts to decrease with further increase of temperature as shown in Figure 5.8 (vii - ix). When the temperature is too high, the capacitance transient ends before time t_1 , and the DLTS signal is zero as shown in Figure 5.8 (x). A peak is reveal when the DLTS signal is plotted as function of sample temperature.

The DLTS peak appearance depends upon the selection of t_1 and t_2 which is termed as “rate window” selection. In DLTS, thermal scan peaks appear only when the trap emission rate falls into the rate window. For a given rate window, a DLTS peak related to a trap with a higher emission rate will move to higher temperature. Since the emission rate is strongly temperature dependent, peak related to a trap’s level will appear when its emission rates coincide with the rate window. Hence, in DLTS, peaks corresponding to different traps appear as a function of temperature as shown in Figure 5.9. Signals from different defect levels can be resolved in a single DLTS scan.

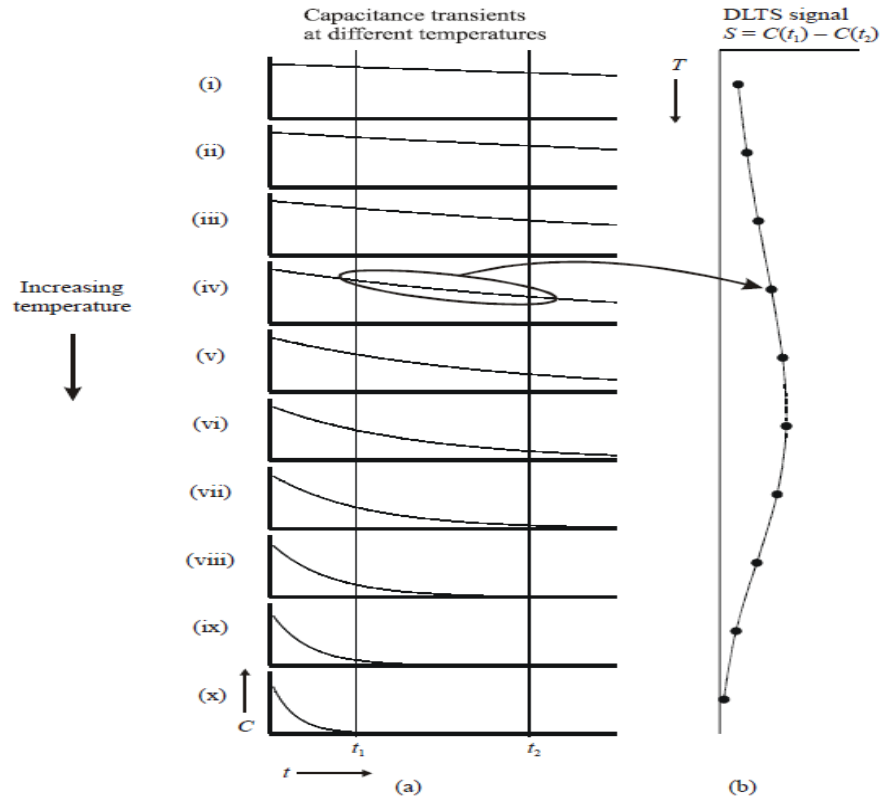


Figure 5.8. (a) Capacitance transient at various temperature (b) DLTS signal obtained by using double boxcar is plotted as a function of sample temperature [14].

The peak position in DLTS spectroscopy depends on the rate window. A larger rate window will shift a defect peak to higher temperature and a smaller rate window will shift a defect peak to lower temperatures. The DLTS has the ability to set rate windows, and a series of spectra can be produced by using different rate windows as shown in Figure 5.10.

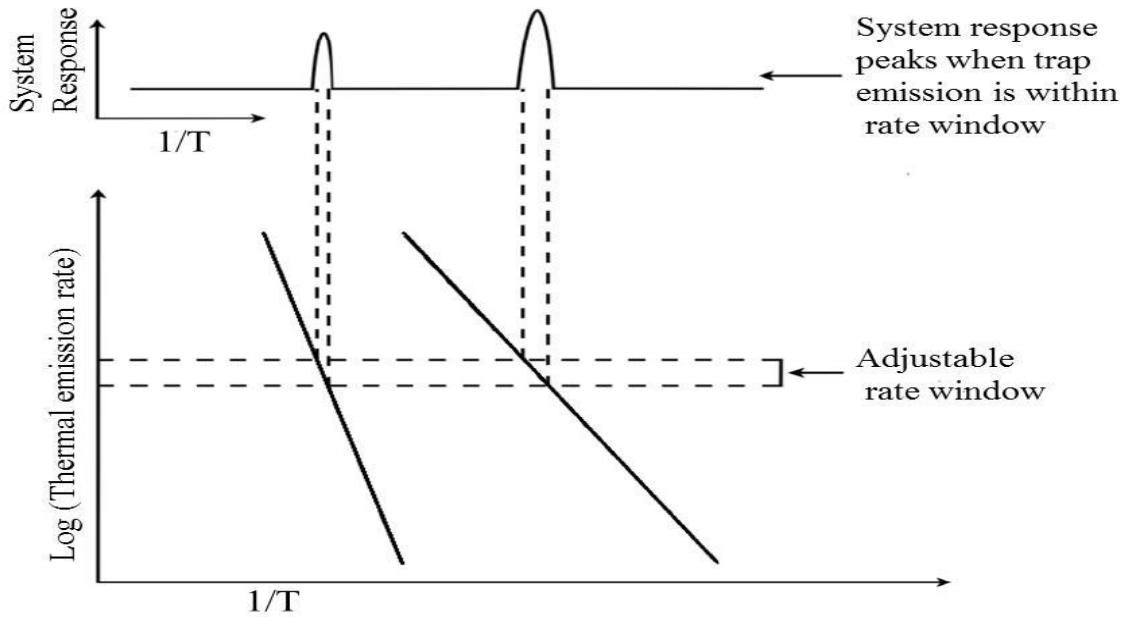


Figure 5.9. An illustration of how a rate window produces a peak in its response when the emission rate of the input signal matches the rate selected by the window [14].

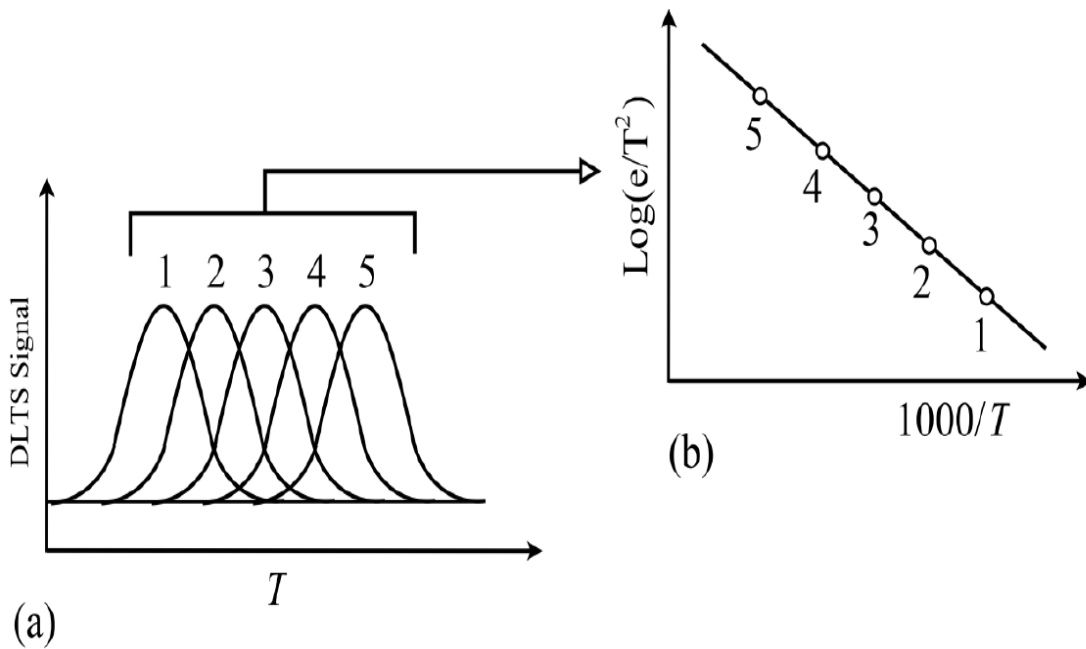


Figure 5.10. (a) The DLTS spectra corresponding to a trap center at various rate windows and (b) the Arrhenius plots obtained from the spectra.

The time constant at maximum height of a DLTS peak can be expressed as

$$\tau_{max} = \frac{\ln(t_2/t_1)}{t_2 - t_1}. \quad 5.10$$

In a DLTS thermal scan, the emission rate at the maximum of a trap peak is a uniquely defined quantity. For each spectrum, the temperature at the maximum peak height can be measured, and the corresponding emission rate e_n is calculated via using Equation 5.10. By using the maximum height of each spectrum, the Arrhenius plot ($\log(e/T^2)$ vs. $1000/T$), corresponding to a particular trap center, can be drawn as shown in Figure 5.10 b. The signature of a trap (i.e. activation energy and capture cross-section) can be extracted from the Arrhenius plot and can be used for defect identification.

5.5 DLTS EXPERIMENTAL SETUP

The DLTS measurements are carried out using a SULA DDS-12 modular DLTS system. The system is comprised of a pulse generator, a capacitance meter, a correlator module, and a PC based data acquisition and analysis software. The block diagram and the photograph of the DLTS system are presented in Figure 5.11 and

Figure 5.12, respectively.

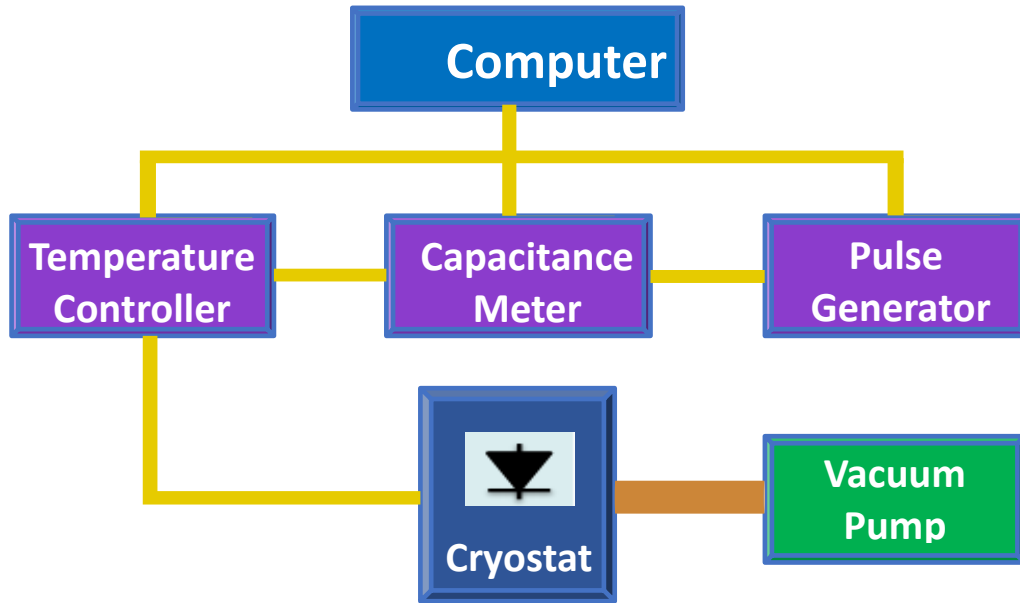


Figure 5.11. Block-Diagram of the SULA DDS-12 DLTS setup.

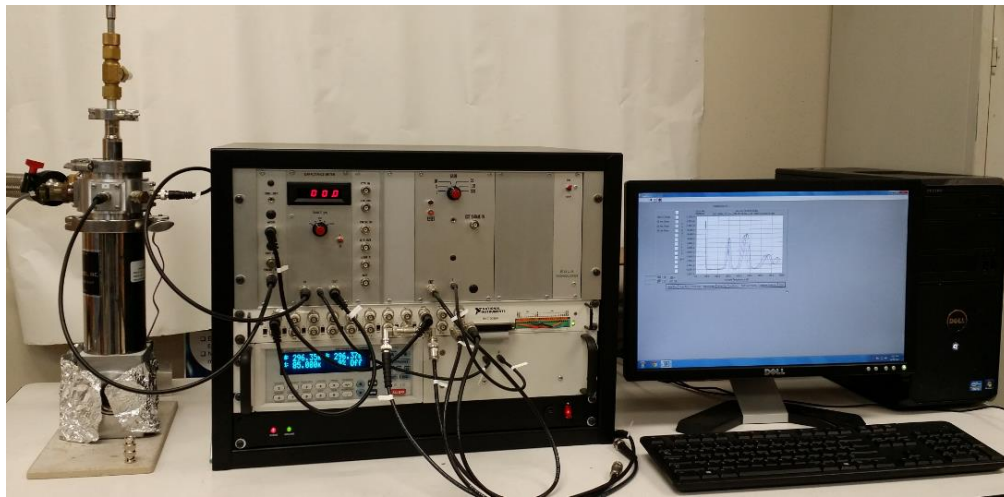


Figure 5.12. Photograph of the SULA DDS-12 DLTS measurement system.

For the measurement, the device under test (Schottky contact) is mounted on a specially designed sample holder inside a JANIS VPF800 cryostat as shown in Figure 5.13. The sample holder is equipped with a sapphire disc which isolates the device electrically but ensures excellent thermal conduction. Tungsten probes are used to

connect the device with the measurement circuit. Connection to the back Ohmic contact was established by placing a piece of copper foil on the sapphire disc. Special care is taken when lowering the top probe so that it will ensure good electrical connection without damaging the Schottky contact. To minimize the damage to the Schottky contact the tips of the probes are kept flat by rubbing with very fine sanding paper.

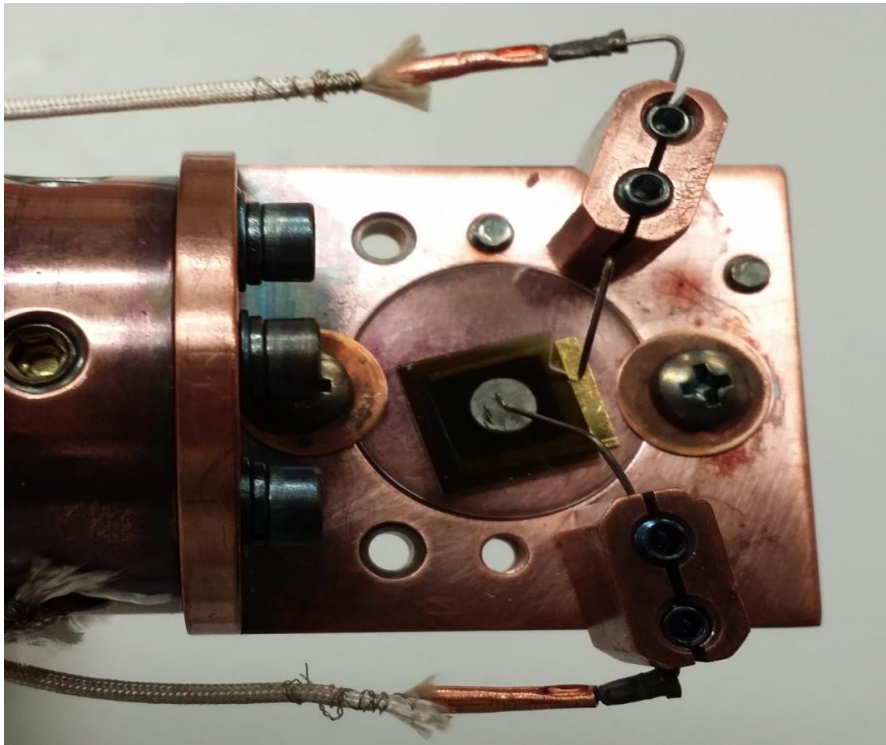


Figure 5.13. Photograph of the sample holder used in DLTS measurements.

The operating temperature of the Cryostat is controlled by a Lakeshore LS335 temperature controller and can be operated in the temperature range of 80 K - 800 K. Cryogenic temperature is reached by liquid nitrogen. During DLTS measurements, the device under test is held in a steady-state reverse bias condition and a pulse is applied periodically to reduce the reverse bias voltage. Repetitive pulsing to the sample is

accomplish by a pulse generator which can generate pulses of magnitude from -12 V to +12 V and width from 1 μ s to pulse repetition period. Usually the pulsing is done to 0 V from the steady-state reverse bias to fill/populate the majority carrier traps present within the depletion (space charge) width. The pulse width is large enough to get ensure saturation trap filling. A self-balancing bridge capacitance meter with a 1 MHz oscillator is used to measure the transient capacitance.

The system is also comprised of a correlator/pre-amplifier module which automatically removes DC background from capacitance meter and amplifies the resultant signal. The correlator module uses a modified double boxcar signal averaging algorithm and measures the capacitance transient in a given rate window. The rate windows are defined by an initial delay which is actually a delay set for the emission rate calculations following the termination of the filling pulse. The initial delay is related to the rate window τ given by

$$\text{Initial delay (ms)} = 1/(4.3 \times \tau) \quad 5.11$$

The DDS-12 system allows the user to collect four DLTS spectra simultaneously which corresponds to four different rate windows in a single temperature scan. The signals were digitized using a NI digitizer card integrated with the DLTS system for live processing using a PC. The entire system including the modules and the temperature controller is controlled using a dedicated Labview interface which also allows the user to analyze the recorded data.

5.5.1 DLTS Spectra of Fabricated Detector

Figure 5.14 (a) & (b) shows representative DLTS spectra in the temperature range of 80 K to 140 K using a smaller set of initial delays, and 80 K to 800 K using a larger set of initial delays, respectively [75]. The peaks appeared at different temperatures corresponding to different defect levels. In total, six distinct peaks were observed in the entire temperature scan range of 80 K - 800 K and are numbered as Peak #1 to #6. The negative peaks indicate that the detected traps are majority carrier traps (electron traps in this case).

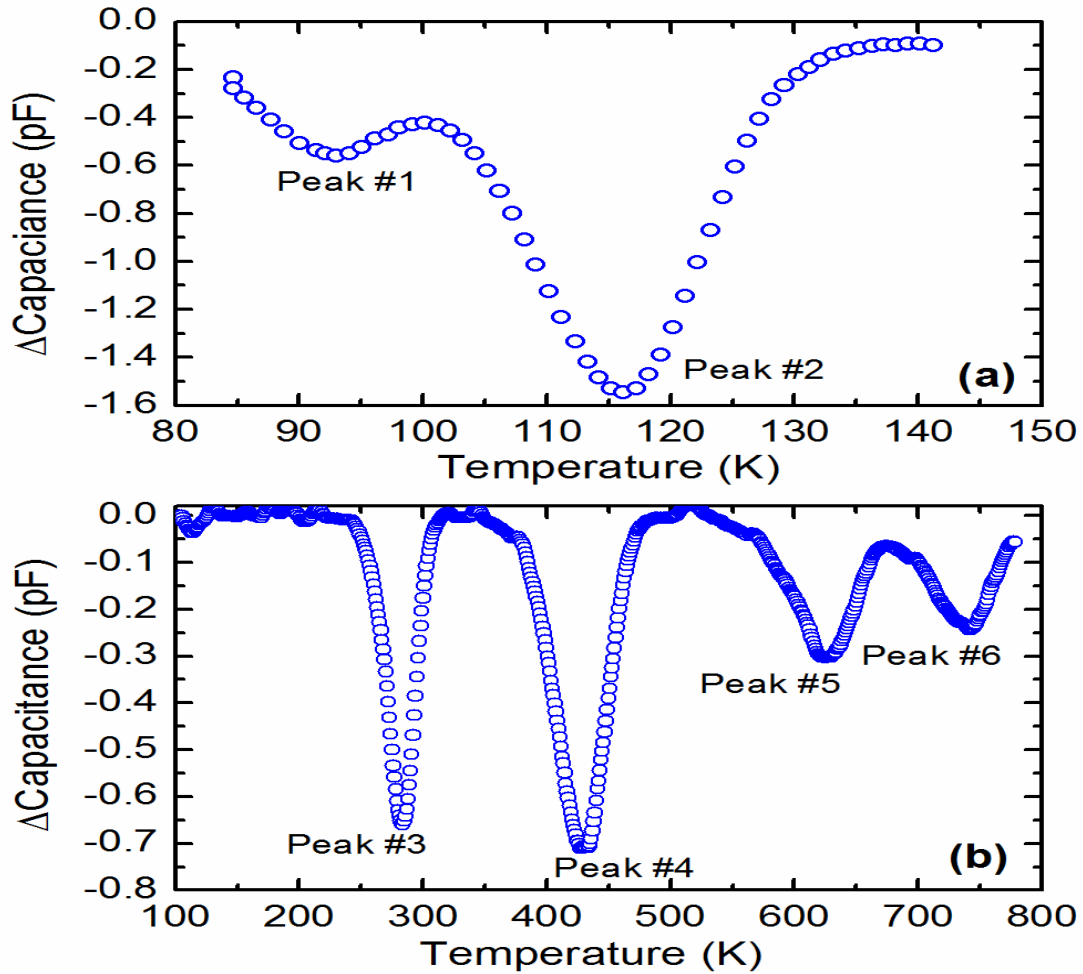


Figure 5.14. DLTS spectra obtained using the 50 μm n-type Ni/4H-SiC epitaxial Schottky barrier radiation detector (AD06) in a temperature range (a) 80 K - 140 K with the smallest initial delay (b) 80 K - 800 K with the largest initial delay.

The DLTS spectra also collected for the detectors (AS1, AS2, and AS3) fabricated on 20 μm 4H-SiC epitaxial layers. Figure 5.15 (a), (b), and (c) shows the DLTS spectra obtained for samples AS2, AS1, and AS3, respectively [2]. In this measurement for reverse bias, a steady state voltage of -2 V was applied, and the samples were pulsed by a 1 ms width, 0 V pulse. Four correlator delays 100 ms, 50 ms, 20 ms, and 10 ms in the temperature range of 230 K - 790 K were used to obtain the DLTS spectra. The peaks correspond to a particular defect, but due to the four different

correlator delays, they were numbered collectively. The peak numbers are used to specify the position of the DLTS peaks on the temperature axis with respect to detector AS2. Detector AS2 showed four DLTS peaks two of which labeled peak #1 and peak #4 were clearly distinguishable peaks. Peak #2 was of very low intensity whereas peak #3 appeared as a partially resolved shoulder. In the DLTS spectra, it is clear that peak #3 is the only prominent peak for the detector AS1, and peak#1 and peak#4 have very low magnitude. The spectra of detector AS3 showed the presence of all the peaks except peak#2.

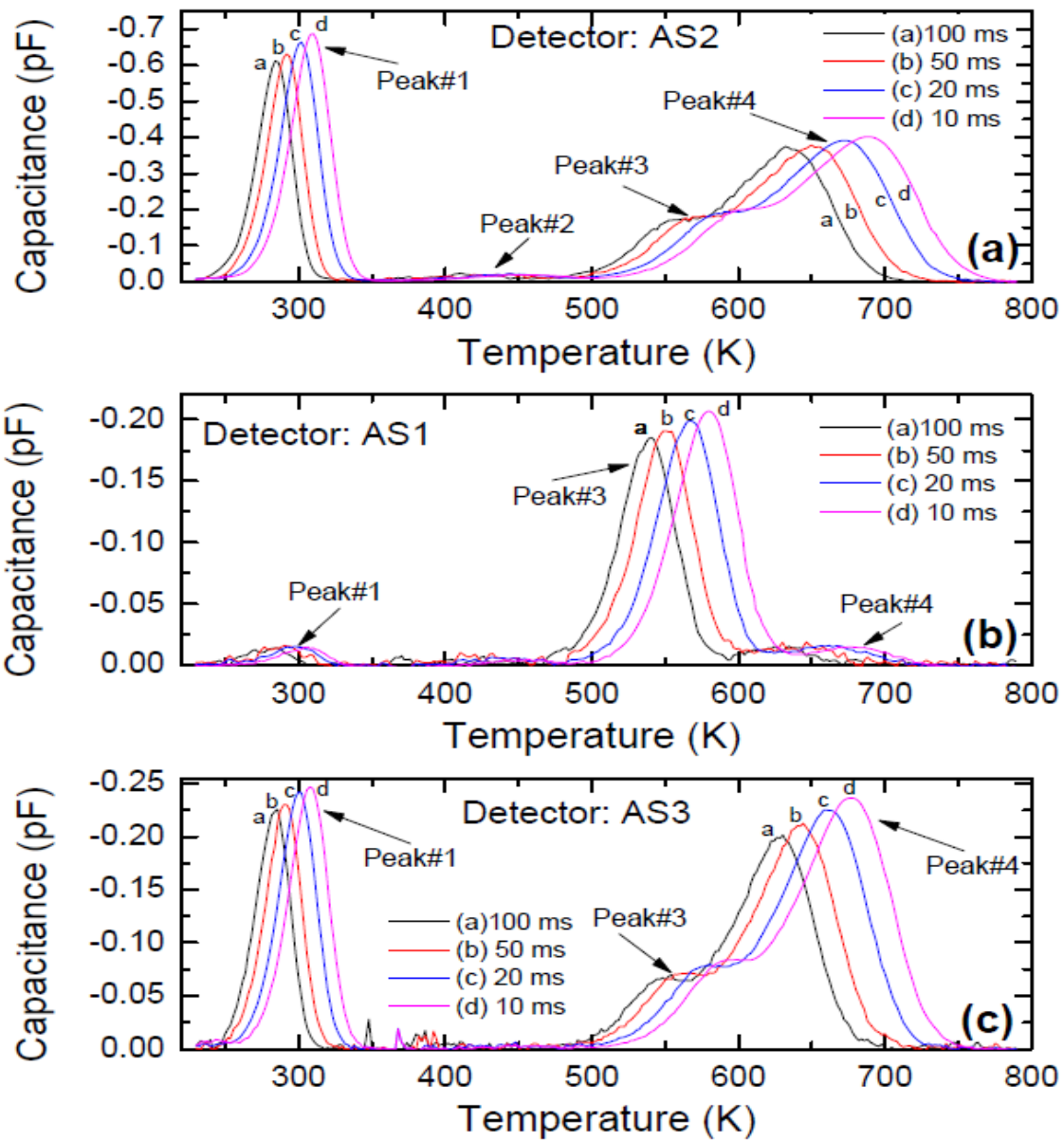


Figure 5.15. DLTS scan for detectors AS2, AS1, and AS3 showing negative peaks related to electron traps present in the 4H-SiC epilayer detectors.

5.5.2 Arrhenius Plot of the Spectra

The activation energies are calculated from the Arrhenius plots (T^2/e_n vs $1000/T$). Figure 5.16 shows the Arrhenius plot for all the peaks obtained

from the DLTS scans. The defect parameters were extracted from the DLTS scans using the equations described above and are summarized in Table 5.3.

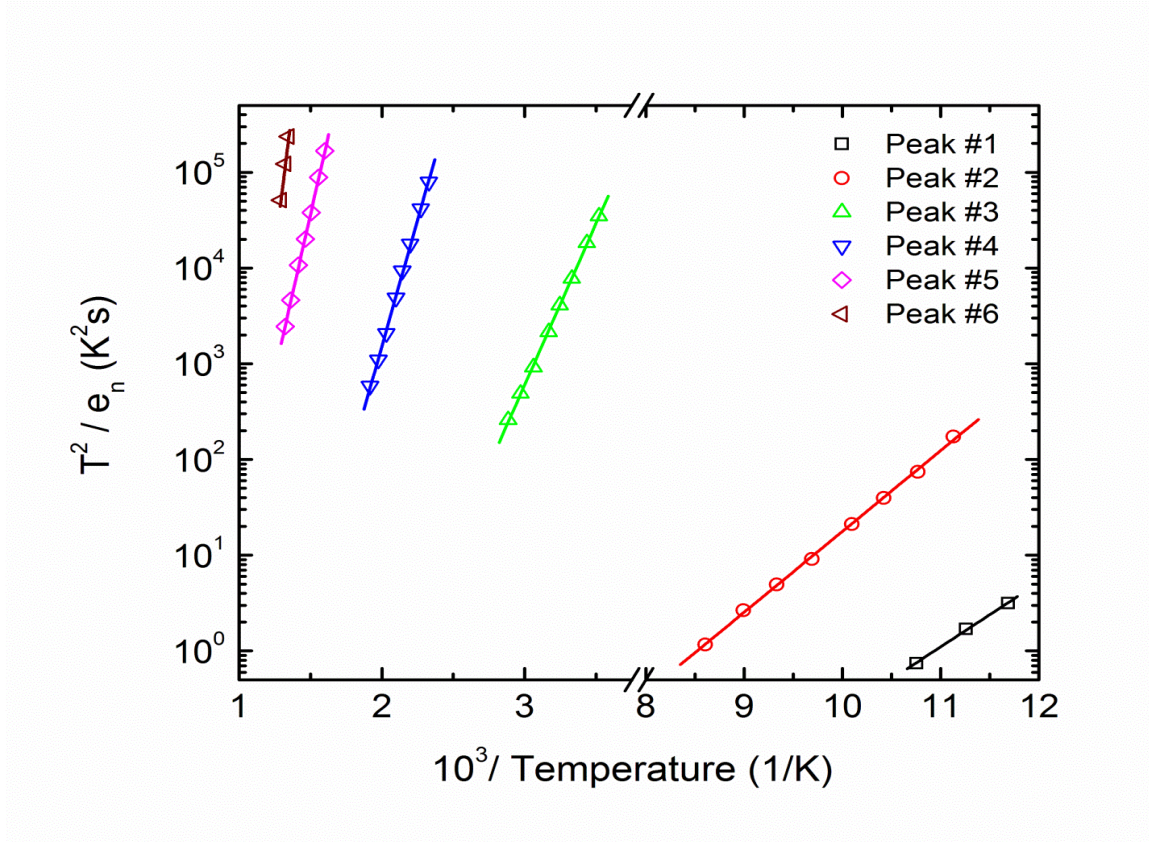


Figure 5.16. Arrhenius plots obtained for the Peaks #1 - #6 corresponding to the DLTS spectra shown in Figure 5.14.

Table 5.3. Defect parameters of the deep levels for the detector AD06

Peak #	σ_n cm ²	ΔE eV	N_t cm ⁻³	Possible Trap Identity
Peak 1	4.13×10^{-15}	$E_c - 0.13$	1.3×10^{13}	Ti (h)
Peak 2	2.50×10^{-15}	$E_c - 0.17$	3.6×10^{13}	Ti (c)
Peak 3	3.36×10^{-15}	$E_c - 0.67$	1.7×10^{13}	$Z_{1/2}$
Peak 4	3.73×10^{-15}	$E_c - 1.04$	2.1×10^{13}	EH ₅
Peak 5	3.22×10^{-17}	$E_c - 1.30$	7.9×10^{12}	Ci1
Peak 6	1.53×10^{-11}	$E_c - 2.40$	5.6×10^{12}	Newly identified

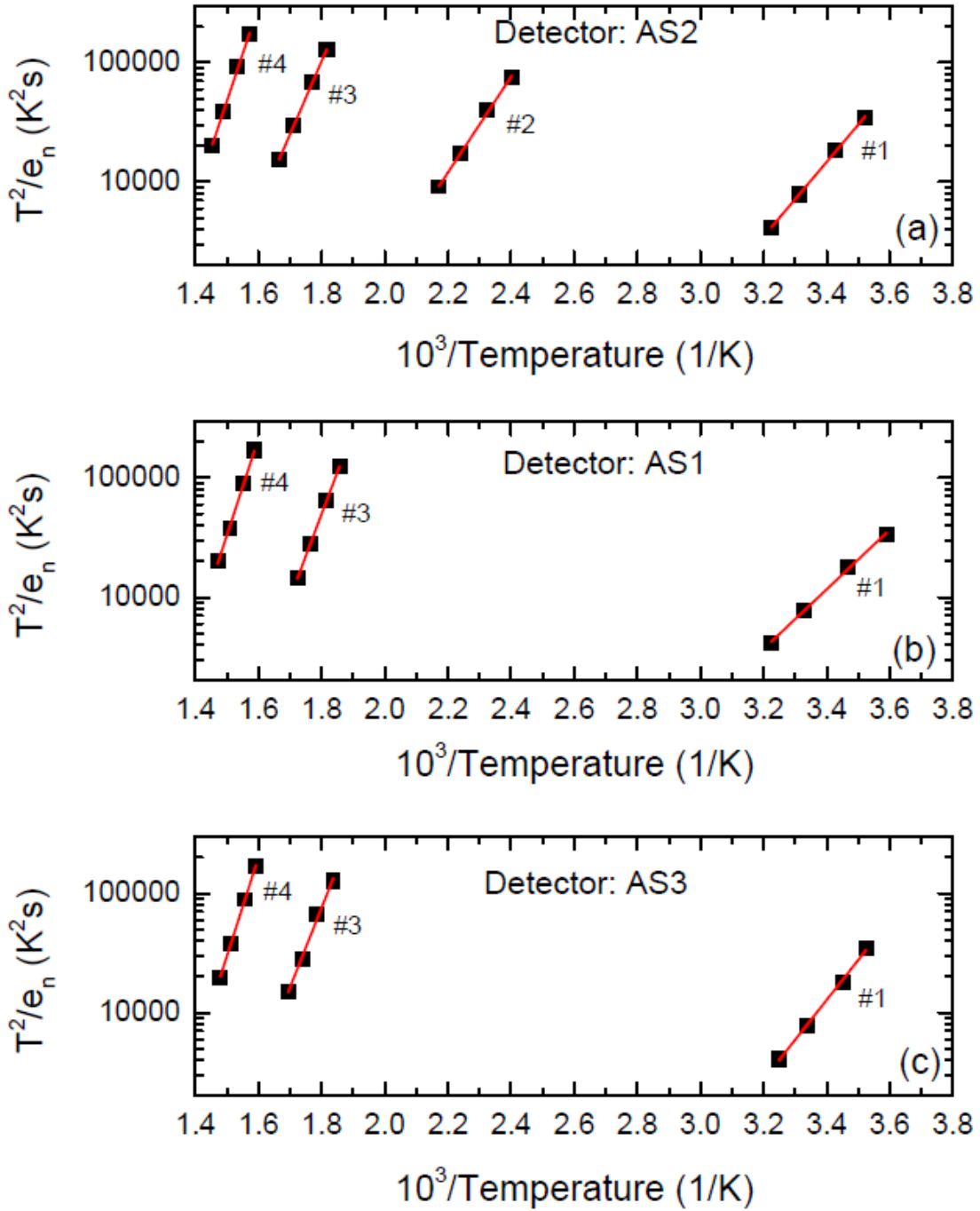


Figure 5.17. Arrhenius plots for determining the activation energy obtained from the DLTS scans shown in Figure 5.15 for detectors (a) AS2, (b) AS1, and (c) AS3. The solid lines show the linear fits.

The Arrhenius plot corresponding to the DLTS spectra (Figure 5.15) of the 20 μm epitaxial layer detectors are shown in Figure 5.17. The defect parameters viz., activation energy, capture cross-section, and trap concentration are calculated for the three detectors AS1, AS2, and AS3 are listed in the Table 5.4, Table 5.5, and Table 5.6, respectively [2].

Table 5.4. Defect parameters of the detector AS1 obtained from the DLTS scans

Peak #	σ_n cm^2	ΔE eV	N_t cm^{-3}	Possible Trap Identity
Peak 1	0.05×10^{-16}	$E_c - 0.60$	0.09×10^{12}	$Z_{1/2}$
Peak 3	575×10^{-16}	$E_c - 1.45$	1.27×10^{12}	Ci1
Peak 4	68.8×10^{-16}	$E_c - 1.6$	0.1×10^{12}	$\text{EH}_{6/7}^b$

Table 5.5. Defect parameters of the detector AS2 obtained from the DLTS scans

Peak #	σ_n cm^2	ΔE eV	N_t cm^{-3}	Possible Trap Identity
Peak 1	1.9×10^{-16}	$E_c - 0.62$	3.2×10^{12}	$Z_{1/2}$
Peak 2	0.1×10^{-16}	$E_c - 0.80$	0.09×10^{12}	V_{si}^+
Peak 3	1.7×10^{-16}	$E_c - 1.31$	0.93×10^{12}	Ci1
Peak 4	28.2×10^{-16}	$E_c - 1.6$	1.9×10^{12}	$\text{EH}_{6/7}^b$

Table 5.6. Defect parameters of the detector AS3 obtained from the DLTS scans

Peak #	σ_n cm^2	ΔE eV	N_t cm^{-3}	Possible Trap Identity
Peak 1	28.8×10^{-16}	$E_c - 0.66$	1.9×10^{12}	$Z_{1/2}$
Peak 3	22.6×10^{-16}	$E_c - 1.3$	65×10^{12}	Ci1
Peak 4	158×10^{-16}	$E_c - 1.6$	1.8×10^{12}	$\text{EH}_{6/7}^b$

5.5.3 Defect Identification

At first the deep level defects found in the detector (AD06) fabricated on 50 μm epitaxial layers as shown in the table are identified by comparing with reported literature data. The trap levels corresponding to Peak #1 and Peak #2 were found to be located at $E_c - 0.13$ eV and $E_c - 0.17$, respectively, where E_c is the conduction band minimum. Both of the defect levels have been identified as titanium substitutional impurity. Dalibor et al. [99, 100] have reported two similar defect levels located at $E_c - (0.117 \pm 0.008)$ eV and $E_c - (0.160 \pm 0.010)$ eV from DLTS studies of Ti^+ implanted 4H-SiC which they attributed to the ionized titanium acceptor Ti^{3+} (3d1) residing at hexagonal and cubic Si lattice sites, respectively. Gelczuk et al. [101] also reported similar trap levels and assigned them to the Ti impurities at hexagonal and cubic Si lattice sites. Zhang et al. [102] also assigned a defect level located at $E_c - 0.16$ eV to a Ti electron trap level. Castaldini et al. [103] assigned a trap level located at $E_c - 0.17$ to chromium or titanium impurities (acceptor like) in hexagonal position.

The trap center related to Peak #3 was found to be located at 0.67 eV below the conduction band edge. Several groups have reported the presence of a similar defect level often designated as $Z_{1/2}$ [104, 105, 106, 107, 108]. However, the exact microscopic structure is still unknown and several theories exist in the literature regarding the probable structure of $Z_{1/2}$ centers. As summarized by Zhang et al. [102], $Z_{1/2}$ is most likely related to defect complexes involving equal number of carbon and silicon sites. The possible structures listed by them, obtained from the existing literatures [95, 104, 109],

are silicon carbon vacancy complexes ($V_{Si} + V_C$), antisite complex ($Si_C + C_{Si}$) pairs, or a pair of an antisite and a vacancy of different atoms. However, their own findings were more inclined towards a divacancy like structure of the $Z_{1/2}$ defect. Eberlein et al. [110] on the other hand, reported that the participation of carbon interstitial with nitrogen can also form defect levels with similar activation energy. $Z_{1/2}$ center is also reported to be responsible for the reduction of carrier lifetime by several authors [101, 111, 112, 113]. The activation energy corresponding to peak #4 was found to be located at 1.04 eV below the conduction band edge. A defect level reported by Alfieri et al. [114] located at $E_c - 1.03$ eV and designated as EH_5 , is the closest match with the peak #4 observed in our case. Beyer et al. have also detected a similar defect level ($E_c - 1.07$ eV) in 2.5 MeV electron irradiated 4H-SiC [115]. EH_5 defect has been found in ion irradiated 4H-SiC and has been attributed to a carbon cluster [95]. The activation energy of peak #5 was found to be 1.30 eV. Alfieri et al. [114] reported a similar defect center $Ci1$ in a chlorine implanted n-type 4H-SiC epitaxial layer. The peak #6 was found to have the highest activation energy (2.40 eV) among all the defect centers observed in the DLTS scans and remains unidentified as the corresponding activation energy does not match with any known defect level in 4H-SiC that has been reported in the literature. The trap concentrations corresponding to peak #1 - #4 were all of the order of 10^{13} cm^{-3} with the Ti impurity (cubic Si site) being the maximum. Peak #5 and #6 were found to be one order of magnitude less in concentration.

In this stage, the deep level defects found in the detectors (AS1, AS2, and AS3) fabricated on 20 μm epitaxial layers were identified. The deep level defects for the

detector AS1, AS2, and AS3 are shown in the table, respectively. Four peaks corresponding to four different defects are found for the detector AS2. The defect related peak position for the detectors AS1 and AS2 are numbered with respect to the AS2 peak position.

The DLTS spectra of detector AS2 showed four peaks and are numbered as peak #1 to peak #4. The calculated parameters of the defects found in the detector AS2 are summarized in the table. According to the calculated activation energy, the position of peak #1 was found to be at $E_c - 0.62$ eV. A similar kind of defect has been identified as carbon vacancy (V_c) or its complexes in 4H-SiC samples by several workers [104, 105, 106, 107, 108]. This defect level is often designated as $Z_{1/2}$ center and is regarded as a potential lifetime killer [111, 112, 113, 102]. The position of the defect related to weak peak #2 was found to be at $E_c - 0.8$ eV. A similar defect level was observed by Nava *et al.* [108] in neutron irradiated n-type 4H-SiC using photo-induced current transient spectroscopy and was identified as silicon vacancy in singly positive charge state (V_{si}^+). The defect related to peak #2 was found to have a much less concentration of $9 \times 10^{10} \text{ cm}^{-3}$ and a low capture cross-section of $1 \times 10^{-17} \text{ cm}^2$ and thus may not have a substantial effect in defining the detector performance in this case. The position of shouldered peak #3 in the band-gap was calculated to be at $E_c - 1.31$ eV. The peak could not be identified with any known or reported defect level in the literature. Alfieri *et al.* [114] reported similar defect level observed in chlorine implanted n-type epitaxial 4H-SiC and labeled it as Ci1. The position of peak #4 in the band-gap was calculated to be at $E_c - 1.6$ eV. Nava *et al.* [108] identified a similar defect level as V_c and its complex in neutron irradiated n-type

4H-SiC using photo-induced current transient spectroscopy. K. Danno *et al.* [116] designated a defect center at $E_c - 1.55$ eV as $EH_{6/7}$ and related it to carbon vacancies or carbon-silicon di-vacancies.

For the detector AS1 and AS3 three peaks (peak #1, peak #3, and peak #4) were found to be related to the same defect levels as found in detector AS2. The defect related to the peak #2 in the detector AS2 which is identified as V_{si}^+ is not found in AS1 and AS3. By comparison of the defect parameters in detectors AS2 and AS3, it can be observed that the capture cross-sections corresponding to defects related to peak #1, #3, and #4 in AS3 were significantly higher than those in AS2. The comparison of the defect parameters in the detectors AS1 and AS2 shows that the detector AS1 has only the high concentration of the defect $Ci1$ (related to peak #3) and has very low concentration of the defect $Z_{1/2}$ (related to peak #1) and the defect $EH_{6/7}$ (related to peak #4).

5.6 DEFECTS' ROLE ON DETECTOR PERFORMANCE

To determine the defects' role on the device performance, the detector properties and electrically active defects are needed to correlate. Important detector properties and calculated defects' parameters are summarized in a separate table for each of the fabricated detectors. Let us first consider the detectors fabricated on 20 μm epitaxial layers. The summarized properties of the detectors AS1, AS2, and AS3 are shown in the Table 5.7, Table 5.8, and Table 5.9, respectively.

In Table 5.8, it is shown that four deep level defects $Z_{1/2}$, V_{si}^+ , Ci1, and $EH_{6/7}$ are observed in the detector AS2. The resolution of this detector was calculated to be 0.38%. The resolution of detector AS3 was calculated to be 0.96%. Three deep level defects $Z_{1/2}$, Ci1, and $EH_{6/7}$ are identified in this detector as shown in Table 5.9. All the defects identified in AS2 except the defects V_{si}^+ are found in AS3. From the comparison of the defect parameters in detectors AS2 and AS3, it is found that the capture cross-sections of the defects $Z_{1/2}$, Ci1, and $EH_{6/7}$ in AS3 are significantly higher than those in AS2. This suggests higher probability of electron trapping in detector AS3 and hence explains the comparatively poor performance. The deep level defects $Z_{1/2}$, Ci1, and $EH_{6/7}$ are also identified in the detector AS1 as shown in the Table 5.7. Among all the defects in AS1, only Ci1 has a much higher concentration compared to the defects $Z_{1/2}$ and $EH_{6/7}$ which are also clear from the high amplitude of the peak #2 in the DLTS spectra of AS1 as shown in Figure 5.15 in section 5.5. The trap concentration of the defects $Z_{1/2}$ and $EH_{6/7}$ in AS1 are found to be one order of magnitude less compared to those found in AS2 and AS3. The capture cross-section of the defect Ci1 in AS1 is found to be much higher compared to any other defects among all the samples. However, the superior performance of detector AS1 indicates that the defect Ci1 does not significantly affect the detector performance. The above analysis suggests that among the defects identified in these n-type 4H-SiC 20 μm epitaxial layers the defects $Z_{1/2}$ (located at $E_c - 0.6$ eV) and $EH_{6/7}$ (located at $E_c - 1.6$ eV) seems have major role in determining the detector performance.

Table 5.7. Detector properties and defect parameters for the detector AS1

Detector Characterization		Defect Parameters			
Ideality Factor	1.2	Trap Identity	σ_n (cm ²)	ΔE (eV)	N_t (cm ⁻³)
ϕ_B (eV)	1.6	$Z_{1/2}$	0.05×10^{-16}	$E_c - 0.60$	0.09×10^{12}
Leakage Current at - 100 V (pA)	4.3				
N_d (cm ⁻³)	2.6×10^{14}	Ci1	75×10^{-16}	$E_c - 1.45$	1.27×10^{12}
Resolution (%)	0.29	EH _{6/7}	68.8×10^{-16}	$E_c - 1.6$	0.1×10^{12}

Table 5.8. Detector properties and defect parameters for the detector AS2

Detector Characterization		Defect Parameters			
Ideality Factor	1.09	Trap Identity	σ_n (cm ²)	ΔE (eV)	N_t (cm ⁻³)
ϕ_B (eV)	1.67	$Z_{1/2}$	1.9×10^{-16}	$E_c - 0.62$	3.2×10^{12}
Leakage Current at - 100 V (pA)	6.2	V_{si}^+	0.1×10^{-16}	$E_c - 0.80$	0.09×10^{12}
N_d (cm ⁻³)	3.2×10^{14}	Ci1	1.7×10^{-16}	$E_c - 1.31$	0.93×10^{12}
Resolution (%)	0.38	EH _{6/7}	1.58×10^{-16}	$E_c - 1.6$	1.8×10^{12}

Table 5.9. Detector properties and defect parameters for the detector AS3

Detector Characterization		Defect Parameters			
Ideality Factor	1.24	Trap Identity	σ_n (cm ²)	ΔE (eV)	N_t (cm ⁻³)
ϕ_B (eV)	1.15	$Z_{1/2}$	28.8×10^{-16}	$E_c - 0.66$	1.9×10^{12}
Leakage Current at - 100 V (pA)	10				
N_d (cm ⁻³)	3.0×10^{14}	Ci1	22.6×10^{-16}	$E_c - 1.3$	65×10^{12}
Resolution (%)	0.96	EH _{6/7}	158×10^{-16}	$E_c - 1.6$	1.8×10^{12}

The summarized detector properties and the defect parameters of the detector (AD06) fabricated on 50 μm epitaxial layers are shown in Table 5.10. Six defects are found in detector AD06, and the resolution is calculated to be 1.8 %. Among the defects, Ti(h) and Ti(c) are shallow levels. The deep level defects $Z_{1/2}$ and EH_5 have the concentrations of the order of 10^{13} cm^{-3} with the capture cross-section on the order of 10^{-15} cm^2 . On the other hand, both the concentration and capture cross-section of deep level Ci1 are smaller compared to those of $Z_{1/2}$ and EH_5 . For 20 μm epitaxial layer, it is found that deep level Ci1 does not affect the detector performance. Though the deep level $\text{EH}_{6/7}$ (located at $\sim E_c - 1.6$) was not found in AD06 and the defect parameters of $Z_{1/2}$ and EH_5 are in tolerable limit, the resolution of AD06 is still much higher than 1%. The extremely high capture cross-section ($1.53 \times 10^{-11} \text{ cm}^2$) of the newly identified defect (located at $\sim E_c - 2.4$) seems to be a significant role in determining the detector performance.

Table 5.10. Detector properties and defect parameters for the detector AD06

Detector Characterization		Defect Parameters			
Ideality Factor	1.2	Trap Identity	$\sigma_n (\text{cm}^2)$	$\Delta E (\text{eV})$	$N_t (\text{cm}^{-3})$
$\phi_B (\text{eV})$	1.7	Ti(h)	4.13×10^{-15}	$E_c - 0.13$	1.3×10^{13}
Leakage Current at - 100 V (nA)	9.0	Ti(c)	2.50×10^{-15}	$E_c - 0.17$	3.6×10^{13}
		$Z_{1/2}$	3.36×10^{-15}	$E_c - 0.67$	1.7×10^{13}
$N_d (\text{cm}^{-3})$	3.2×10^{14}	EH_5	3.73×10^{-15}	$E_c - 1.04$	2.1×10^{13}
		Ci1	3.22×10^{-17}	$E_c - 1.30$	7.9×10^{12}
Resolution (%)	1.8	Newly identified	1.53×10^{-11}	$E_c - 2.40$	5.6×10^{12}

5.7 CONCLUSION

Deep level transient spectroscopy (DLTS) studies were conducted to investigate the defect levels present in the detectors fabricated on different thickness of 4H-SiC epitaxial layers. In the fabricated detectors different deep level defects were observed in the temperature scan range of 80 K - 800 K. Types of observed defects and their parameters varied widely from detector to detector. In all of the detectors fabricated on 20 μm thick epitaxial layers, deep level defects $Z_{1/2}$ located at $E_c - 0.6$ eV, Ci1 located at $E_c - 1.3$ eV, and $\text{EH}_{6/7}$ located at $E_c - 1.6$ eV were revealed by the DLTS measurement. Among them, two defect levels (electron traps) $Z_{1/2}$ and $\text{EH}_{6/7}$ related to carbon vacancies and their complexes mostly affected the detector resolution. Defect level observed at $E_c - 1.3$ eV was found to not affect the detectors' performance.

For the case of 50 μm epitaxial layer detector, six different defect centers were detected in the same DLTS temperature scan range of 80 K - 800 K. Defects were identified as Ti (h) at $E_c - 0.13$ eV, Ti (c) at $E_c - 0.17$ eV, $Z_{1/2}$ at $E_c - 0.67$ eV, EH_5 at $E_c - 1.04$ eV, Ci1 at $E_c - 1.3$ eV, and a newly detected deep level at $E_c - 2.4$ eV. A Deep level detected located at $E_c - 2.4$ eV was identified for the first time and has not been reported to date. Along with $Z_{1/2}$ and EH_5 , the newly identified defect at $E_c - 2.4$ eV mostly affected the detector resolution fabricated on 50 μm 4 H-SiC epitaxial layers.

CHAPTER 6: ANNEALING BEHAVIOR OF CRYSTALLINE DEFECTS

6.1 INTRODUCTION

For the annealing behavior studies of SiC crystalline defects, nickel (Ni) Schottky barrier diodes are fabricated on 50 μm thick n-type 4H-SiC epitaxial layers. Deep level transient spectroscopy (DLTS) measurements were carried out on the fabricated Schottky diodes in a wide temperature range from 80 K to 800 K to determine the initial defect parameters (i.e. defect densities, capture cross-sections, and activation energies) prior to the first iteration of isochronal annealing. Isochronal annealing of the devices was carried out over the temperature range from 100 $^{\circ}\text{C}$ to 800 $^{\circ}\text{C}$. The defect parameters were then compared with the initial DLTS scans of the unannealed devices.

6.2 DEEP LEVEL TRANSIENT SPECTRA BEFORE ANNEALING

Schottky barrier diodes were fabricated on 50 μm thick n-type 4H-SiC epitaxial layers to characterize the initial deep level defects. Parameters of the deep level defects are determined by the DLTS measurements on the fabricated detectors. Figure 6.1 (a) shows representative DLTS spectra in the temperature range of 85 K to 130 K using a smaller set of initial delays, and Figure 6.1 (b) shows DLTS spectra in the temperature

range 200 K to 800 K using a larger set of initial delays. The peaks appeared at different temperatures corresponding to different defect levels. In total, four distinct peaks were observed in the entire temperature scan range of 85 K - 800 K and are numbered as peak #1 to peak #4.

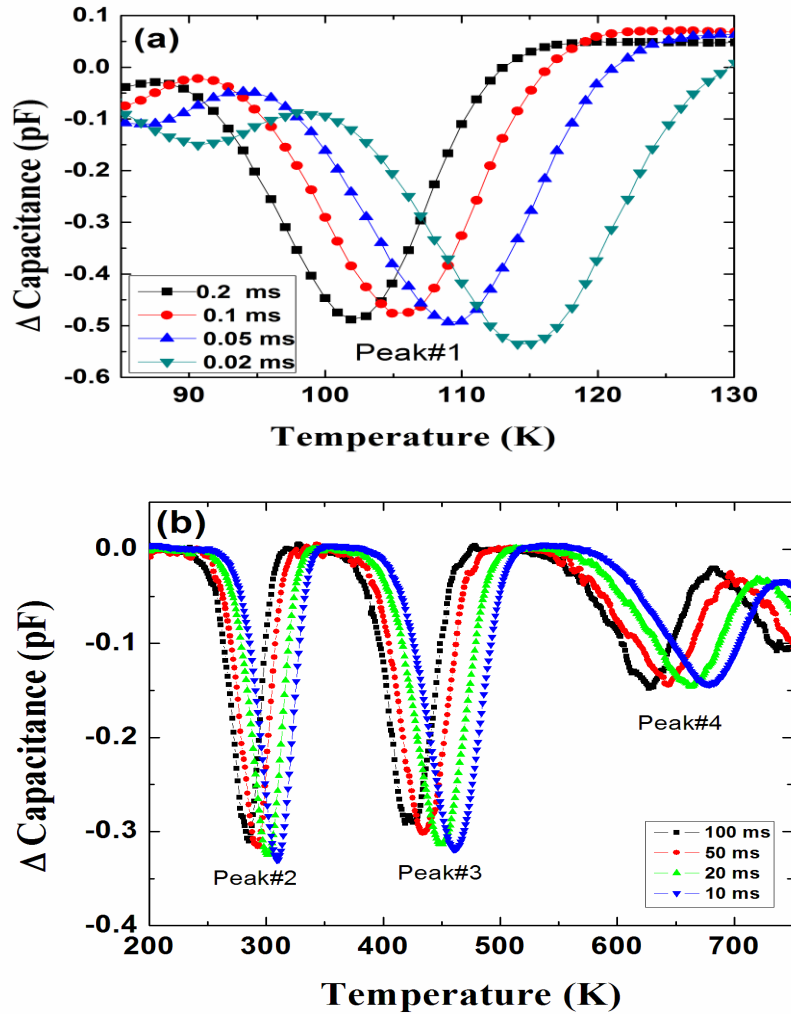


Figure 6.1. DLTS spectra obtained using the 50 μ m thick n-type Ni/4H-SiC unannealed epitaxial Schottky barrier in the temperature range: (a) 85 K - 130 K with a smaller set of initial delays, and (b) 200 K - 800 K with a larger set of initial delays.

The negative peaks indicate that the detected traps are majority carrier traps (electron traps in this case). The activation energy is calculated from the Arrhenius plots (T^2/e_n vs $1000/T$). Figure 6.2 shows the Arrhenius plots for all the peaks obtained from the DLTS scans. The defect parameters were extracted from the DLTS scans described above and are summarized in Table 6.1.

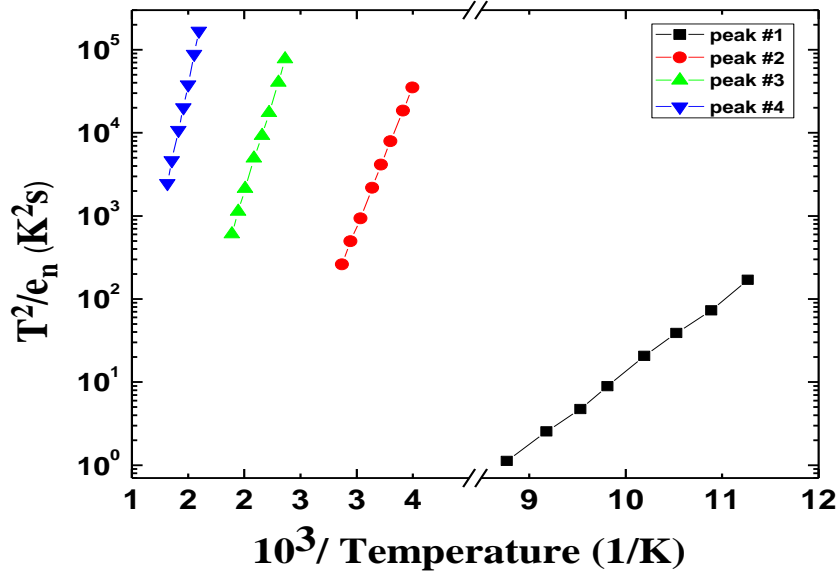


Figure 6.2. Arrhenius plots obtained for the peaks #1 - #4 corresponding to the DLTS spectra shown

Table 6.1. Defect Parameters Obtained from the DLTS Measurements.

Peak #	σ_n cm^2	ΔE eV	N_t cm^{-3}	Possible Trap Identity
Peak 1	6.62×10^{-15}	$E_c - 0.17$	1.7×10^{13}	Ti (c)
Peak 2	3.37×10^{-15}	$E_c - 0.67$	7.1×10^{12}	$Z_{1/2}$
Peak 3	5.56×10^{-17}	$E_c - 1.04$	7.1×10^{12}	EH ₅
Peak 4	2.66×10^{-17}	$E_c - 1.60$	3.3×10^{12}	EH _{6/7}

6.3 EXPERIMENT FOR ISOCHRONAL ANNEALING STUDIES

An annealing experimental set-up has been assembled at USC for the annealing studies of the defects. The annealing set-up comprises of a furnace with a temperature control unit, an oil-free mechanical pump, a turbo-molecular pump, vacuum gauge controller, and turbo pump controller. The block diagram of the isochronal annealing experimental set up is shown in Figure 6.3.

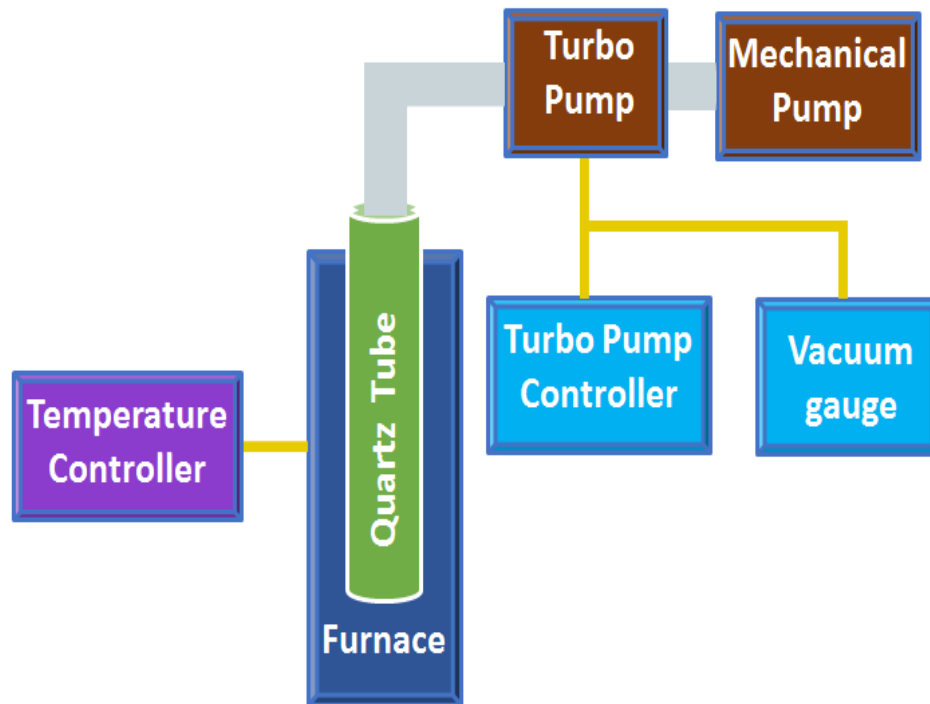


Figure 6.3. Block diagram of annealing set up at USC.

For isochronal annealing, a sample is loaded in a quartz ampoule and then connected to the vacuum system of the annealing experimental set-up as shown in Figure 6.4. After the loaded quartz ampoule was pumped down by the mechanical pump for 30

minutes, the turbo pump was turned on to achieve higher vacuum pressure levels. A Varian Multi-Gauge ionization gauge was used to monitor the vacuum pressure level. After reaching the vacuum pressure level of 2×10^{-7} torr, the ampoule was lowered to the hot zone of a dedicated single-zone tube furnace to be annealed. The temperature of the furnace was controlled by a Thermolyne temperature control unit. Moreover, a digital thermocouple is connected to the ampoule for cross-checking the annealing temperature.

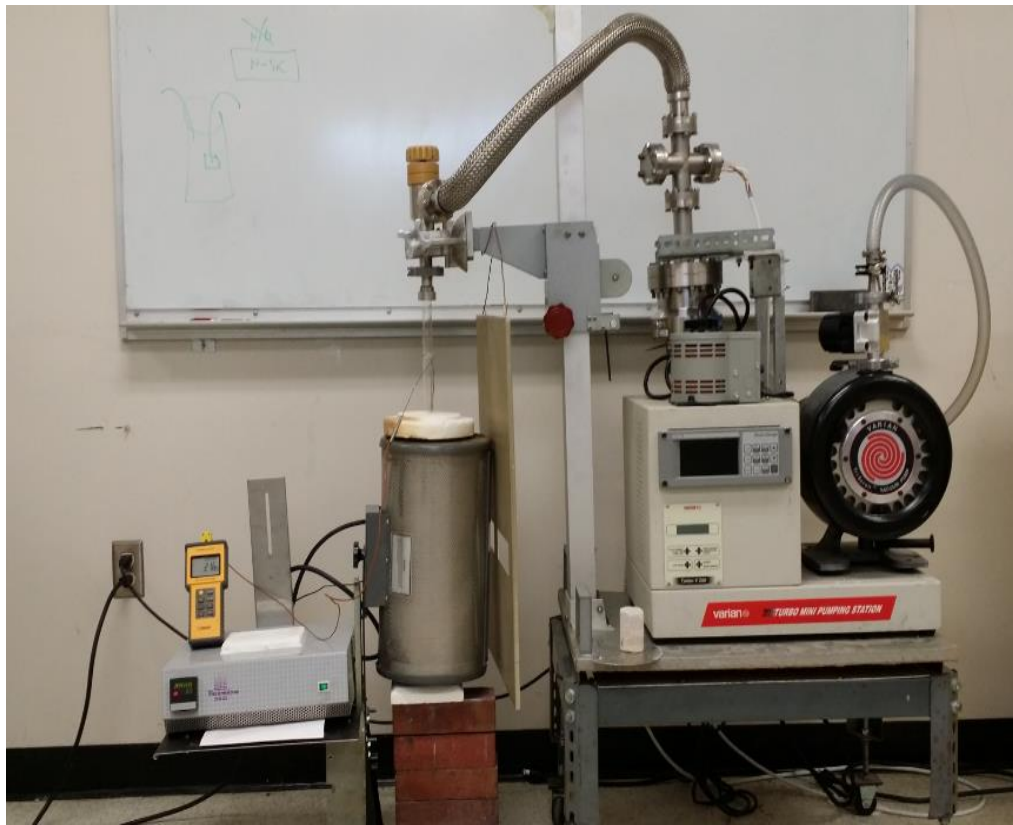


Figure 6.4. Picture of the annealing set up at USC.

After characterization of the initial defects of 4H-SiC epitaxial layer by DLTS measurement, the Schottky devices are ready for annealing. Before annealing, the top and bottom nickel contact of the Schottky devices were completely etched off by

concentrated nitric acid. Then the samples are annealed for 30 minutes. After annealing at each temperature, the samples are cleaned by RCA cleaning procedure and Ni Schottky and Ohmic contacts are deposited for subsequent I-V, C-V, and DLTS measurements.

6.4 ANNEALING STUDIES RESULTS

6.4.1 Electrical characteristics after annealing

Figure 6.5 shows the I-V (current-voltage) characteristics of the fabricated Schottky barrier devices before and after isochronal annealing at different temperatures. It is observed that the forward current for an applied voltage beyond the knee voltage is decreased up to the annealing temperature of 400 °C and then increased again till the temperature of 800 °C which is a limit of our isochronal annealing studies. Figure 6.6 shows the reverse bias characteristics of the fabricated Schottky diode and after annealing at different temperatures. The reverse bias current is almost same up to the annealing of 400 °C and increased significantly with annealing at 600 °C and 800 °C, respectively.

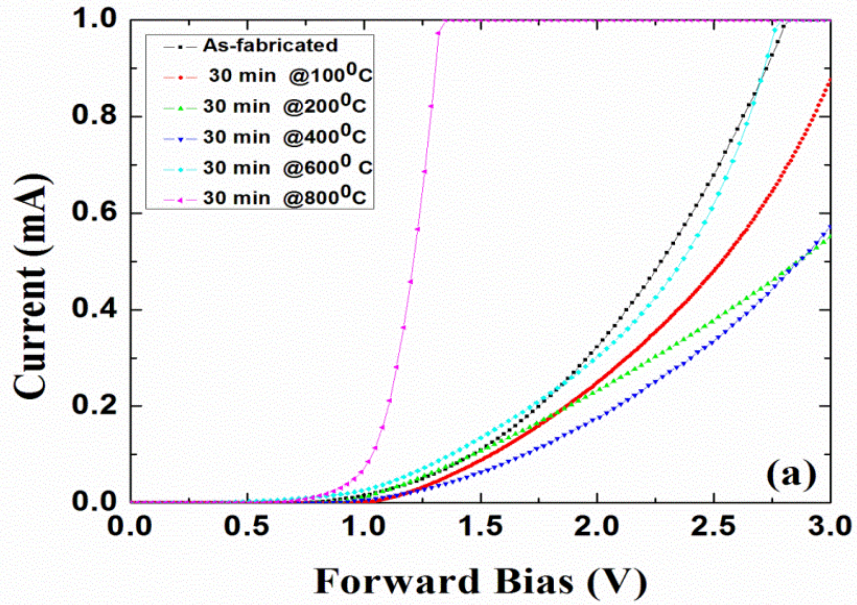


Figure 6.5. Forward current voltage (I-V) characteristics of the as-fabricated 50 μm thick n-type 4H-SiC Schottky barrier and after isochronal annealing at different temperatures:

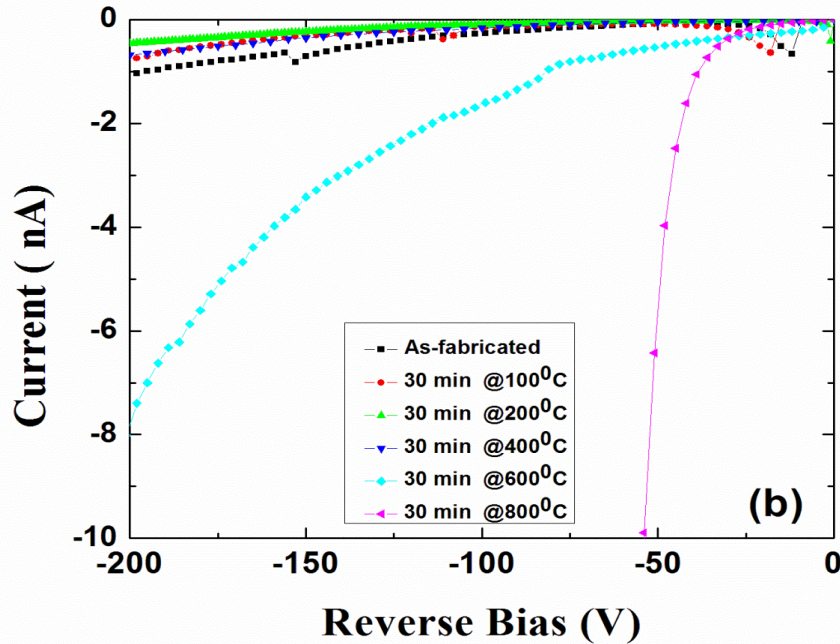


Figure 6.6. Reverse current voltage (I-V) characteristics of the as-fabricated 50 μm thick n-type 4H-SiC Schottky barrier and after isochronal annealing at different temperatures:

The calculated ideality factor from the forward I-V characteristics is shown in Figure 6.7. A comparison of the ideality factors of fabricated devices before and after annealing at different temperatures revealed the presence of spatial non-uniformities in barrier heights over the metal contact area [117]. The total diode current is an aggregate of the current flowing through different barrier height regions in the metal semiconductor interface. Low barrier height turns on at a lower bias than the high barrier height region and the non-ideality in the diode characteristics arises. The ideality factor of the unannealed SiC Schottky barrier is significantly higher than ideality factors found after annealing at different temperatures.

Calculated ideality factor of ~ 1.6 of the as-fabricated Schottky barrier suggests the presence of high density patches of small barrier heights [50, 118, 119]. The ideality factor reduces to ~ 1.2 after annealing at $100\text{ }^{\circ}\text{C}$, implying the major reduction of the density of patches. The density of low barrier height patches do not change significantly with further annealing at higher temperatures which is also clear from the small variation of ideality factor throughout the annealing studies up to $800\text{ }^{\circ}\text{C}$.

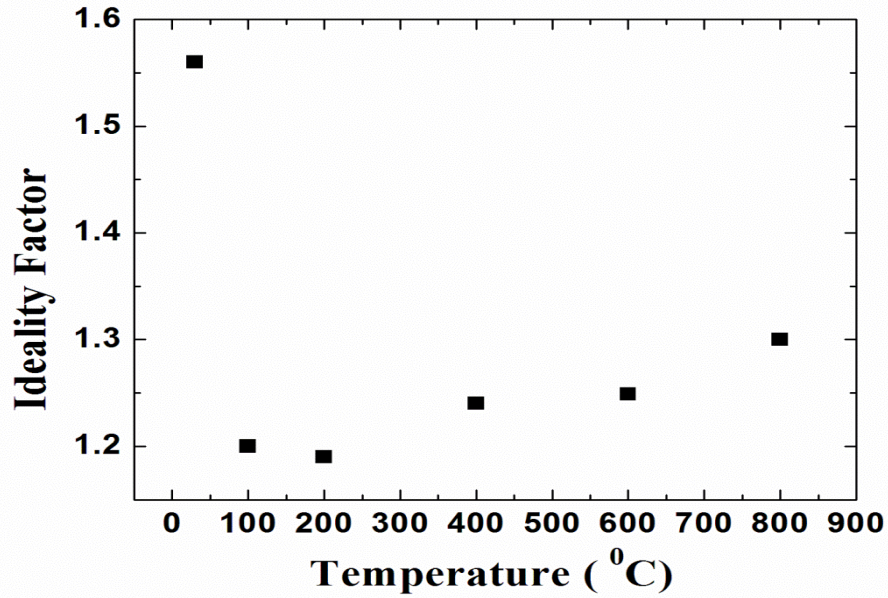


Figure 6.7. Variation of ideality factors with isochronal annealing of 50 μm thick n-type 4H-SiC Schottky barrier device.

Figure 6.8 shows C-V plots of the Schottky barrier after annealing at different temperatures. The capacitance of the fabricated Schottky barrier is decreased after annealing at 100 $^{\circ}\text{C}$ and then again increased with annealing at higher temperatures [120].

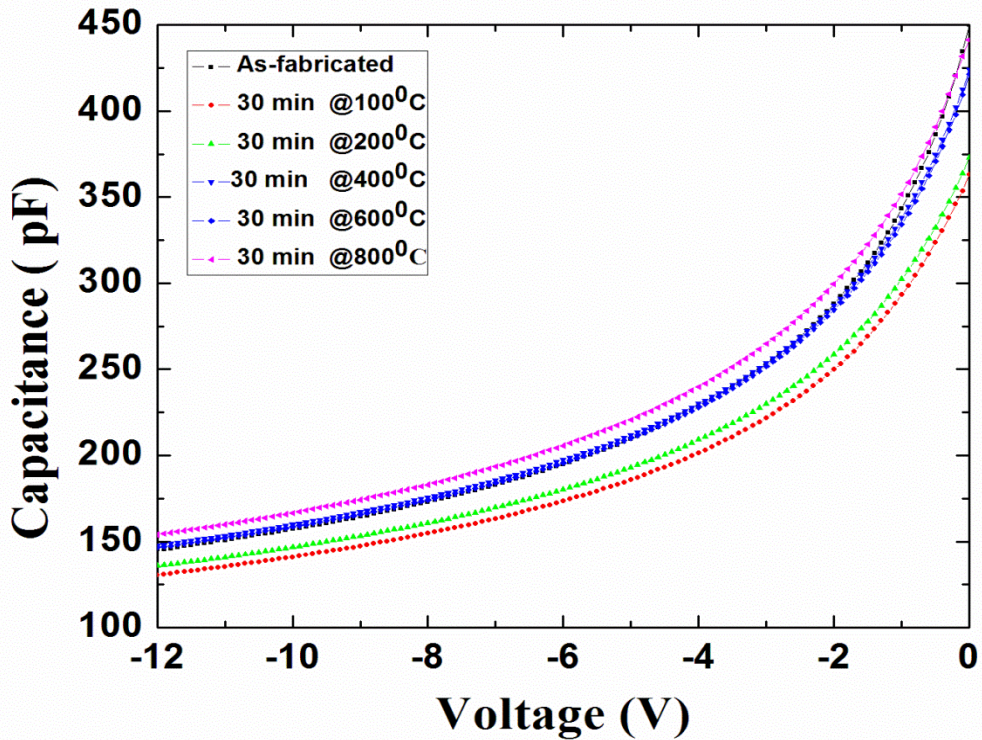


Figure 6.8. Capacitance vs voltage of the as-fabricated 50 μm thick n-type 4H-SiC Schottky barrier and after isochronal annealing at different temperatures.

6.4.2 DLTS Spectra and Arrhenius Plots after Annealing

After each isochronal annealing of the SiC sample at a particular temperature, a DLTS thermal scan was carried for different rate windows. A DLTS scan with a particular rate window of the annealed sample are plotted together to investigate the effect of isochronal annealing. Figure 6.9 (a) shows the DLTS spectra (for the rate window 5 ms) of fabricated Schottky barrier diodes before and after annealing at 100 $^{\circ}\text{C}$ and 200 $^{\circ}\text{C}$ respectively. Figure 6.9 (b) shows the spectra (for the rate window 5 ms) after

annealing at 400 °C, 600 °C, and 800 °C respectively for the temperature scan 80 K - 140 K [120]. The spectra are separated in two figures for clarity.

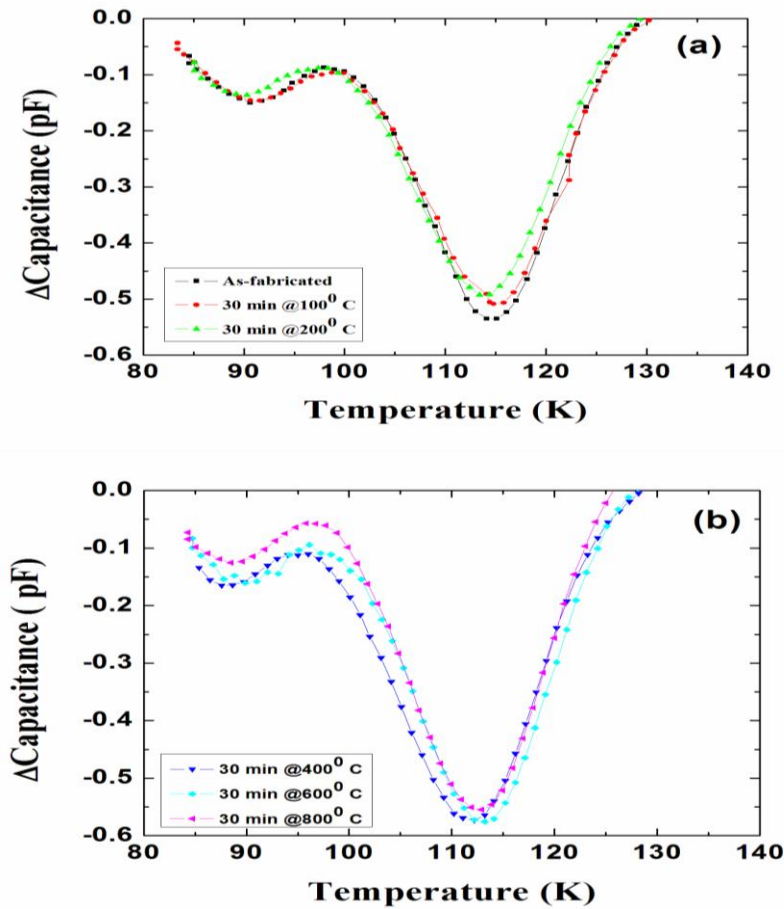


Figure 6.9. DLTS spectra obtained using the 50 μ m thick n-type Ni/4H-SiC epitaxial Schottky barrier in a temperature range 80 K - 140 K: (a) as-fabricated, annealed at 100 °C and 200 °C; and (b) annealed at 400 °C, 600 °C, and 800 °C respectively.

The small peak that appears at around 85 K did not appear for all rate windows. From the spectra in Figure 6.9, it is obvious that the activation energy and defect density related to this peak is very small and almost near to the detection limit of the DLTS measurement system. For better determination of the defect signature, DLTS spectra has to be run in a much lower temperature around 50 K. However, due to the small activation

energy and very low density of the defect, it is expected that this defect will have negligible effects on the device performance. For the more prominent DLTS peak that appears in the temperature scan 80 K - 140 K is at 0.16 eV below the conduction band minima which is termed as peak #1 in our study.

The DLTS spectra (for the rate window 5 ms) in the temperature scan 250 K - 800 K of the as-fabricated and after annealing are shown in Figure 6.10 (a) and (b) [120]. These spectra showed the annealing behavior of the defects $Z_{1/2}$ (peak #2, $E_c - 0.67\text{eV}$) at around 300 K, EH_5 (peak #3, $E_c - 1.03\text{ eV}$) at around 500 K, and $\text{EH}_{6/7}$ (peak #4, $E_c - 1.6\text{ eV}$) at around 650 K. Annealing impact on DLTS peaks corresponding to different defects that were detected at higher temperatures are depicted in Figure 6.10.

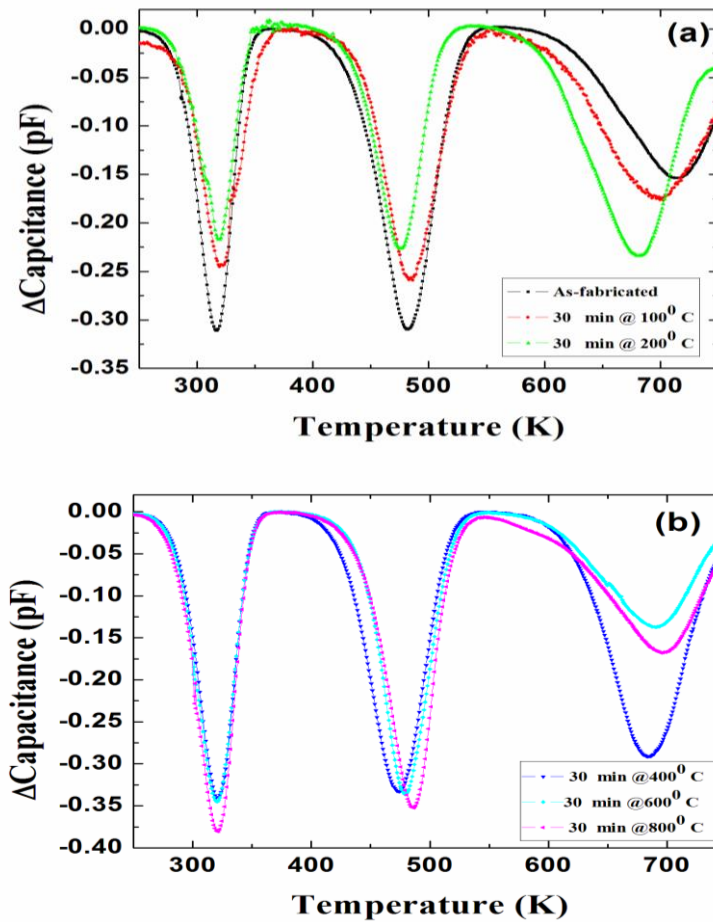


Figure 6.10. DLTS spectra obtained in a temperature range 250 K - 750 K: (a) as-fabricated and annealed at 100 °C and 200 °C; and (b) annealed at 400 °C, 600 °C, and 800 °C.

After isochronal annealing at different temperatures, an Arrhenius plot was drawn from the peak temperatures in the DLTS spectra of the annealed sample. The defects parameters for every individual defects are calculated from these Arrhenius plot. The Arrhenius plot drawn after annealing at temperature 100 °C, 200 °C, 400 °C, 600 °C and 800 °C are shown in Figure 6.11, Figure 6.12, Figure 6.13, Figure 6.14, and Figure 6.15 respectively. The calculated defects parameters after annealing at temperatures 100 °C,

200 °C, 400 °C, 600 °C, and 800 °C are shown in Table 6.2, Table 6.3, Table 6.4, Table 6.5, and Table 6.6 respectively.

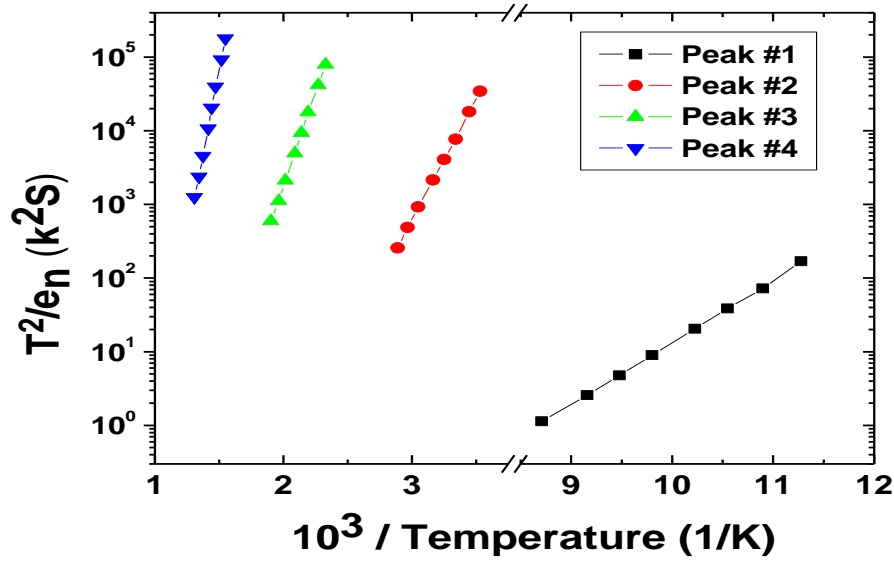


Figure 6.11. Arrhenius plot corresponding to the DLTS spectra obtained after annealing at 100 °C.

Table 6.2. Defect parameters obtained after annealing at 100 °C

Peak #	σ_n cm^2	ΔE eV	N_t cm^{-3}	Possible Trap Identity
Peak 1	3.32×10^{-15}	$E_c - 0.17$	1.13×10^{13}	Ti(c)
Peak 2	2.09×10^{-15}	$E_c - 0.65$	6.38×10^{12}	$Z_{1/2}$
Peak 3	1.61×10^{-15}	$E_c - 1.00$	6.49×10^{12}	EH_5
Peak 4	3.23×10^{-15}	$E_c - 1.70$	6.38×10^{12}	$\text{EH}_{6/7}$

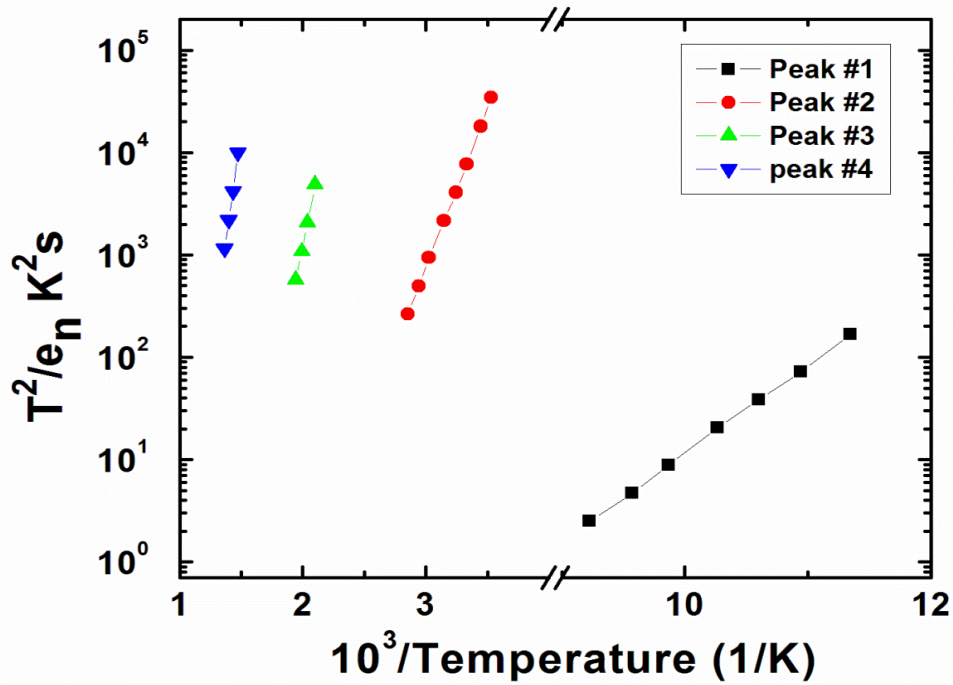


Figure 6.12. Arrhenius plots corresponding to the DLTS spectra obtained after annealing at 200 °C.

Table 6.3. Defect parameters after annealing at 200 °C

Peak #	σ_n cm^2	ΔE eV	N_t cm^{-3}	Possible Trap Identity
Peak 1	2.18×10^{-15}	$E_c - 0.17$	1.04×10^{13}	Ti (c)
Peak 2	4.27×10^{-16}	$E_c - 0.61$	5.58×10^{12}	$Z_{1/2}$
Peak 3	9.1×10^{-16}	$E_c - 1.14$	5.71×10^{12}	EH ₅
Peak 4	6.66×10^{-14}	$E_c - 1.69$	5.59×10^{12}	EH _{6/7}

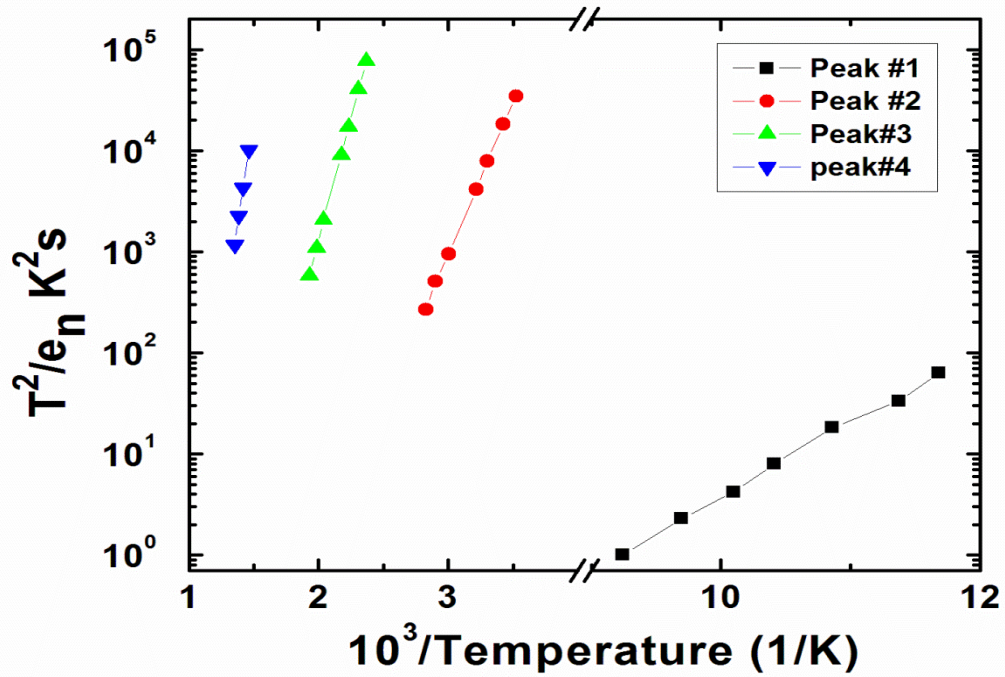


Figure 6.13. Arrhenius plots corresponding to the DLTS spectra obtained after annealing at 400 °C

Table 6.4. Defect parameters after annealing at 400 °C

Peak #	σ_n cm^2	ΔE eV	N_t cm^{-3}	Possible Trap Identity
Peak 1	9.63×10^{-16}	$E_c - 0.15$	1.17×10^{13}	Ti(c)
Peak 2	2.01×10^{-16}	$E_c - 0.60$	7.19×10^{12}	$Z_{1/2}$
Peak 3	6.02×10^{-16}	$E_c - 0.96$	7.01×10^{12}	EH_5
Peak 4	6.46×10^{-14}	$E_c - 1.71$	7.44×10^{12}	$\text{EH}_{6/7}$

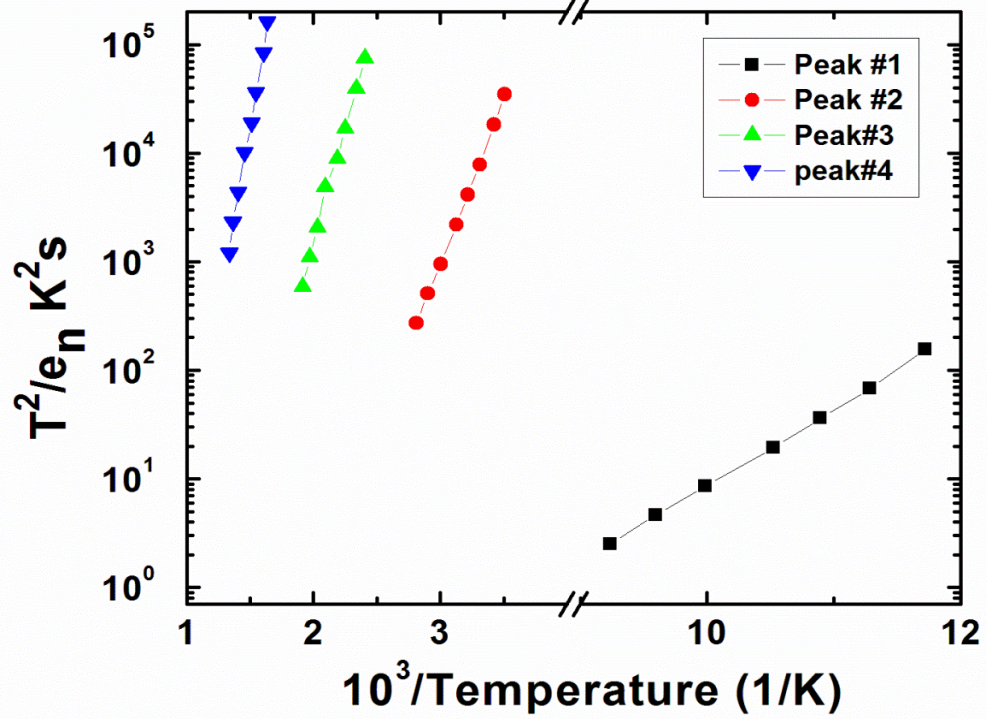


Figure 6.14. Arrhenius plots corresponding to the DLTS spectra obtained after annealing at 600 °C.

Table 6.5. Defect parameters after annealing at 600 °C

Peak #	σ_n cm^2	ΔE eV	N_t cm^{-3}	Possible Trap Identity
Peak 1	6.7×10^{-16}	$E_c - 0.14$	1.23×10^{13}	Ti(c)
Peak 2	1.58×10^{-16}	$E_c - 0.60$	8.06×10^{12}	$Z_{1/2}$
Peak 3	3.71×10^{-16}	$E_c - 0.85$	8.23×10^{12}	EH_5
Peak 4	1.43×10^{-14}	$E_c - 1.34$	3.32×10^{12}	$\text{EH}_{6/7}$

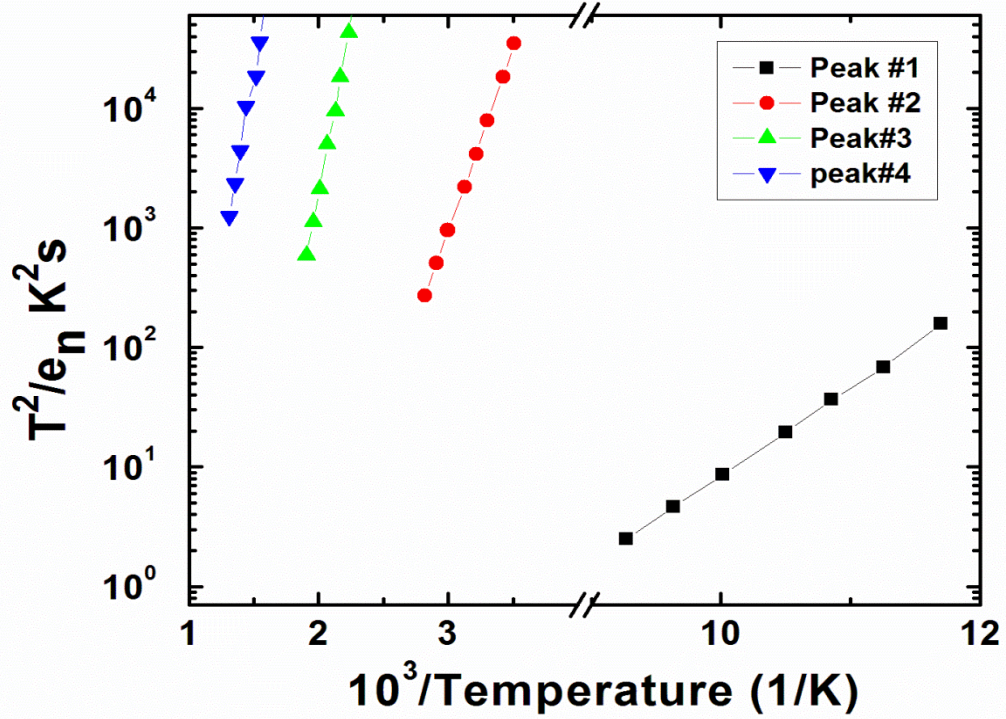


Figure 6.15. Arrhenius plot corresponding to the DLTS spectra obtained after annealing at 800 °C

Table 6.6. Defect parameters after obtained annealing 800 °C

Peak #	σ_n cm^2	ΔE eV	N_t cm^{-3}	Possible Trap Identity
Peak 1	6.28×10^{-16}	$E_c - 0.15$	1.45×10^{13}	Ti(c)
Peak 2	2.28×10^{-16}	$E_c - 0.60$	1.00×10^{13}	$Z_{1/2}$
Peak 3	3.72×10^{-16}	$E_c - 1.14$	9.56×10^{12}	EH ₅
Peak 4	2.23×10^{-17}	$E_c - 1.245$	6.14×10^{12}	EH _{6/7}

6.4.3 Analysis of the Impact of Annealing on Defects Parameters

To observe the effect of annealing, the defect parameters (capture cross section and density) variation with annealing temperature are plotted for every individual defects. For the peak # 1 which identified as Ti (c), the activation energy after annealing at different temperatures up to 800 °C lies within $E_c - 0.16 \pm 0.015$ eV which means the nature of the defect did not change much with annealing. The capture cross section and defect density related to peak #1 are shown in Figure 6.16 (a) and Figure 6.16 (b), respectively. The capture cross-section of the defect Ti (c) decreased up to the annealing temperature of 400 °C and remains unchanged for the annealing at higher temperatures. On the other hand the defect density decreased with the annealing temperature up to 200 °C and again increased gradually with the annealing temperature of 800 °C, which is the extent of our present studies.

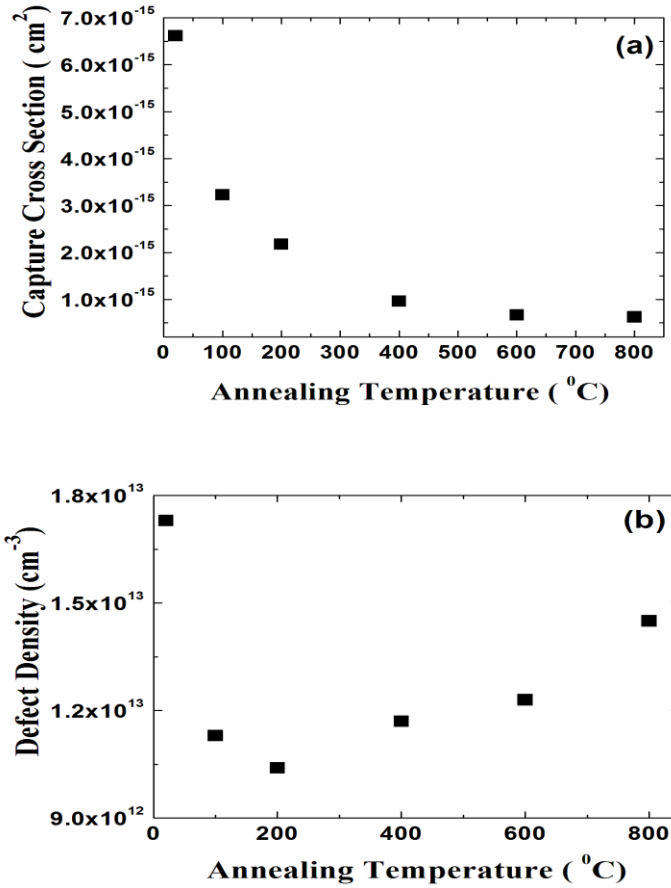


Figure 6.16. Defect ($E_c - 0.17$ eV corresponding to peak #1) parameters variation with annealing temperature: (a) capture cross-section, and (b) defect density.

Defect parameters variation of most prominent defect $Z_{1/2}$ of 4H-SiC is located at $E_c - 0.67$ eV is shown in Figure 6.17 [120]. The capture cross-section is decreased by almost an order of magnitude through annealing up to 200 °C and remains unchanged till 800 °C. The defect density increased with the increase of annealing temperature after showing an initial small decrease up to 200 °C. This small decrease may be due to migration or out-diffusion of carbon interstitial C_i . After 200 °C, dopant nitrogen atoms occupy the position of carbon atom which produces C_i resulting in an increase of $Z_{1/2}$. Eberlein *et al.* [121] has shown that the formation of $Z_{1/2}$ is possible through the

participation of C_i with nitrogen. This has also been supported experimentally by Kimoto *et al.* [122] on CVD grown 4H-SiC and by Eberlein *et al.* [121] through theoretical modeling. However the variation of density is less than an order of magnitude and shows a tendency of stability through the isochronal annealing up to 800 °C. This stability is reasonable for a defect of $Z_{1/2}$ type which is an intrinsic growth defect and can be increased substantially by irradiation. The observation is consistent with the fact that $Z_{1/2}$ has a high thermal stability since the growth temperature used in CVD is typically ~ 1600 °C [123].

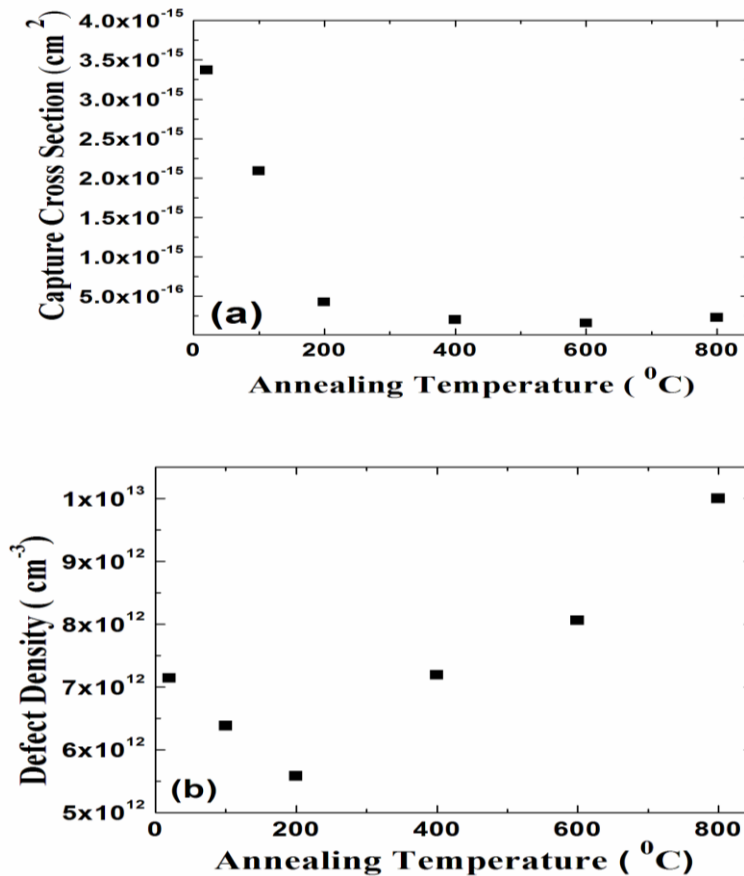


Figure 6.17. Defect $Z_{1/2}$ (corresponding to peak #2, $E_c - 0.67$ eV) parameters variation with annealing temperature: (a) capture cross-section, and (b) defect density.

The variation of capture cross-section and defect density of EH_5 is shown in Figure 6.18. The capture cross-section of the defect is decreased slightly and remains unchanged throughout our annealing study. Annealing impact on the defect density of EH_5 showed a decrease up to 200 °C and increases with annealing temperature. Negoro et al. [124] identified a similar defect at 0.95 ± 0.05 eV as $RD_{1/2}$ and showed that the defect density increases slightly with the increase of annealing temperature. On the other hand, Alfieri et al. [123] showed that the defect density located at $E_c - 1.03$ eV is slightly decreased with the annealing up to the temperature 600 °C and the defect density goes below the detection limit after annealing at 1300 °C. In our studies we found similar annealing response of defect density for $Z_{1/2}$ and EH_5 . This is due to the same origin of formation of these two defects related to the displacement of carbon from the lattice structure. $Z_{1/2}$ is thought to be formed due to carbon interstitials, and EH_5 is thought to be formed due to carbon clustering. Hemmingsson et al. [95] observed EH_5 defect in the samples with a 2.5 MeV electron irradiation for doses higher than 10^{14} cm⁻². But Storasta et al. [104] did not see this defect when the samples were exposed in low energy irradiation (250 keV) which is close to the threshold for atomic displacement of carbon. This also suggests EH_5 is related to carbon cluster defects.

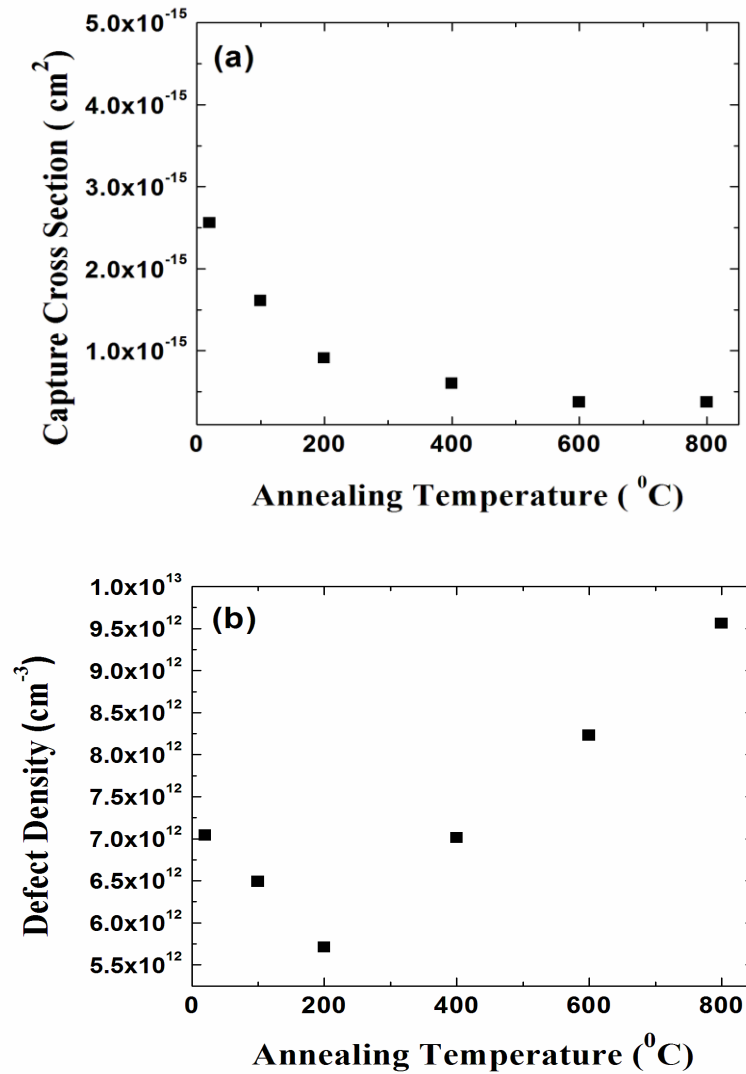


Figure 6.18. Defect EH₅ (corresponding to peak #3, E_c - 1.03 eV) parameters variation with annealing temperature: (a) capture cross-section, and (b) defect density.

In our studies the variation of capture cross-sections and densities of EH_{6/7} defect with isochronal annealing do not follow any trend as shown in Figure 6.19. Though the variation of defects parameters is random but the range of variation is very small, which suggests the defect is very stable up to a temperature of 800 °C. Several groups have shown that the defect EH_{6/7} is very stable up to a temperature of 1000 °C [123, 124, 105].

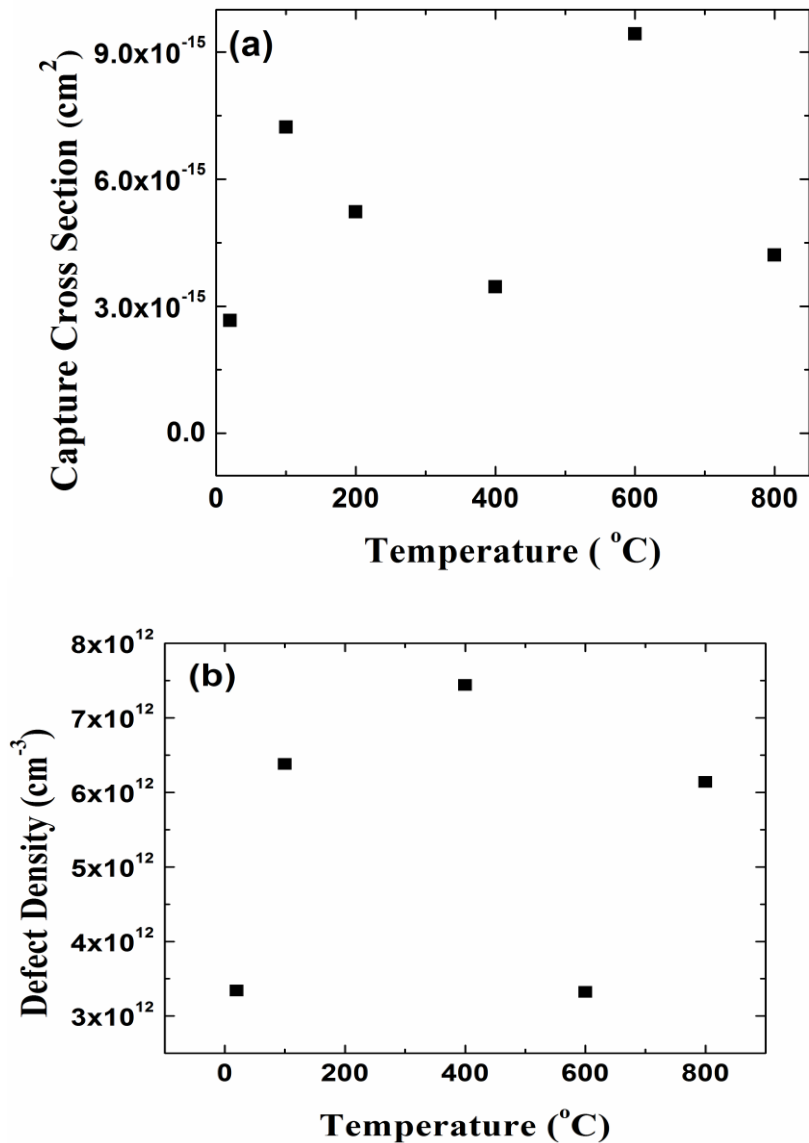


Figure 6.19. Defect EH_{6/7} (corresponding to peak #4, E_c - 1.6 eV) parameters variation with annealing temperature: (a) capture cross-section, and (b) defect density.

6.5 CONCLUSION

Isochronal annealing studies are carried out in the temperature range from 100 °C to 800 °C on 50 μm n-type 4H-SiC epitaxial layers. Defect levels have been investigated and characterized thoroughly on as-fabricated and isochronal annealed Schottky diodes

through deep level transient spectroscopy. Four different defect levels located at $E_c - 0.17$ eV, $E_c - 0.67$ eV, $E_c - 1.03$ eV, and $E_c - 1.6$ eV are identified as Ti (c), $Z_{1/2}$, EH_5 , and $EH_{6/7}$, respectively. The capture cross-section of the shallow defect level $E_c - 0.17$ eV for Ti (c) was reduced with increasing annealing temperature while the defect density was not changed significantly. Similar annealing behavior of $Z_{1/2}$ and EH_5 were correlated very well with these defect levels having the same origin of formation. $Z_{1/2}$ is related to carbon interstitial, and EH_5 is related to carbon cluster. The defect parameters of $EH_{6/7}$ changed randomly within a small range up to the upper annealing temperature range of 800 °C. The most common two intrinsic deep level defects $Z_{1/2}$ and $EH_{6/7}$ were found to be stable up to the limit of our experiment of 800 °C.

CHAPTER 7: CONCLUSION AND SUGGESTIONS FOR FUTURE WORK

7.1 CONCLUSION

This dissertation is focused on the investigation the deep level defects of 4H-SiC epitaxial layers. A comprehensive study on the fabrication and characterization of 4H-SiC radiation detector has been performed. The characterization techniques are based on electrical measurements which include current - voltage and capacitance - voltage studies to know electrical behavior of the devices, spectroscopic measurements to see the alpha response, DLTS measurements to detect deep level defects, and isochronal annealing to observe the impact of annealing on defects.

Radiation detectors based on Schottky diodes are fabricated on high quality 20 μm and 50 μm thick n-type 4H-SiC epitaxial layers. The epitaxial layers were grown by chemical vapor deposition on 4H-SiC (0001) n-type substrates. The properties of the fabricated Schottky barriers are determined by current-voltage (I-V) and capacitance-voltage (C-V) measurements. The high barrier height (of the order of 1.6 eV, was calculated by using a thermionic emission model) of the Schottky devices offered very low leakage current (of the order of few pA) at the reverse bias of \sim -100 V. Due to this good Schottky behavior and low leakage current, the fabricated detectors are found to be

very suitable for radiation detectors. Alpha spectroscopic measurements of the fabricated detectors are performed by using a ^{241}Am radiation source and the percentage energy resolution of the detectors was found to be in the range of 0.29 % - 1.8 % for 5486 keV alpha particle peak.

Deep level transient spectroscopy (DLTS) studies were conducted in the temperature range of 80 K - 800 K to investigate the deep level defects. Types of identified defects and defect parameters are varied widely from the detector to detector. In all of the detectors fabricated on 20 μm thick epitaxial layers, deep level defects $Z_{1/2}$ located at $E_c - 0.6$ eV, Ci1 located at $E_c - 1.3$ eV, and $\text{EH}_{6/7}$ located at $E_c - 1.6$ eV are found by the DLTS measurements. Among them two defect levels (electron traps) $Z_{1/2}$ and $\text{EH}_{6/7}$ which are related to carbon vacancies and their complexes mostly affected the detector resolution. Defect level observed at $E_c - 1.3$ eV is found not to affect the detectors performance. For the case of 50 μm epitaxial layer the detected defects are identified as $\text{Ti}(\text{c})$ at $E_c - 0.13$ eV, $\text{Ti}(\text{c})$ at $E_c - 0.17$ eV, $Z_{1/2}$ at $E_c - 0.67$ eV, EH_5 at $E_c - 1.04$ eV, Ci1 at $E_c - 1.3$ eV, and a newly detected deep level at $E_c - 2.4$ eV. Deep level defect located at $E_c - 2.4$ eV is identified for the first time. Along with $Z_{1/2}$ and EH_5 , the newly identified defect at $E_c - 2.4$ eV mostly affected the detector resolution fabricated on 50 μm 4H-SiC epitaxial layers.

To investigate the annealing behavior of deep level defects, isochronal annealing studies were carried out in the temperature range 100 °C to 800 °C on 50 μm n-type 4H-SiC epitaxial layers. Four different defects $\text{Ti}(\text{c})$ located at $E_c - 0.17$ eV, $Z_{1/2}$ located at E_c

- 0.67 eV, EH_5 located at $E_c - 1.03$ eV, and $EH_{6/7}$ located at $E_c - 1.6$ eV are responded differently to the annealing studies. Capture cross sections and densities of every individual defects are plotted to see the impact of annealing. The capture cross-section of the shallow defect level $E_c - 0.17$ eV for Ti (c) was reduced with increasing annealing temperature while the defect density was not changed significantly. Similar annealing behavior of $Z_{1/2}$ and EH_5 were correlated very well with the understanding of these defect levels having the same origin of formation. $Z_{1/2}$ is related to carbon interstitial, and EH_5 is related to carbon cluster. The defect parameters of $EH_{6/7}$ changed randomly within a small range up to the upper annealing temperature range of 800 °C in this study. The most common two intrinsic deep level defects $Z_{1/2}$ and $EH_{6/7}$ were found to be stable up to the limit of our experiment of 800 °C.

7.2 FUTURE WORK

Due to high band-gap and good crystallinity, 4H-SiC epitaxial layer is an excellent material for fabrication of alpha particle detectors. The resolutions of Schottky barrier based detectors are found to be limited by the deep level defects present within the 4H-SiC epitaxial layers. To improve the detector performance and minimize the defects' role, the following suggestions for future research work have emerged from the present investigations:

- ❑ Surface passivation prior to detector fabrication can be applied to improve the radiation detector performance. It is likely that both the reverse

leakage current and energy resolution can be improved by eliminating surface and interface states through passivation. Dielectric layer grown by PECVD or MOCVD such as silicon dioxide (SiO_2), silicon nitride (Si_3N_4), and Si-O-N are the most suitable materials for passivation.

- ❑ In this work nickel is used for Schottky barrier fabrication. Detector fabrication with high work function metals such as ruthenium, palladium, and platinum may improve the Schottky barrier properties. It is expected that these high work function metals will reduce the leakage current and will minimize the deep level effects to hence improve the detector performance.
- ❑ After delineating the microscopic defects on the epitaxial layers, the Schottky barrier based devices can be fabricated on different location on the epitaxial surfaces. Correlation of the deep level defects with microscopic defects can be carried out through DLTS measurements on the Schottky devices fabricated in the region with microscopic defect and in the defect free region.
- ❑ Various thicknesses (other than 20 μm and 50 μm) of 4H-SiC epitaxial layers can be used to fabricate the Schottky barrier to see the improvement on detector resolution. DLTS measurements can be used to investigate the

deep centers in different thick epitaxial layers and the impact of deep centers on the high energy detector performance.

- Detailed theoretical studies by DFT (Density Functional Theory) and ab-initio calculations may be interesting to investigate the microstructure of newly identified deep level defects located far below from the conduction band ($E_c - 2.4$ eV).

REFERENCES

- [1] S. T. Pantelides, "The electronic structure of impurities and other point defects in semiconductors," *Review of Modern Physics*, vol. 50, no. 4, pp. 797-858, 1978.
- [2] K. C. Mandal, S. K. Chaudhuri, K. V. Nguyen and M. A. Mannan, "Correlation of Deep Levels With Detector Performance in 4H-SiC Epitaxial Schottky Barrier Alpha Detectors," *IEEE Transaction on Nuclear Science*, vol. 61, no. 4, pp. 2338-2344, 2014.
- [3] A. Rohatgi, R. H. Hopkins, J. R. Davis, R. B. Cambell and H. C. Mollenkopf, "The impact of molybdenum on silicon and silicon solar cell performance," *Solid State Electronics*, vol. 23, no. 11, pp. 1185-1190, 1981.
- [4] M. Jaros and S. Brand, "Localized defects in III-V semiconductors," *Physical Review B*, vol. 14, no. 10, pp. 4494-4505, 1976.
- [5] G. A. Baraff, E. O. Kane and M. Schluter, "Silicon Vacancy: A Possible "Anderson Negative-U" System," *Physical Review Letters*, vol. 43, no. 13, pp. 956-959, 1979.
- [6] E. O. Kane and M. Schluter, "Charge disturbances around neutral defects: A simple new method applied to the ideal silicon vacancy," *Physical Review B*, vol. 19, no. 10, pp. 5232-5239, 1979.
- [7] T. Shimizu and K. Minami, "LCAO MO treatment for the S+ donor in Si," *Physica Status Solidi (b)*, vol. 48, no. 2, pp. K181-K184, 1971.
- [8] I. Gorczyca, A. Svane and N. E. Christensen, "Theoretical study of point defects in GaN and AlN; lattice relaxations and pressure effects," *MRS Internet Journal of Nitride Semiconductor Research*, vol. 2, p. e18, 1997.
- [9] R. Williams, "Criterion for Continuous Amplitude Oscillations of Optical Masers," *Journal of Applied Physics*, vol. 37, no. 9, pp. 3411-3412, 1966.
- [10] L. Forbes and C. T. Sah, "On the determination of deep level center energy and concentration by thermally stimulated conductivity measurements using reverse-biased p-n junctions," *Solid-State Electronics*, vol. 14, no. 2, pp. 182-183, 1971.
- [11] C. T. Sah, W. Chan, H. Fu and J. W. Walker, "Thermally Stimulated Capacitance (TSCAP) in p-n Junctions," *Applied Physics Letters*, vol. 20, no. 5, pp. 193-195, 1972.
- [12] C. T. Sah, L. Forbes, L. L. Rosier and A. F. Tasch, "Thermal and optical emission and capture rates and cross sections of electrons and holes at imperfection centers in semiconductors from photo and dark junction current and capacitance experiments," *Solid State Electronics*, vol. 13, no. 6, pp. 759-788, 1970.
- [13] C. T. Sah, "Bulk and interface imperfections in semiconductors," *Solid State Electronics*, vol. 19, no. 12, pp. 975-990, 1976.
- [14] D. V. Lang, "Deep-level transient spectroscopy: A new method to characterize

- traps in semiconductors," *Journal of Applied Physics*, vol. 45, no. 7, pp. 3023-3032, 1974.
- [15] J. K. Rhee and T. Ikoma, "Photoinduced current transient spectroscopy of semi-insulating InP:Fe and InP:Cr," *Journal of Applied Physics*, vol. 53, no. 6, pp. 4247-4249, 1982.
- [16] R. E. Kremer, M. Arikian, J. C. Abele and J. Blakemore, "Transient photoconductivity measurements in semi-insulating GaAs. I. An analog approach," *Journal of Applied Physics*, vol. 62, no. 6, pp. 2424-2431, 1987.
- [17] J. A. PALS, "Properties of Au, Pt, Pd and Rh levels in silicon measured with a constant capacitance technique," *Solid State Electronics*, vol. 17, no. 11, pp. 1139-1145, 1974.
- [18] INSPEC, Properties of Gallium Arsenide, London: The Institution of Electrical Engineers, 1986.
- [19] Z. Q. Fang, D. C. Look, W. Kim, Z. Fan, A. Botchkarev and H. Morkoc, "Deep centers in n-GaN grown by reactive molecular beam epitaxy," *Applied Physics Letters*, vol. 72, no. 18, pp. 2277-2279, 1998.
- [20] Z. Q. Fang, D. C. Look, J. Jasinski, M. Benamara, Z. Liliental-Weber and R. J. Molnar, "Evolution of deep centers in GaN grown by hydride vapor phase epitaxy," *Applied Physics Letters*, vol. 78, no. 3, pp. 332-334, 2001.
- [21] F. Riedel and W. Schroter, "Electrical and structural properties of nanoscale NiSi₂ precipitates in silicon," *Physical Review B*, vol. 62, no. 11, pp. 7150-7156, 2000.
- [22] S. Das, S. K. Chaudhuri, R. N. Bhattacharya and K. C. Mandal, "Defect levels in Cu₂ZnSn(S_xSe_{1-x})₄ solar cells probed by current-mode deep level transient spectroscopy," *Applied Physics Letters*, vol. 104, no. 19, pp. 192106(1-4), 2014.
- [23] M. Igalson, P. Zabierowski, A. Romeo and L. Stolt, "Reverse -bias DLTS for investigation of the interface region of thin film solar cells," *Opto-Electronics Review*, vol. 8, no. 4, p. 346-349, 2000.
- [24] S. F. Yoon, K. H. Yip, H. Q. Zheng and B. P. Gay, "Effect of deep levels on the characteristics of InGa_{1-x}P/In_{0.20}Ga_{0.80}As/GaAs high-electron mobility transistor grown by solid-source MBE," *Journal of Crystal Growth*, vol. 217, no. 1-2, pp. 33-39, 2000.
- [25] V. W. Ilchenko, S. D. Lin, C. P. Lee and O. V. Tretyak, "Deep level transient spectroscopy characterization of InAs self-assembled quantum dots," *Journal of Applied Physics*, vol. 89, no. 2, pp. 1172-1174, 2001.
- [26] R. Magno, B. R. Bennett and E. R. Glaser, "Deep level transient capacitance measurements of GaSb self-assembled quantum dots," *Journal of Applied Physics*, vol. 88, no. 10, pp. 5843-5849, 2000.
- [27] J. J. Berzelius, "Untersuchungen über die Flusspathsäure und deren merkwürdigsten Verbindungen," *Annalen der Physik*, vol. 77, no. 6, pp. 169-230, 1824.
- [28] L. S. Ramsdell, "Studies on silicon carbide," *American Mineralogist*, vol. 32, pp. 64-82, 1947.
- [29] T. Kinoshita, K. M. Itoh, J. Muto, M. Schadt, G. Pensl and K. Takeda, "Calculation

- of the Anisotropy of the Hall Mobility in N-type 4H- and 6H-SiC," *Material Science Forum*, vol. 264–268, pp. 295-298, 1998.
- [30] W. J. Choyke, H. Matsunami and G. Pensi, *Silicon Carbide: A Review of Fundamental Questions and Applications to Current Device Technology*, Berlin: Wiley-VCH, 1997.
- [31] G. L. Harris, *Properties of SiC*, London: INSPEC, 1995.
- [32] B. Ellis and T. S. Moss, "The Conduction bands in 6H and 15R silicon carbide, Hall effect and infrared Faraday rotation measurements," in *Proceeding of the Royal Society of London*, London, 1967.
- [33] G. A. Lomakina, "Silicon carbide Proceeding," in *3 rd International Conference on Silicon Carbide*, Miami, 1973.
- [34] S. Karmann, W. Suttrop, A. Schoner, M. Schadt, C. Haberstroh, F. Engebrecht, R. Helbig, G. Penal, R. A. Stein and S. Leibenzeder, "Chemical vapor deposition and characterization of undoped and nitrogen-doped single crystalline 6H-SiC," *Journal of Applied Physics*, vol. 72, no. 11, pp. 5437-5442, 1992.
- [35] F. Nava, G. Bertuccio, A. Cavallini and E. Vittone, "Silicon carbide and its use as a radiation detector material," *Measurement Science and Technology*, vol. 19, pp. 102001(1-25), 2008.
- [36] Y. M. Tairov and V. F. Tsvetkov, "General principles of growing large-size single crystals of various silicon carbide polytypes," *Journal of Crystal Growth*, vol. 52, no. 1, pp. 146-150, 1981.
- [37] S. G. Muller, R. C. Glass, H. M. Hobgood, V. F. Tsvetkov, M. Brady, D. Henshall, J. R. Jenny, D. Malta and C. H. Carter, "The status of SiC bulk growth from an industrial point of view," *Journal of Crystal Growth*, vol. 211, no. 1-4, pp. 325-332, 2000.
- [38] J. J. Sumakeris, J. R. Jenny and A. R. Powell, "Bulk crystal growth, epitaxy, and defect reduction in silicon carbide materials for microwave and power devices," *MRS Bulletin*, vol. 30, no. 4, pp. 280-286, 2005.
- [39] CREE, "Cree Silicon Carbide Substrates and Epitaxy," CREE, March 2015. [Online]. Available: <http://www.cree.com/LED-Chips-and-Materials/Materials>.
- [40] S. V. Rendakova, I. P. Nikitina, A. S. Tregubova and V. A. Dmitriev, "Micropipes and dislocation density reduction in 6H-SiC and 4H-SiC Structure grown by liquid phase epitaxy," *Journal of Electronic Materials*, vol. 27, pp. 292-295, 1998.
- [41] A. R. Powell and L. B. Rowland, "SiC materials - Progress, status, and potential roadblocks," *Proceedings of the IEEE*, vol. 90, no. 6, pp. 942-955, 2002.
- [42] O. Kordina, C. Hallin, A. Henry, J. P. Bergman, I. G. Ivanov, A. Ellison, N. T. Son and E. Janzen, "Growth of SiC by Hot-Wall CVD and HTCVD," *Physica Status Solidi (b)*, vol. 202, pp. 321-334, 1997.
- [43] A. Owens and A. Peacock, "Compound semiconductor radiation detectors," *Nuclear Instruments and Methods in Physics Research Section A: Accelerators, Spectrometers, Detectors and Associated Equipment*, vol. 531, no. 1-2, pp. 18-37, 2004.
- [44] P. Blood and J. W. Orton, "The Electrical Characterization of Semiconductors:

- Majority Carriers and Electron States," in *Techniques of Physics*, San Diego, 1992.
- [45] S. M. Sze and K. K. Ng, *Physics of Semiconductor devices*, New Jersey: John Wiley & Sons, 2007.
- [46] E. H. Rhoderick and R. H. Williams, *Metal-Semiconductor Contacts*, New York: Clarendon Press. Oxford, 1988.
- [47] S. S. Li, *Semiconductor Physical Electronics*, New York: Springer, 2006.
- [48] H. A. Bethe, "Theory of the Boundary Layer of Crystal Rectifiers," MIT Radiation . Laboratory, Boston, 1942.
- [49] D. K. Schroder, *Semiconductor Material and Device Characterization*, New York: John Wiley & Sons, 1998.
- [50] R. T. Tung, "Electron transport at metal-semiconductor interfaces: General theory," *Physical Review B*, vol. 45, no. 23, pp. 13509-13523, 1992.
- [51] P. G. Muzykov, R. M. Krishna and K. C. Mandal, "Temperature dependence of current conduction in semi-insulating 4H-SiC epitaxial layer," *Applied Physics Letters*, vol. 100, no. 3, pp. 032101(1-4), 2012.
- [52] D. A. Neamen, *Semiconductor Physics andz Devices, Basic Principle*, McGraw-Hill, 2012.
- [53] A. Hallen and M. Bakowski, "The influence of ion flux on defect production in MeV proton-irradiated silicon," *Solid-State Electronics*, vol. 32, no. 11, pp. 1033-1037, 1989.
- [54] F. D. Auret and P. N. K. Deenapanray, "Deep Level Transient Spectroscopy of Defects in HighEnergy Light-Particle Irradiated Si," *Critical Review in Solid State and Materials Sciences*, vol. 29, no. 1, pp. 1-44, 2004.
- [55] J. A. Powell and D. J. Larkin, "Process-Induced Morphological Defects in Epitaxial CVD Silicon Carbide," *Physics Status Solidi (b)*, vol. 202, no. 1, pp. 529-548, 1997.
- [56] T. Kimoto, N. Miyamoto and H. Matsunami, "Performance Limiting Surface Defects in SiC Epitaxial p-n Junction Diodes," *IEEE Transaction on Electron Devices*, vol. 46, no. 3, pp. 471-477, 1999.
- [57] Cree Incorporated, "SiC data Sheets," Cree Research Incorporation, Durham, NC, 1999.
- [58] T. Kuhr, E. Sanchez, M. Skowronski, W. Vetter and M. Dudley, "Hexagonal voids and the formation of micropipes during SiC sublimation growth," *Journal of Applied Physics*, vol. 89, no. 8, pp. 4625-4630, 2001.
- [59] E. Sanchez, S. Ha, J. Grim, M. Skowronski, W. Vetter, M. Dudley, R. Bertke and W. Mitchel, "Assessment of Polishing-Related Surface Damage in Silicon Carbide," *Journal of Electrochemical Society*, vol. 149, no. 2, pp. G131-G136, 2002.
- [60] P. G. Neudeck and J. A. Powell, "Performance limiting micropipe defects in silicon carbide wafers," *IEEE Electron Devices Letters*, vol. 15, no. 2, pp. 63-65, 1994.
- [61] U. Zimmermann, A. Hallen, A.O.Konstantinov and B. Breitholtz, "Investigations of microplasma breakdown in 4H silicon carbide," in *Materials Research Society Symposium Proceeding*, San Francisco, California, 1998.

- [62] M. Dudley, S. Wang, W. Huang, C. H. Carter, V. F. Tsvetkov and C. Fazi, "White-beam synchrotron topographic studies of defects in 6H-SiC single crystals," *Journal of Physics D: Applied Physics*, vol. 28, no. 4A, pp. A63-A68, 1995.
- [63] P. G. Neudeck, "Electrical Impact of SiC Structural Defects on High Electric Field Devices," *Materials Science Forum*, Vols. 338-342, pp. 1161-1166, 2000.
- [64] P. G. Neudeck, W. Huang and M. Dudley, "Study of Bulk and Elementary Screw Dislocation Assisted Reverse Breakdown in Low-Voltage (< 250 V) 4H-SiC p+ n Junction Diodes—Part I: DC Properties," *IEEE Transaction of Electron Devices*, vol. 46, no. 3, pp. 478-484, 1999.
- [65] Q. Wahab, A. Ellison, A. Henry, E. Janzen, C. Hallin, J. D. Persio and R. Martinez, "Influence of epitaxial growth and substrate-induced defects on the breakdown of 4H-SiC Schottky diodes," *Applied Physics Letters*, vol. 76, no. 19, pp. 2725-2727, 2000.
- [66] H. Lendenmann, F. Dahlquist, N. Johansson, R. Soderholm, P. A. Nilsson, J. P. Bergman and P. Skytt, "Long term operation of 4.5kV PiN and 2.5kV JBS diodes," *Material Science Forum*, Vols. 353-356, pp. 727-730, 2001.
- [67] S. Ha, M. Skowronski, W. M. Vetter and M. Dudley, "Basal plane slip and formation of mixed-tilt boundaries in sublimation grown hexagonal polytype silicon carbide single crystals," *Journal of Applied Physics*, vol. 92, no. 2, pp. 778-785, 2002.
- [68] J. Fan and P. K. Chu, *Silicon Carbide Nanostructures: Fabrication, Structure, and Properties*, Springer, 2014.
- [69] S. Ha, N. T. Nufher, G. S. Rohrer, M. D. Graef and M. Skowronski, "Identification of Prismatic Slip Bands in 4H SiC Boules Grown by Physical Vapor Transport," *Journal of Electronic Materials*, vol. 29, no. 7, pp. L5-L8, 2000.
- [70] S. Ha, W. M. Vetter, M. Dudley and M. Skowronski, "A simple mapping method for elementary dislocations in heteroepitaxial SiC layers," *Material Science Forum*, vol. 389-393, pp. 443-446, 2002.
- [71] S. Amelinckx and G. Strumane, "Dislocations in Silicon Carbide," *Journal of Applied Physics*, vol. 31, no. 8, pp. 1359-1370, 1960.
- [72] E. K. Sanchez, J. Q. Liu, M. D. Graef, M. Skowronski, W. M. Vetter and M. Dudley, "Nucleation of threading dislocations in sublimation grown silicon carbide," *Journal of Applied Physics*, vol. 91, no. 3, pp. 1143-1148, 2002.
- [73] J. Takahashi, M. Kanaya and Y. Fujiwara, "Sublimation growth of SiC single crystalline ingots on faces perpendicular to the (0001) basal plane," *Journal of Crystal Growth*, vol. 135, no. 1-2, pp. 61-70, 1994.
- [74] D. Siche, D. Klimm, T. Hölzel and A. Wohlfart, "Reproducible defect etching of SiC single crystals," *Journal of Crystal Growth*, vol. 270, no. 1-2, pp. 1-6, 2004.
- [75] M. A. Mannan, S. K. Chowdhuri, K. V. Nguyen and K. C. Mandal, "Effect of $Z_{1/2}$, EH_5 and $Ci1$ deep defects on the performance of n-type 4H-SiC epitaxial layers Schottky detectors : Alpha spectroscopy and deep level transient spectroscopy studies," *Journal of Applied Physics*, vol. 115, no. 22, pp. 224504 (1-6), 2014.
- [76] M. E. Levinshtein, S. L. Rumyantsev and M. S. Shur, *Properties of Advanced*

- Semiconductor Materials: GaN, AlN, InN, BN, SiC, SiGe, London: John Wiley & Sons, 2001.
- [77] M. Jang, Y. Kim, J. Shin and S. Lee, "Characterization of erbium-silicided Schottky diode junction," *IEEE Electron Devices Letter*, vol. 26, no. 6, p. 354 – 356, 2005.
- [78] G. F. Knoll, Radiation Detection and Measurement, New York: John Wiley & Sons, 2000.
- [79] M. B. H. Breese, "A theory of ion beam induced charge collection," *Journal of Applied Physics*, vol. 74, no. 6, pp. 3789-3799, 1993.
- [80] J. F. Ziegler, J. Biersack and U. Littmark, The Stopping and Range of Ions in Matter, New York: Pergamon Press, 1985.
- [81] S. N. Ahmed, Physics & Engineering of Radiation Detection, San Diego: Elsevier, 2007.
- [82] A. Owens and A. Peacock, "Compound semiconductor radiation detectors," *Nuclear Instruments and Methods in Physics Research*, vol. 531, no. 1-2, pp. 18-37, 2004.
- [83] S. K. Chaudhuri, K. J. Zavalla and K. C. Mandal, "Experimental determination of electron-hole pair creation energy in 4H-SiC epitaxial layer: An absolute calibration approach," *Applied Physics Letters*, vol. 102, no. 3, pp. 031109 (1-4), 2013.
- [84] Z.-Q. Fang, B. Claflin, D. C. Look, L. Polenta and W. C. Mitchel, "Thermally stimulated current spectroscopy of high-purity semiinsulating 4H-SiC substrates," *Journal of Electronic Materials*, vol. 34, pp. 336-340, 2005.
- [85] D.C. Look, "The Electrical and Photoelectronic Properties of Semi-Insulating GaAs," *Semiconductors and Semimetals*, vol. 19, pp. 75-170, 1983.
- [86] K. C. Mandal, P. G. Muzykov, R. Krishna, T. Hayes and T. S. Sudarshan, "Thermally stimulated current and high temperature resistivity measurements of 4H semi-insulating silicon carbide," *Solid State Communications*, vol. 151, no. 7, pp. 532-535, 2011.
- [87] K. C. Mandal, R. Krishna, P. G. Muzykov, T. Hayes and T. S. Sudarshan, "Characterization of Semi-Insulating 4H Silicon Carbide for Radiation Detectors," *IEEE Transactions on Nuclear Science*, vol. 58, pp. 1992-1999, 2011.
- [88] M. Pavlovic and U. V. Desnica, "Precise determination of deep trap signatures and their relative and absolute concentrations in semi-insulating GaAs," *Journal of Applied Physics*, vol. 84, no. 4, pp. 2018-2024, 1998.
- [89] A. A. Lebedev, "Deep level centers in Silicon Carbide," *Semiconductors*, vol. 19, pp. 107-130, 1999.
- [90] W. C. Mitchel, R. Perrin, J. Goldstein, A. Saxler, M. Roth, S. R. Smith, J. S. Solomon and A. O. Evwaraye, "Fermi level control and deep levels in semi-insulating 4H-SiC," *Journal of Applied Physics*, vol. 86, no. 9, pp. 5040-5044, 1999.
- [91] J. R. Jenny, S. G. Müller, A. Powell, V. F. Tsvetkov, H. M. Hobgood, R. C. Glass and C. H. Carter, "High-purity semi-insulating 4H-SiC grown by the seeded-

- sublimation method," *Journal of Electronic Materials*, vol. 31, no. 5, pp. 366-369, 2002.
- [92] K. C. Mandal, R. Krishna, P. G. Muzykov, S. K. Chowdhuri and J. R. Terry, "Assessment of 4H-SiC epitaxial layers and high resistivity bulk crystals for radiation detectors," in *SPIE Conference*, San Diego, 2012.
- [93] P. G. Muzykov, R. M. Krishna and K. C. Mandal, "Characterization of deep levels in n-type and semi-insulating 4H-SiC epitaxial layers by thermally stimulated current spectroscopy," *Journal of Applied Physics*, vol. 111, no. 1, pp. 014910 (1-7), 2012.
- [94] L. Storasta, F. H. C. Carlsson, S. G. Sridhara, J. P. Bergman, A. Henry, T. Egilsson, A. Hallén and E. Janzén, "Pseudodonor nature of the DI defect in 4H-SiC," *Applied Physics Letters*, vol. 78, no. 1, pp. 46-48, 2001.
- [95] C. Hemmingsson, N. T. Son, O. Kordina, J. P. Bergman, E. Janzén, J. L. Lindström, S. Savage and N. Nordell, "Deep level defects in electron-irradiated 4H SiC epitaxial layers," *Journal of Applied Physics*, vol. 81, no. 9, pp. 6155-6159, 1997.
- [96] K. Danno and T. Kimoto, "Deep level transient spectroscopy on as-grown and electron-irradiated p-type 4H-SiC epilayers," *Journal of Applied Physics*, vol. 101, no. 10, pp. 103704(1-5), 2007.
- [97] I. Pintilie, L. Pintilie, K. Irmsche and B. Thomas, "Deep levels in as-grown 4H-SiC epitaxial layers and their correlation with CVD parameters," *Material Science Forum*, Vols. 433-436, pp. 463-466, 2003.
- [98] N. T. Son, B. Magnusson, Z. Zolnai, A. Ellison and E. Janzén, "Defects in High-Purity Semi-Insulating SiC," *Material Science Forum*, Vols. 457-460, pp. 437-442, 2004.
- [99] T. Dalibor and G. Pensl, "Electrical properties of the titanium acceptor in silicon carbide," *Physical Review B*, vol. 55, no. 20, pp. 13618-13624, 1997.
- [100] T. Dalibor, G. Pensl, H. Matsunami, T. Kimoto, W. J. Choyke, A. Schöner and N. Nordell, "Deep defect centers in silicon carbide monitored with deep level transient spectroscopy," *Physica Status Solidi (a)*, vol. 162, no. 1, pp. 199-225, 1997.
- [101] Ł. Gelczuk, M. D. browska-Szata, M. Sochacki and J. Szmids, "Characterization of deep electron traps in 4H-SiC Junction Barrier Schottky rectifiers," *Solid-State Electronics*, vol. 94, pp. 56-60, 2014.
- [102] J. Zhang, L. Storasta, J. P. Bergman, N. T. Son and E. Janzén, "Electrically active defects in n-type 4H-silicon carbide grown in a vertical hot-wall reactor," *Journal of Applied Physics*, vol. 93, no. 8, pp. 4708-4714, 2003.
- [103] A. Castaldini, A. Cavallini, L. Polenta, F. Nava, C. Canali and C. Lanzieri, "Defective states analysis in Silicon Carbide," *Applied Surface Science*, vol. 187, no. 3, pp. 248-252, 2002.
- [104] L. Storasta, J. P. Bergman, E. Janzen, A. Henry and J. Lu, "Deep levels created by low energy electron irradiation in 4H-SiC," *Journal Applied Physics*, vol. 96, no. 9, pp. 4909-4915, 2004.
- [105] K. Danno and T. Kimoto, "Investigation of deep levels in n-type 4H-SiC epilayers

- irradiated with low-energy electrons," *Journal of Applied Physics*, vol. 100, no. 11, pp. 113728(1-6), 2006.
- [106] T. Hornos, A. Gali and B. G. Svensson, "Large-Scale Electronic Structure Calculations of Vacancies in 4H-SiC Using the Heyd-Scuseria-Ernzerhof Screened Hybrid Density Functional," *Material Science Forum*, Vols. 679 - 680, pp. 261-264, 2011.
- [107] N. Iwamoto, B. C. Johnson, N. Hoshino, M. Ito, H. Tsuchida, K. Kojima and T. Ohshima, "Defect-induced performance degradation of 4H-SiC Schottky barrier diode particle detectors," *Journal of Applied Physics*, vol. 113, no. 14, pp. 143714(1-5), 2013.
- [108] F. Nava, A. Castaldini, A. Cavallini, P. Errani and V. Cindro, "Radiation Detection Properties of 4H-SiC Schottky Diodes Irradiated Up to 1016 n/cm² by 1 MeV Neutrons," *IEEE Transaction of Nuclear Science*, vol. 53, no. 5, pp. 2977-2982, 2006.
- [109] A. Kawasuso, F. Redmann, R. Krause-Rehberg, P. Sperr, T. Frank, M. Weidner, G. Pensl and H. Itoh, "Annealing process of defects in epitaxial SiC induced by He and electron irradiation: Positron annihilation study," *Material Science Forum*, Vols. 353-356, pp. 537-540, 2001.
- [110] T. A. G. Eberlein, C. J. Fall, R. Jones, P. R. Briddon and S. Öberg, "Alphabet luminescence lines in 4H-SiC," *Physical Review B*, vol. 65, pp. 184108(1-4), 2002.
- [111] T. Tawara, H. Tsuchida, S. Izumi, I. Kamata and K. Izumi, "Evaluation of Free Carrier Lifetime and Deep Levels of the Thick 4H-SiC Epilayers," *Materials Science Forum*, Vols. 457-460, pp. 565-568, 2004.
- [112] P. B. Klein, B. V. Shanabrook, S. W. Huh, A. Y. Polyakov, M. Skowronski, J. Sumakeri and M. J. O'Loughlin, "Lifetime-limiting defects in n- 4H-SiC epilayers," *Applied Physics Letters*, vol. 88, no. 5, pp. 052110(1-3), 2006.
- [113] T. Kimoto, K. Danno and J. Suda, "Lifetime-killing defects in 4H-SiC epilayers and lifetime control by low-energy electron irradiation," *Physica Status Solidi (b)*, vol. 245, no. 7, pp. 1327-1336, 2008.
- [114] G. Alfieri and T. Kimoto, "Capacitance spectroscopy study of deep levels in Cl-implanted 4H-SiC," *Journal of Applied Physics*, vol. 112, no. 6, pp. 063717(1-4), 2012.
- [115] F. C. Beyer, C. G. Hemmingsson, H. Pedersen, A. Henry, J. Isoya, N. Morishita, T. Ohshima and E. Janzén, "Capacitance transient study of a bistable deep level in e-irradiated n-type 4H-SiC," *Journal of Physics D: Applied Physics*, vol. 45, pp. 455301(1-7), 2012.
- [116] K. Danno, T. Kimoto and H. Matsunami, "Midgap levels in both n - and p -type 4H-SiC epilayers investigated by deep level transient spectroscopy," *Applied Physics Letters*, vol. 86, no. 12, pp. 122104(1-3), 2005.
- [117] J. H. Werner and H. H. Guttler, "Barrier inhomogeneities at Schottky contacts," *Journal of Applied Physics*, vol. 69, no. 3, pp. 1522-1533, 1991.
- [118] R. T. Tung, "Electron transport of inhomogeneous Schottky barriers," *Applied Physics Letters*, vol. 58, no. 24, pp. 2821-2823, 1991.

- [119] J. P. Sullivan, R. T. Tung, M. R. Pinto and W. R. Graham, "Electron transport of inhomogeneous Schottky barriers: A numerical study," *Journal of Applied Physics*, vol. 70, no. 12, pp. 7403-7424, 1991.
- [120] M. A. Mannan, K. V. Nguyen and K. C. Mandal, "Isochronal Annealing on n-type 4H-SiC Epitaxial Schottky Barriers and Investigation of Defect Levels by Deep Level Transient Spectroscopy," in *IEEE Nuclear Science Symposium (NSS), Medical Imaging Conference (MIC), and 21st Symposium on Room-Temperature Semiconductor X-ray and Gamma-Ray Detectors (RTSD) Conference Record*, Seattle, WA, 2014.
- [121] T. A. G. Eberlein, R. Jones and P. R. Briddon, " Z_1/Z_2 Defects in 4H-SiC," *Physical Review Letter*, vol. 90, no. 22, pp. 225502(1-4), 2003.
- [122] T. Kimoto, K. Hashimoto and H. Matsunami, "Effects of C/Si Ratio in Chemical Vapor Deposition of 4H-SiC(112 $\bar{0}$) and (033 $\bar{8}$)," *Japanese Journal of Applied Physics*, vol. 42, no. 12, pp. 7294-7295, 2003.
- [123] G. Alfieri, E. V. Monakhov and B. G. Svensson, "Annealing behavior between room temperature and 2000 °C of deep level defects in electron-irradiated n-type 4H silicon carbide," *Journal of Applied Physics*, vol. 98, no. 5, pp. 043518 (1-5), 2005.
- [124] Y. Negoro, T. Kimoto and H. Matsunami, "Stability of deep centers in 4H-SiC epitaxial layers during thermal annealing," *Applied Physics Letters*, vol. 85, no. 10, pp. 1716-1718, 2004.